

Interactive Real Time Deep Brain Stimulation System

by

John Saad

A thesis

presented to the University of Waterloo

in fulfillment of the

thesis requirement for the degree of

Doctor of Philosophy

in

Electrical and Computer Engineering

Waterloo, Ontario, Canada, 2012

©John Saad 2012

Author's Declaration

I hereby declare that I am the sole author of this thesis. This is a true copy of the thesis, including any required final revisions, as accepted by my examiners.

I understand that my thesis may be made electronically available to the public.

Abstract

Deep Brain Stimulation (DBS) is a developing therapeutic technique with a high potential to control and treat central nervous system diseases through neuromodulation. DBS utilizes through implanted electrodes that are inserted in the targeted brain structure. Being an emerging technology; neuromodulation introduces many challenges that are not yet comprehensively identified, characterized and resolved. The advancement of this technique requires qualitative and quantitative perception of the brain response to electrical stimulation which is controlled by the electric field distribution within the brain tissue. This can be realized by formulating the tissue-field interaction such that we will have a better understanding of the spatial extent and the direct effects of deep brain stimulation (DBS) on neurons activity. The focus of this research is to develop a model for encoding and decoding the neuron activity in the DBS region and to address all the parameters that affect this activity in order to have a complete understanding of the DBS problem and to develop a brain model that can be readily used in DBS analysis. Our goal is to study the immediate direct effects of the stimulating field and examine where the beneficial effects of DBS originate since the mechanism of DBS is not yet fully understand and hence an inclusive comprehensive performance study will be done for the DBS problem.

Acknowledgements

“For I am the LORD, your God, who takes hold of your right hand and says to you, Do not fear, I will help you” (Isaiah 41:13)

Thank you my LORD for taking care of me, protecting me, and putting me on the right track.

I would like to express my gratitude and appreciation to my supervisors Prof. Magdy Salama and Prof. Raafat Mansour for their support, guidance, patience and providing a productive atmosphere for doing research.

I would also like to thank my committee members Professor Magdy Attia, Professor Daniel Stashuk, Professor Fakhreddine Karray and Professor Zhou Wang. I appreciate their time and effort devoted for reading my Ph.D. thesis and providing me with their insightful comments and invaluable suggestions, thereby further improving the quality of my research work.

Special thanks to my lovely wife Sally and my beautiful kids Maurine and Mena.

Finally, I would love to thank my family and friends who shared with me the ups and downs of this long journey.

Dedication

This thesis is dedicated to my father, mother and brother for their endless support, inspiration, and encouragement.

Table of Contents

Author's Declaration.....	ii
Abstract	iii
Acknowledgements	iv
Dedication	v
Table of Contents	vi
List of Figures.....	x
List of Tables.....	xvi
Chapter 1 Introduction	1
1.1 Introduction to Deep Brain Stimulation (DBS)	1
1.2 Motivation.....	2
1.3 Research Objective.....	3
1.4 Thesis Outline	4
Chapter 2 Literature Survey.....	5
2.1 History of Deep Brain Stimulation.....	5
2.2 How Does DBS Work?	6
2.3 Conditions Treatable by DBS.....	7
2.3.1 Parkinson's Disease.....	8
2.3.2 Dystonia	8
2.3.3 Essential Tremor	8
2.4 DBS Advantages and Disadvantages	8
2.5 DBS Electrode Configuration	9
2.6 DBS Active Contact Configuration and Safety.....	10
2.7 Introduction to Neuronal System.....	13
2.7.1 Elements of Neuronal Systems.....	13
2.7.2 The Ideal Neuron	14
2.8 Threshold and Action Potential.....	16
2.8.1 Equilibrium Potential	17
2.8.2 Nernst Potential.....	18
2.8.3 Reversal Potential	19
2.9 Neuron Models Responses	20
2.10 Detailed Neuron Models.....	21

2.10.1 Leaky Integrate-and-Fire Model (LIF)	21
2.10.2 Hodgkin-Huxley Model	24
2.11 Ion Channels	27
2.11.1 Sodium Channels	27
2.11.2 Potassium Channels	27
2.11.3 Low-Threshold and High-Threshold Calcium Current.....	28
2.12 Which model should we choose?	28
2.13 Spatial Structure: the Dendritic Tree	28
2.13.1 Cable Theory	29
2.14 Compartmental Models	30
2.15 Axon Models	31
2.16 Complete STN Neuron Model	34
2.17 Rate versus Time Codes	37
2.18 Summary of the Survey	38
Chapter 3 Proposed Interactive Real Time Comprehensive DBS System	39
3.1 Introduction	39
3.2 The Main Components of the DBS Model.....	41
3.3 Methodology	45
3.3.1 Electrode Modeling.....	45
3.3.2 Brain Modeling.....	45
3.3.3 Electric Field Solver	45
3.3.4 Stimulation Waveform.....	46
3.3.5 Neural Modeling	46
3.3.6 Neuron Decoding	47
3.3.7 Linear Filter Technique	47
3.3.8 Singular Value Decomposition (SVD)	49
3.4 Challenges	51
3.5 Conclusion	51
Chapter 4 The Effect of Medium Brain Tissue and Stimulation Pulse Parameters on the Electric Field Distribution in a Deep Brain Stimulation System	52
4.1 Introduction	52
4.2 Brain Tissue Properties.....	54

4.2.1 Brain Conductivity.....	54
4.2.2 Brain Permittivity.....	54
4.2.3 Biological Tissue Parameters Database.....	55
4.2.4 Discussion.....	58
4.3 Finite Difference Time Domain (FDTD).....	58
4.4 Brain Modeling.....	59
4.4.1 Modeling a DBS Electrode Inside Homogeneous Brain Tissue (Model-I).....	59
4.4.2 Foreign Body Response and Encapsulation Formation (Model-II).....	61
4.4.3 DBS Electrode Position with Respect to Two Different Brain Tissues (Model-III).....	62
4.5 Simulation Setup.....	63
4.5.1 Discretization and Model Stability.....	64
4.6 Simulation Results.....	66
4.7 Stimulation Pulse.....	73
4.8 Firing Pattern Stimulation.....	76
4.9 Electrode Array.....	78
4.10 Conclusion.....	79
Chapter 5 Evaluating the Activating Function in Deep Brain Stimulation System.....	81
5.1 Introduction.....	81
5.2 Electromagnetic Solution.....	82
5.3 Finite Element Model.....	83
5.4 Stimulation Results.....	84
5.4.1 Activating Function Calculation along Lateral Axis of the Electrode.....	89
5.4.2 Activating Function along Tilted Axis with Respect to DBS Electrode Shaft.....	96
5.5 Effect of Pulse Width.....	102
5.6 Effect of DBS Electrode Encapsulation Thickness.....	104
5.6.1 Electric Field Distribution Calculation.....	105
5.6.2 Effect of Encapsulation Thickness on Voltage and Activating Function.....	106
5.6.3 Current Density and Impedance Calculation.....	107
5.7 DBS Electrode in Anisotropic Conductivity Medium.....	109
5.8 DBS Electrode Representation versus Point Source Approximation.....	111
5.9 Conclusion.....	113
Chapter 6 Deep Brain Stimulation Neuron Simulations and Modeling.....	115

6.1 Introduction	115
6.2 STN Neuron Cell Model	116
6.3 DBS STN Tuning Curves	120
6.4 Neurons Firing Decoding	121
6.5 Volume of Tissue Activated (VTA) of Neurons	127
6.6 Stochastic STN Neuron Model	131
6.7 Conclusion	136
Chapter 7 Conclusions and Future Work	138
7.1 Conclusions	138
7.2 Future Work	140
References	141

List of Figures

Figure 2-1 DBS electrode implantation [4]	6
Figure 2-2 DBS activity in STN of Parkinson's disease [18]	7
Figure 2-3 A few of many possible electrode configurations.....	9
Figure 2-4 Schematic representation of stimulus pulse [17]	11
Figure 2-5 Analogy describes how multiple active contacts can lower the impedance [17].....	12
Figure 2-6 A schematic representation of the deposition and removal of electrical charge by the first and second phases [17].....	12
Figure 2-7 Neurons in the mammalian cortex representing cells, dendrites, and axons [20].....	13
Figure 2-8 Neuron classification in the brain [21]	14
Figure 2-9 A schematic representation of a motor neuron structure neuron indicating its detailed structure and how neurons are connected through Synapses [21].....	15
Figure 2-10 Chemical synapse structure [22].....	16
Figure 2-11 Action potential pulse levels and phases	17
Figure 2-12 The cell membrane structure of the neuron cell [24].....	18
Figure 2-13 Action potential phases indicating depolarization, repolarization and hyperpolarization of the neuron cell [21]	19
Figure 2-14 LIF neuron model [24].....	22
Figure 2-15 LIF spike response [24]	23
Figure 2-16 Firing rate of LIF model for a constant input current	23
Figure 2-17 Schematic diagram for the Hodgkin-Huxley model	24
Figure 2-18 The asymptotic value $x_0(V)$ and the time constant $\tau x(V)$ for the three variables m, n, h in the Hodgkin-Huxley model.	26
Figure 2-19 Comparison of the neuro-computational properties of spiking models [26]	28
Figure 2-20 A schematic drawing of cable theory	29
Figure 2-21 Multi-compartment neuron model [34]	31
Figure 2-22 The axon segment model [37]	32
Figure 2-23 Cable model of a STN neuron [38].....	35
Figure 2-24 Mean firing rate vs. a temporal average.....	37
Figure 3-1 A schematic diagram of the proposed DBS model with its input and output parameters	39
Figure 3-2 A complete detailed diagram of the proposed DBS model.....	40
Figure 3-3 A detailed flow chart of some of the components in the proposed DBS model	44
Figure 3-4 The reduced SVD or rank approximation	50

Figure 4-1 Semi-log plot of the relative permittivity of White and Grey matter 10 Hz – 1 KHz ...	56
Figure 4-2 Semi-log plot of the relative permittivity of White and Grey matter 1 KHz – 100KHz	56
Figure 4-3 Conductivity of White and Grey matter 10 Hz – KHz	57
Figure 4-4 Loss Tangent of White and Grey matter 10 Hz – 100 MHz	57
Figure 4-5 Schematic diagram of the proposed Model-I.....	60
Figure 4-6 FDTD Medtronic 3387 DBS electrode.....	60
Figure 4-7 A schematic diagram of the proposed Model-II representing the electrode surrounded with an encapsulation layer inside the Grey tissue.....	63
Figure 4-8 A schematic diagram of the proposed Model-III representing the electrode surrounded with Grey tissue and inserted in White matter.....	63
Figure 4-9 Time domain normalized Gaussian stimulation pulse.....	64
Figure 4-10 Excitation voltage values applied to a Medtronic 3387 electrode.....	64
Figure 4-11 Effect of oversampling on the input simulation pulse.....	65
Figure 4-12 Electric field distribution for Gaussian pulse, $\epsilon_r = 1 \times 10^5$, $\sigma = 0.1 \text{ S.m}^{-1}$	66
Figure 4-13 Maximum electric field values for different permittivities estimated for several conductivities.....	67
Figure 4-14 Electric field intensity vs. permittivity @ $\sigma = 0.1 \text{ S.m}^{-1}$	69
Figure 4-15 Model-II: Homogenous model with encapsulation layer; $\epsilon_r = 1 \times 10^5$, gray box (Grey tissue): $\sigma_{\text{Gray tissue}} = 0.1 \text{ S.m}^{-1}$, red box (encapsulation layer): $\sigma_{\text{capsule}} = 0.05 \text{ S.m}^{-1}$	70
Figure 4-16 Maximum electric field intensity vs. capsule thickness (TCapsule) for tissue permittivity of ; $\epsilon_r = 1 \times 10^5$ and $\sigma_{\text{Gray tissue}} = 0.1 \text{ S.m}^{-1}$, $\sigma_{\text{Capsule}} = 0.05 \text{ S.m}^{-1}$.	71
Figure 4-17 Model-III: Non-homogeneous model for Grey and White tissue layers, red box (Grey tissue): $\epsilon_r - \text{Gray tissue} = 1 \times 10^5$, $\sigma_{\text{Gray tissue}} = 0.1 \text{ S.m}^{-1}$, gray box (White tissue): $\epsilon_r - \text{White tissue} = 4 \times 10^4$, $\sigma_{\text{White tissue}} = 0.06 \text{ S.m}^{-1}$	72
Figure 4-18 Maximum electric field intensity vs. Grey matter thickness (TGray) for $\epsilon_r - \text{Gray tissue} = 1 \times 10^5$, $\sigma_{\text{Gray tissue}} = 0.1 \text{ S.m}^{-1}$ and $\epsilon_r - \text{White tissue} = 4 \times 10^4$, $\sigma_{\text{White tissue}} = 0.06 \text{ S.m}^{-1}$	72
Figure 4-19 Effect of pulse amplitude on field distribution, (left: 1 V , right: 10 V) @ $\epsilon_r = 10^5$, $\sigma = 0.1 \text{ S.m}^{-1}$	73
Figure 4-20 Electric field intensity vs. simulation pulse amplitude (A) for $\epsilon_r = 10^4$ and 10^5 @ $\sigma = 0.1 \text{ S.m}^{-1}$	74
Figure 4-21 Effect of pulse width on field distribution (52 and 52000 steps) @ $\epsilon_r = 10^5$, $\sigma = 0.1 \text{ S.m}^{-1}$	75

Figure 4-22 Electric field intensity vs. simulation pulse width @ $\sigma = 0.1 \text{ S.m} - 1, \epsilon_r = 10^5$	75
Figure 4-23 Current steering and field shaping, top: 2 rings firing, bottom: 3 rings firing	77
Figure 4-24 Maximum electric field vs. current steering ratio for different permittivity $\epsilon_r = 10^4$ and $\epsilon_r = 10^5$ at $\sigma = 0.1 \text{ S.m} - 1$	77
Figure 4-25 Two DBS electrode array, left: 100% current level on all rings, right: 0-100-0% (left shaft), 100-0-100% (right shaft).....	78
Figure 5-1 A schematic diagram for the input and output of the second order spatial voltage component	81
Figure 5-2 A 60 μs monophasic pulse and its FFT magnitude.....	82
Figure 5-3 Finite element meshing for the DBS electrode in Model-I.....	83
Figure 5-4 Finite element potential contour of DBS electrode for $V = -0.5$ Volt	84
Figure 5-5 Finite element potential contour of DBS electrode for $V = -1.0$ Volt	85
Figure 5-6 Finite element potential contour of DBS electrode for $V = -2.0$ Volt	85
Figure 5-7 Finite element potential contour of DBS electrode for $V = -3.0$ Volt	86
Figure 5-8 Electric potential along a vertical line passing 1 mm on the right of the active contact No. 1 for $V = -1$ volt.....	87
Figure 5-9 Electric potential along a vertical line passing 1 mm on the right of the active contact No. 1 for $V = -3$ volt.....	87
Figure 5-10 Finite element potential contour of DBS electrode for 4 active contacts (-3, -2, -1 and -0.5 volts.).....	88
Figure 5-11 Electric potential along a horizontal axis passing through the first active contact.	88
Figure 5-12 A schematic diagram of DBS electrode with respect to surrounding neurons where the activating function will be calculated at positions lateral to the electrode shaft	89
Figure 5-13 Electric potential and activating function along a vertical line passing 1 mm from DBS active contact No. 1 for $V = -1$ volt.....	90
Figure 5-14 Electric potential and activating function along a vertical line passing 2 mm from DBS active contact No. 1 for $V = -1$ volt.....	91
Figure 5-15 Electric potential and activating function along a vertical line passing 3 mm from DBS active contact No. 1 for $V = -1$ volt.....	91
Figure 5-16 Maximum activating function (AF_{\max})[V/m^2] for different positions from the electrode shaft for $V = -1$ volt applied to the DBS electrode first contact.	92
Figure 5-17 Electric potential and activating function along a vertical line passing 1 mm from DBS active contact No. 1 for $V = -3$ volt.....	93

Figure 5-18 Electric potential and activating function along a vertical line passing 2 mm from DBS active contact No. 1 for V= -3 volt.....	94
Figure 5-19 Electric potential and activating function along a vertical line passing 3 mm from DBS active contact No. 1 for V= -3 volt.....	94
Figure 5-20 Electric potential and activating function along a vertical line passing 4 mm from DBS active contact No. 1 for V= -3 volt.....	95
Figure 5-21 Maximum activating function (AF_{max})[V/m ²] for different positions from the electrode shaft for V= -3 volt compared to the case when V= -1 volt applied to the DBS electrode contact..	96
Figure 5-22 A schematic diagram of DBS electrode with respect to surrounded neurons where the activating function will be calculated along tilted axis with respect to electrode shaft.....	97
Figure 5-23 Electric potential and activating function along a 10 degree angle from the electrode axis.....	98
Figure 5-24 Electric potential and activating function along a 20 degree angle from the electrode axis.....	98
Figure 5-25 Electric potential and activating function along a 30 degree angle from the electrode axis.....	99
Figure 5-26 Electric potential and activating function along a 45 degree angle from the electrode axis.....	99
Figure 5-27 Electric potential and activating function along a 55 degree angle from the electrode axis.....	100
Figure 5-28 Electric potential and activating function along a 90 degree angle from the electrode axis.....	100
Figure 5-29 Maximum activating function (AF_{max})[V/m ²] for different angels from the electrode shaft	102
Figure 5-30 Activating function along a vertical line passing 1 mm from DBS active contact No. 1 for DBS pulse width = 90 μ s.....	103
Figure 5-31 Maximum activating function (AF_{max})[V/m ²] for different DBS pulse widths (μ s)....	104
Figure 5-32 Finite element potential contour of DBS electrode surrounded by 0.36 mm encapsulation thickness with conductivity $\sigma=0.05$ S.m ⁻¹	105
Figure 5-33 Finite element potential contour of DBS electrode surrounded by 1.0 mm encapsulation thickness with conductivity $\sigma=0.05$ S.m ⁻¹	105
Figure 5-34 Electric potential and activating function at 2 mm from DBS contact for V= -1 volt with 1.0 mm encapsulation thickness of conductivity $\sigma=0.05$ S.m ⁻¹	106

Figure 5-35 Surface current density distribution at DBS contact center with 0 mm encapsulation thickness of conductivity $\sigma=0.05 \text{ S.m}^{-1}$	107
Figure 5-36 Surface current density distribution at DBS contact center with 0.36 mm encapsulation thickness of conductivity $\sigma=0.05 \text{ S.m}^{-1}$	108
Figure 5-37 Surface current density distribution at DBS contact center with 1.0 mm encapsulation thickness of conductivity $\sigma=0.05 \text{ S.m}^{-1}$	108
Figure 5-38 DBS electrode contact impedance vs. encapsulation thickness from 0-1 mm.....	109
Figure 5-39 Finite element potential contour of DBS electrode surrounded by anisotropic medium of conductivity $\sigma_1 = 0.545 \text{ S.m}^{-1}$ and $\sigma_2 = 0.435 \text{ S.m}^{-1}$ respectively.....	110
Figure 5-40 Electric potential and activating function at 1 mm from DBS electrode surrounded by anisotropic medium of conductivity $\sigma_1 = 0.545 \text{ S.m}^{-1}$ and $\sigma_2 = 0.435 \text{ S.m}^{-1}$ respectively.....	110
Figure 5-41 DBS voltage distribution at 10 degree.....	112
Figure 5-42 DBS voltage distribution at 55 degree.....	112
Figure 5-43 DBS voltage distribution at 90 degree.....	112
Figure 5-44 Point source approximation	112
Figure 6-1 A schematic diagram of the inputs and outputs of the neuron environment indicating the coupling between the activating function calculated from FEM model and neuron environment tool to detect neuron firing activity	115
Figure 6-2 Position of the electrode with respect to the neuron for two different scenarios 1 and 2	117
Figure 6-3 Propagation of action potential along the axon.....	117
Figure 6-4 Action Potential cannot be triggered due to hyperpolarization effect	118
Figure 6-5 Firing activity rate (spikes/second) for DBS electrode stimulation amplitude voltage of -0.5 volt.....	119
Figure 6-6 Firing activity rate (spikes/second) for DBS electrode stimulation amplitude voltage of -2.0 volt.....	119
Figure 6-7 Position of the electrode with respect to two neurons (N=2).....	120
Figure 6-8 Tuning curves for two neurons (N=2) located at 1.0 mm and 1.5 mm from electrode shaft at the center of the first DBS electrode contact.....	120
Figure 6-9 A schematic diagram of the inputs and outputs of the optimal linear decoder filter	121
Figure 6-10 Tuning curves for neuron population (N=10) oriented perpendicular to the electrode shaft with 0.25mm inter distance.....	122

Figure 6-11 Tuning curves for neuron population (N=20) oriented perpendicular to the electrode shaft with 0.25mm inter distance.....	122
Figure 6-12 Tuning curves for neuron population (N=30) oriented perpendicular to the electrode shaft with 0.25mm inter distance.....	123
Figure 6-13 Tuning curves for neuron population (N=40) oriented perpendicular to the electrode shaft with 0.25mm inter distance.....	123
Figure 6-14 Tuning curves for neuron population (N=50) oriented perpendicular to the electrode shaft with 0.25mm inter distance.....	124
Figure 6-15 Optimal linear filter coefficients for N=10.....	125
Figure 6-16 Reconstructed DBS pulse amplitude versus applied input DBS pulse amplitude	125
Figure 6-17 Optimal linear filter coefficients for N=20.....	126
Figure 6-18 Optimal linear filter coefficients for N=30.....	126
Figure 6-19 Optimal linear filter coefficients for N=40.....	126
Figure 6-20 Optimal linear filter coefficients for N=50.....	126
Figure 6-21 Mean square error versus number of neurons (N) used to build tuning curves	127
Figure 6-22 Prediction of neuron model activation for pulse amplitude $V = -0.5$ Volt	128
Figure 6-23 Prediction of neuron model activation for pulse amplitude $V = -1$ Volt	129
Figure 6-24 Prediction of neuron model activation for pulse amplitude $V = -2$ Volt	129
Figure 6-25 Prediction of neuron model activation for pulse amplitude $V = -3$ Volt	130
Figure 6-26 Effect of DBS pulse amplitude on VTA for different four voltage values (-0.5 V, -1.0 V, -2.0 V, and -3.0 V).....	130
Figure 6-27 Firing activity rate (spikes/second) for DBS amplitude voltage of $v = -0.35$ volt with $\tau = 0$ ms	133
Figure 6-28 Firing activity rate (spikes/second) for DBS amplitude voltage of $v = -0.35$ volt with $\tau = 5$ ms	133
Figure 6-29 Firing activity rate (spikes/s) for DBS amplitude voltage of $v = -0.35$ volt with $\tau = 10$ ms	134
Figure 6-30 Neuron firing rates variation on a tuning curve for a neuron located at 1.5 mm from electrode shaft at the center of the first DBS electrode contact.....	134
Figure 6-31 Mean square error versus neuron populations N for $\sigma \cong 0.1$	135
Figure 6-32 Comparison of Mean square error versus neuron populations N for deterministic STN model and stochastic STN model of $\sigma \cong 0.1$	136

List of Tables

Table 2-1 Advantages and disadvantages of various DBS lead active contact configuration	10
Table 2-2 A review of 8 of the most biological spiking neurons responses [26]	20
Table 2-3 The parameters of the Hodgkin-Huxley equations [23]	25
Table 2-4 Values of α and β parameters of the Hodgkin-Huxley equations [23]	26
Table 2-5 Axon geometric parameters for different fiber diameters from 2-16 μm [36, 37].	33
Table 2-6 Axon model electrical parameters [36]	34
Table 2-7 STN model geometric parameters [38]	36
Table 2-8 STN cell body and dendrite electrical parameters [38]	36
Table 4-1 Mean values for brain tissue conductivity	55
Table 4-2 Tissue conductivities, σ , relative permittivity, ϵ_r , and loss tangent calculated at a median frequency of 130 Hz for the Grey and White tissue matter.	61
Table 4-3 Maximum electric field intensities [V/m] for different tissue dielectric properties	68
Table 4-4 Electric field penetration depth activated vs. tissue permittivity values	68
Table 5-1 Maximum and minimum activating function (AF) [V/m ²] for different positions from the electrode shaft	92
Table 5-2 Maximum and minimum activating function (AF) [V/m ²] for different positions from the electrode shaft	95
Table 5-3 Maximum and minimum activating function (AF) [V/m ²] for different degree angles from the electrode shaft	101
Table 5-4 Maximum activating function (AF) [V/m ²] for different DBS pulse widths at 1.0mm from the DBS electrode shaft	103
Table 6-1 Effect of DBS pulse amplitude on VTA and its equivalent radius	131
Table 6-2 Neurons spiking rate for different time constant τ at DBS pulse amplitude = - 0.35 V	132

Chapter 1

Introduction

1.1 Introduction to Deep Brain Stimulation (DBS)

Deep brain stimulation (DBS) is one of the fastest developing fields within the neurological specialties. Even though this technique emerged only 20 years ago and had its real breakthrough as a clinical therapy around the millennium, more than 50,000 patients have already been treated with this therapy [1].

DBS has provided dramatic clinical benefit for several central nervous system disorders including Parkinson's disease (PD), essential tremor (ET) and torsion dystonia [2], which regular surgical and chemical therapies fail to treat. Placement of electrical stimulating electrodes in the region of the ventral intermediate nucleus of the thalamus (VIM) without purposefully destroying the brain, can markedly reduce tremor in these conditions, and stimulation of either the subthalamic nucleus (STN) or the internal segment of the globus pallidus (GPi) may not only reduce tremor, but also decrease bradykinesia which plague people with PD [1, 2].

DBS works with electrical stimulation of the central, peripheral and autonomic nervous systems which is currently a standard clinical practice for treating and investigating several diseases [3]. This electrical stimulation is a form of functional electrical stimulation (FES) which is employed in developing electrotherapeutic techniques. The electrical stimulation is adjustable and can be changed as the person's disease changes or his or her response to medications change. No further surgery is necessary to make the adjustments.

In 1997, stimulation of the thalamus was approved by the FDA for the treatment of movement disorders and it was implemented in many patients using electrodes and stimulators supplied by Medtronic [4, 14]. In addition, a number of adverse effects can be generated by DBS including sensory motor impairments, involuntary movements (stimulation-induced dyskinesias), as well as speech, mood, and cognitive disturbances [5]. Often these side effects can be avoided or alleviated with proper adjustment of the stimulation settings [6].

Being an emerging technology; DBS introduces many challenges that are not yet comprehensively identified, characterized and resolved and is still being experimented and developed in order to be presented as a standard medical care [4]. It has the potential to provide substantial benefit for a variety of neuropsychiatric conditions. Despite the marked clinical benefit, we still have much to learn about the mechanism of action of DBS.

The convincing clinical efficacy achieved by the DBS has occurred without a clear understanding of the therapeutic mechanism of the action, although different hypotheses involving neuronal excitation and inhibition have been discussed [7]. One fundamental step towards a deeper comprehension and a proper use of DBS in evoking neural responses is to characterize the electric potential, the electric field, and the activating function generated inside the brain [8].

1.2 Motivation

There are many important issues to be addressed when considering deep brain stimulation. It is a reversible technique that is currently used for the treatment of PD and may be suitable for the treatment of psychiatric disorders. Whether DBS inactivates the target structure is still a matter of debate, this will give us the motivation to work in modeling these electrotherapeutic techniques.

Nevertheless, neither the mechanism of action for DBS nor the neurophysiology of the PD state is characterized [9]. As a result, it is not known a priori which DBS waveform will be most effective and the standard DBS parameters (e.g., the frequency, duration, and amplitude of a square-wave pulse train) typically must be hand-tuned by neurologists, this is always done after many trials.

The advancement of these electrotherapeutic techniques requires qualitative and quantitative perception of the brain neuron response to the electrical stimulation. This response is controlled by the electric field distribution within the brain tissue that can be realized by formulating models to this tissue-field interaction.

This field interaction generates an excitatory effect on the neurons and axons that are surrounded by the electrical field, the time dependent voltage distribution caused by this electrical field inside the brain tissue becomes as an input to those axons and neurons. Since it is very difficult to measure the effects of stimulation parameters of the neuron level, this will also be a motivation in the development of simulation models for implanted DBS electrodes in order to estimate the electric field distribution in the ambient brain tissue induced by deep brain stimulation patterns.

1.3 Research Objective

This research endeavor focuses on the modeling and decoding of neural activity inside the STN or globus pallidus pars interna (GPI) of the basal ganglia [10]. The fundamental goal of this research is to enhance our understanding of the target neural elements of the stimulation through models as well as providing an introduction to the investigational field of DBS.

In order to achieve our goals, we will propose a model that we named the DBS model. It will develop an understanding of the dependence of electric field distribution within brain tissue, and its associated volume of tissue activated (VTA) on the different parameters that configure the DBS technique. Our DBS model will study the immediate effects of the DBS stimulating field and will examine where the beneficial effects of DBS originate since the mechanism of DBS is not yet fully understood.

We will quantitatively evaluate the neural response to the deep brain stimulation parameters (Pulse amplitude, width and frequency), we will develop a brain neuron model that can be readily used in DBS analysis; also, we will study the effect of these stimulation parameters on neural firing activity. The different parameters will be mapped into mathematical functions to create a quantitative formulation for predicting the field distribution within brain tissue and estimating the volume of tissue activated (VTA).

The effect of the brain medium properties on our DBS model will be studied, This includes several tissue dielectric properties that take into consideration the homogeneous medium surrounding the DBS electrode; also we will address the isotropic and anisotropic neural tissue surrounding the DBS electrode which can in turn affect the neural polarization [11].

Neuron cell and axon modeling with a different population will also be taken into consideration to have a complete field interaction. Another important goal of this research is to develop an appropriate algorithm for encoding and decoding the neural activity in the DBS region and to address all the parameters that affect this activity.

The research major goals and objectives were successfully fulfilled and accomplished.

1.4 Thesis Outline

The first chapter of this thesis represents a brief introduction highlighting DBS and the role of neuromodulation as a medical procedure and outlines the objectives of the proposed research. Chapter two provides a survey of DBS history and definitions explaining its advantages and disadvantages as well as DBS electrode configurations and safety. The survey also outlines neuron models used and a comparison between them and explains the neuron activity terms used in modeling. In addition, it demonstrates current complete models of the STN. Chapter three provides the detailed proposed plan of our DBS system. Chapter four discusses the electromagnetic modeling and simulation of the implanted electrodes using finite difference time domain (FDTD). Finite element method (FEM) was considered in modeling the Medtronic DBS electrode to solve for the electric field and the voltage distribution to calculate the neuron activating function as been represented in chapter five. Chapter six discusses neuron simulations and modeling that validates our proposed DBS system. Finally, the thesis is concluded and future work is presented in chapter seven.

Chapter 2

Literature Survey

In this chapter, we will survey the state of the art in DBS mechanism and the various biological neuron models that represent the action potential. We will identify the compartment model details for the STN regions in which DBS electrodes are implanted.

2.1 History of Deep Brain Stimulation

In the early 1950s, doctors found that lesioning, or destroying, specific areas within the brain could help treat certain movement disorders [12]. When areas of the brain involved in the disorder were lesioned, the symptoms often improved. Unfortunately, lesioning surgery was not an ideal solution. They weren't always effective in reducing negative symptoms, and sometimes they resulted in damaging side effects. One of the main problems with lesioning surgeries is that lesioned brain structure is permanently destroyed. As a result, unwanted side effects are usually irreversible.

In the 1970s a new drug therapy for movement disorders was introduced to control some of the same types of symptoms as lesioning, but without risky brain surgery [4]. Drug therapy quickly began to replace lesioning surgeries, after many years, however, long-term drug therapy was found to cause new problems. The brain eventually compensates for the effects of the drugs. The result was often serious. Patients were developing new movement control problems that were considered worse than the original symptoms.

Then, in the late 1980s, a new discovery was made. Experts found that the same effects caused by lesioning brain tissue could be achieved by stimulating the tissue with harmless pulses of electricity [4, 9]. This was an exciting find, because the effects of electrical stimulation are completely reversible. In fact, when the stimulation is turned off, the brain resumes its normal behavior. Similar to drug treatments, doctors could tailor the electrical stimulation to fit the exact needs of each patient. Unlike drug treatments, the electrical stimulation could be localized so that only intended parts of the brain were affected.

Treatments with deep brain stimulation (DBS) were used on an experimental basis for several years [9, 13]. In 2002, the use of DBS for conditions such as Parkinson's disease was approved by the Food and Drug Administration (FDA). DBS remains the standard treatment for several brain disorders similar to, and including, Parkinson's.

2.2 How Does DBS Work?

Deep Brain Stimulation (DBS) involves implanting electrodes, thin wires, in some deep nuclei of the brain as shown in Figure 2-1. These electrodes are connected to a pace-maker placed under the skin. The pace-maker is set to send regular electrical pulses to the brain. This procedure aims at improving the patients' life by reducing the severity of their symptoms. This procedure is most frequently used to treat three conditions at present, Parkinson's disease, tremor and dystonia. After surgery patients need to be followed regularly. Today the treatment of Parkinson's disease using Deep Brain Stimulation is used world-wide. Current estimates are that more than 50,000 patients with movement disorders have been treated [13].

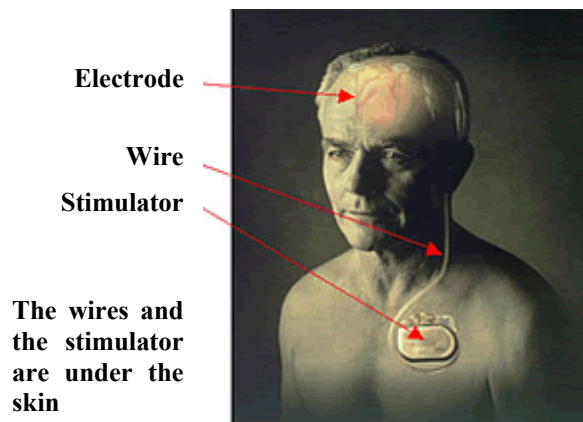


Figure 2-1 DBS electrode implantation [4]

DBS offers adjustable electrical stimulation patterns, whereas surgical destruction does not. The electrode has four metal contacts (Medtronic Electrode [14]) that can be used in many different combinations. Even if one electrode contact is not in the exact location, it is likely that one of the others or some combination of electrical contacts will be closer to the proper target. As the patient's response to surgery changes over time, the stimulation can be adjusted without the necessity of a repeat operation. The electrode that is implanted in the brain, and the electrical

systems that provide stimulation, are tolerated with no significant changes in brain tissue surrounding the electrodes

Although it is known that DBS suppresses activity in the overactive STN of Parkinson's patients and the Globus Pallidus Interna (GPi) in Dystonia patients as shown in Figure 2-2, more research is still needed to understand the action of DBS. The mechanism by which DBS produces clinical benefit remains uncertain and there is definitely need for more research [15].

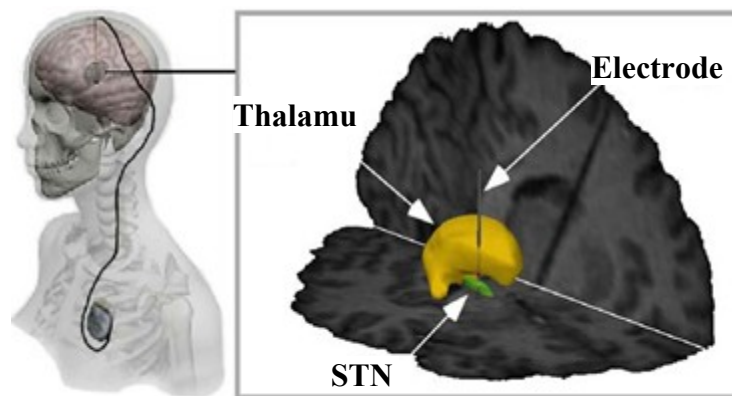


Figure 2-2 DBS activity in STN of Parkinson's disease [18]

Several types of neuronal behaviors that may be induced by STN stimulation are not clearly understood. Neurons can be affected directly by the stimulating field or can be indirectly affected by the trans-synaptically in the neuronal network. A key issue is to understand the mechanisms of DBS in order to determine which brain regions are directly affected by the electric stimulus and whether the target nucleus or other regions are affected or not. Indirect effects will then originate from these directly affected regions of the brain.

2.3 Conditions Treatable by DBS

- Parkinson's disease , Dystonia and Tremor

FDA approves thalamic DBS in 1997 for Parkinson's disease (PD) and Essential Tremor. In 2002 the use of DBS was expanded to treat other movement disorders (e.g., dystonia) [15].

2.3.1 Parkinson's Disease

Parkinson's is a progressive neurological condition affecting movements such as walking, talking, and writing. It is named after Dr James Parkinson (1755-1824) [16], the London doctor who first identified Parkinson's as a specific condition.

2.3.2 Dystonia

Dystonia is the term used to describe a condition dominated by involuntary sustained muscle spasms [4, 13, 15]. These spasms can affect various parts of the body and cause abnormal movements and postures, and can be extremely painful. The condition is thought to be caused by a malfunction of the central nervous system, probably in those parts of the brain called the basal ganglia. There is some evidence that there may be a malfunction in the way 'sensory' signals are interpreted in the brain, and how 'motor' signals are instigated.

2.3.3 Essential Tremor

Essential tremor is a common movement disorder that usually affects the head, chin, outstretched hands or voice. This disease causes tremor that is disabling in some. The cause of essential tremor is unknown, although it does run in some families [15].

2.4 DBS Advantages and Disadvantages

DBS has many advantages which can be summarized as follows:

- It doesn't destroy brain tissue and “won't” limit future treatment.
- The device can be removed at any time.
- It is adjustable.
- It is more effective than other operations in controlling tremors.

While its disadvantages are listed below

- Risks of chronically implanted device: infection, movement over time, erosion through skin
- Finite battery life of generator

- Device malfunction
- Time/staff investment for programming
- Cost

2.5 DBS Electrode Configuration

The usual process in DBS is to keep the electrode configuration the same while a series of voltages, frequencies and pulse widths are manipulated in order to control the spatial distribution of the electrical field. Neuronal elements further from the active DBS contact will experience a lower voltage than those elements closer to the active DBS contact. Thus, the spread of the electrical field can be controlled by scheming the stimulating voltage [17].

Fortunately, there are otherways to change the shape, size and strength of the electrical fields by changing the configuration of the active contacts. A monopolar configuration has a cathode (negative contact) on the DBS lead, and the impulse generator acts as the anode (positive contact) as shown in Figure 2-3, other configuration include bipolar and tripolar. The voltage in the monopolar falls off by the radius $V \propto 1/r$ where r is equal to the distance from the cathode. In bipolar the voltage drops by $V \propto 1/r^2$ while in the tripolar the voltage drops by $V \propto 1/r^3$

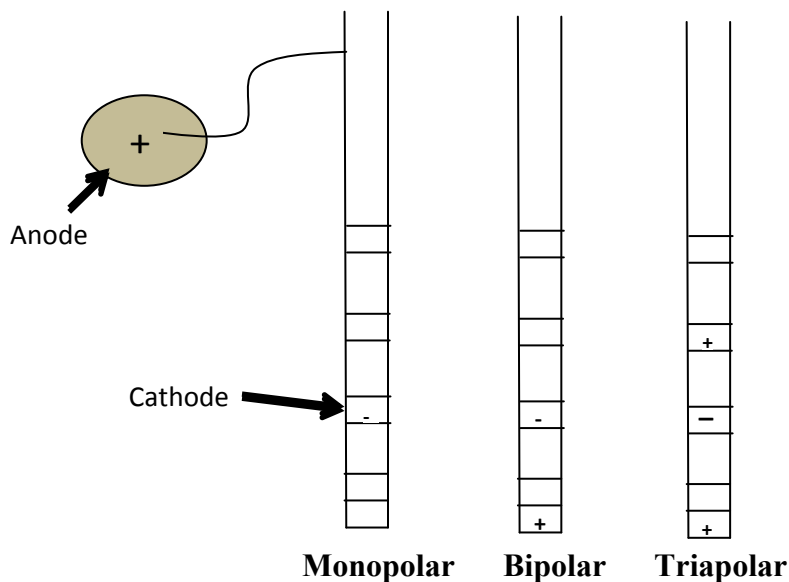


Figure 2-3 A few of many possible electrode configurations

In Table 2-1 the relative advantages and disadvantages of various DBS lead active contact configurations have been introduced.

Table 2-1 Advantages and disadvantages of various DBS lead active contact configuration

Configuration	Advantages	Disadvantages
Monopolar	<ul style="list-style-type: none"> • Produces the widest spread of the electrical field at the same relative voltages. • More effective if large volumes of brain need to be activated. 	<ul style="list-style-type: none"> • Wider spread increases risk of activation of unintended neuronal elements. • Tends to require higher stimulation voltages and consequently could increase the drain from the battery.
Bipolar	<ul style="list-style-type: none"> • Produce a more intense electrical field at the same relative voltages. • May be an advantage if DBS lead is near unintended neuronal elements. 	<ul style="list-style-type: none"> • Produce the least spread of the electrical field at the same relative voltages. • Least effective if large volume of brain or more neuronal elements within the target volume need to be activated.

2.6 DBS Active Contact Configuration and Safety

Since different active contact configurations can have an impact on the electrical voltage field, the different configuration can also have a marked impact on the amount of electrical energy dumped into the brain, which has safety consequences. There is a limit to how much electrical energy can be safely given, and that is $30\mu C/cm^2/phase$ [17]. This value refers to the amount of electrons (ions) passed into the brain with each stimulation pulse, where the per cm^2 refers to the surface area of the active contact and the per Phase refers to one component of the stimulation pulse as shown in Figure 2-4.

In Figure 2-4 the description of contact being cathode (negative) or anode (positive) is a misleading term. All contacts are cathode during the first phase and then anode during the second phase or vice versa. This is because the stimulation pulse is bi-phasic; it contains two phases where the polarity (negative and positive) reverses.

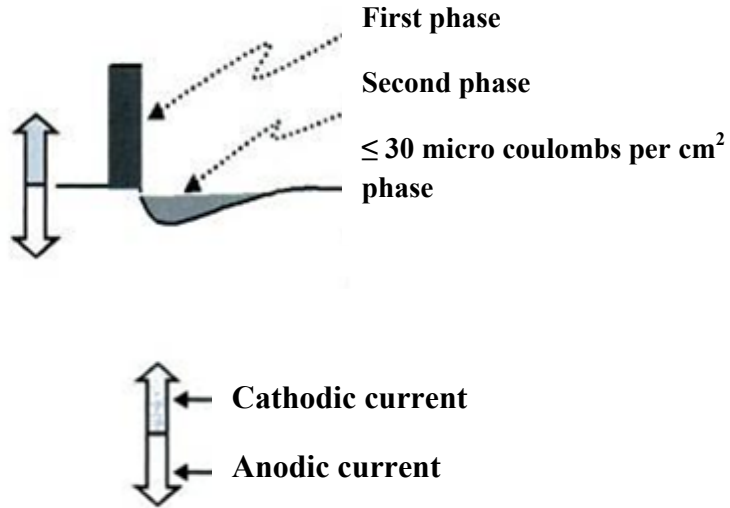


Figure 2-4 Schematic representation of stimulus pulse [17]

Actually, the amount of energy injected into the brain with each stimulation pulse is not directly controlled. Rather, the voltage level is controlled, which is indirectly related to the amount of energy injected into the brain for a given time. Since the current and voltage are related with Ohm's law through the impedance, thus, if the voltage is kept constant but the impedance is reduced, then there will be an increase in the current being delivered to the brain. So changing the DBS active contact will have an effect on the impedance, i.e. for a single contact the impedance is very high relative to multiple active contacts as shown in Figure 2-5. So that there will be an increase in the current and the charge being delivered to the brain. Hence, it is very important to know the impedance of DBS active contacts to assure that the amount of current is within the safety limit. [17].

However, another aspect of DBS electrical safety has to do with charge balanced biphasic stimulation pulses shown in Figure 2-6. If more electrical charge is passed into the brain by the cathodal (negative) current than is taken out by the anodal (positive) current then there will be a

buildup of electrical charge on the DBS contact, this residual electrical charge can cause chemical reactions at the DBS contact surface that can be dangerous for the tissue so that Biphasic current pulses are commonly used because the cathodal and anodal phases are charge-balanced yielding zero net charge [17].

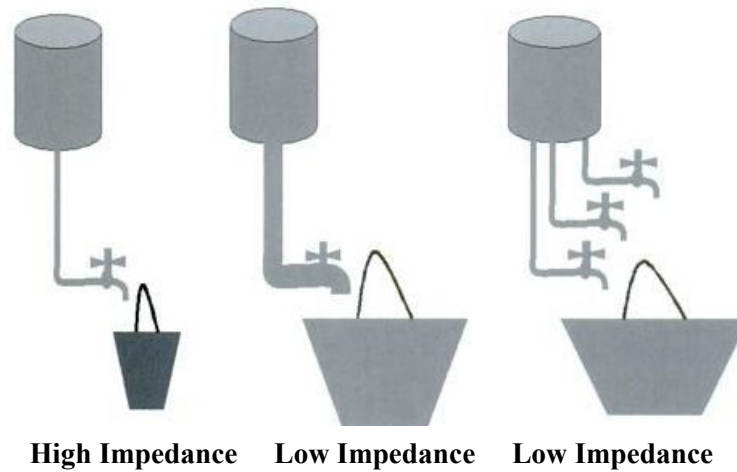


Figure 2-5 Analogy describes how multiple active contacts can lower the impedance [17]

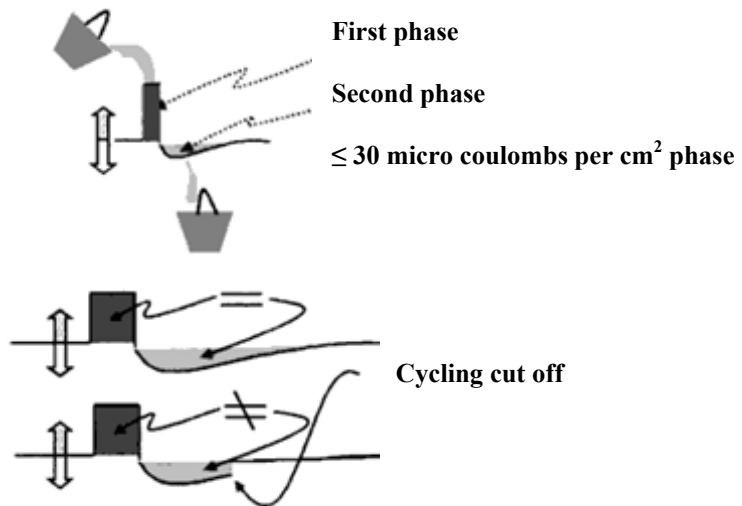


Figure 2-6 A schematic representation of the deposition and removal of electrical charge by the first and second phases [17]

2.7 Introduction to Neuronal System

2.7.1 Elements of Neuronal Systems

It is claimed that the human central nervous system is comprised of about 1.3×10^{10} neurons and about 1×10^{10} neurons are located in the brain. Some of these neurons are firing and the power dissipation due to this electrical activity is estimated to be about 10 Watts, even when asleep, 5×10^7 nerve impulses per second are being relayed back and forth between the brain and other parts of the body. This rate is increased significantly when awake [19].

Neurons are the elementary processing units in the nervous system. A small portion of this neural network is shown in Figure 2-7 by Ramón y Cajal who is one of the pioneers of neuroscience around 1900 [20]. Beside these neurons there are a large number of supporter cells called Glial-cells which are non-neuronal cells and constitute the support for neurons which provides physical support, nutrition, protection and insulations of neurons.

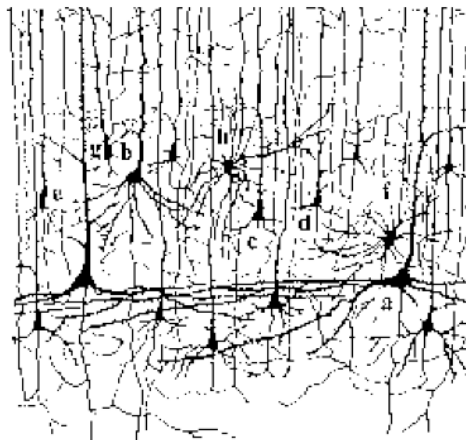


Figure 2-7 Neurons in the mammalian cortex representing cells, dendrites, and axons [20]

Neurons are responsible for processing and transmitting signals and constitute the building elements of the nervous system. According to function, neurons can be classified as shown in Figure 2-8.

- Sensory neurons (which provide inputs from sensory organs to the brain and spinal cord)

- Interneurons (carry information between other neurons only found in the brain and spinal cord).
- Motor neurons (which provide output from the brain and spinal cord to muscles and glands).

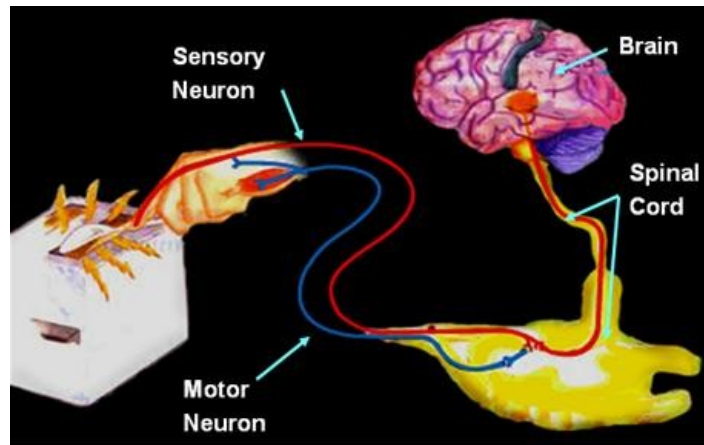


Figure 2-8 Neuron classification in the brain [21]

2.7.2 The Ideal Neuron

There are many different types of neurons but most of them have certain structural and functional characteristics in common. A typical neuron can be divided into three functionally distinct parts; dendrites, soma, and axon as shown in Figure 2-9. The dendrites which branch from the body of the neuron act as input devices which collect signals from other neurons and transmit them to the soma, the soma containing the nucleus which represents the cell body where an important nonlinear processing takes part. If the total input exceeds a certain threshold, then an output signal is generated inside the neuron which is taken by a communication means named the axon. The axon is long and fine fiber that corresponds the signals with other neurons, at the axon ends it separates making several branches called synapses which are the junctions that transmit signals from one neuron to another. It is common to refer to the sending neuron as the pre-synaptic cell and to the receiving neuron as the post-synaptic cell.

Axons are generally enclosed by a myelin sheath that is made of many wrappings of lipid as in Figure 2-9 which: Protects the axon and electrically isolates it from the extracellular fluid and increases the rate of action potential transmission. The speed of propagation down the axon

depends on the thickness of the myelin sheath. The myelin sheath is interrupted at regular intervals by narrow gaps called nodes of Ranvier [21]. Since the axons themselves are poor conductors, the action potential is transmitted as depolarization occurs at the nodes of Ranvier. The action potential effectively jumps from one node to another in a way like a regeneration amplifier to compensate for losses.

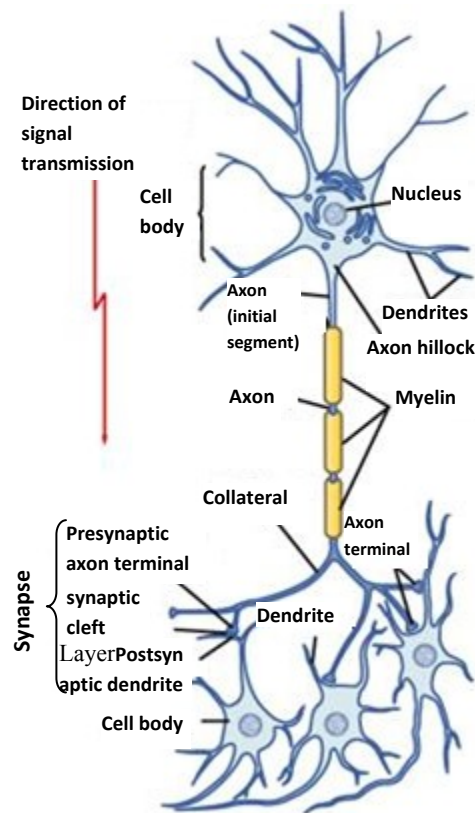


Figure 2-9 A schematic representation of a motor neuron structure neuron indicating its detailed structure and how neurons are connected through Synapses [21]

The nodes are the gaps between myelin segments that are referred to as internodes. The size and spacing of the internodes vary with the fiber diameter. The size of the nodes span from 1-2 μm whereas the internodes can be a couple millimeters or more, depending on the axon diameter and fiber type [23].

The place where the axon of a pre-synaptic neuron makes contact with a dendrite (or soma) of a postsynaptic cell is a synapse [22]. The most common is a chemical synapse as shown in Figure 2-10. At a chemical synapse, the axon terminal comes very close to the postsynaptic neuron, leaving only a tiny gap between pre- and postsynaptic cell membrane, called the synaptic

cleft. When an action potential arrives at a synapse, it triggers a complex chain of bio-chemical processing steps that lead to a release of neurotransmitter from the pre-synaptic terminal into the synaptic cleft. As soon as the transmitter molecules have reached the postsynaptic side, they will be detected by specialized receptors in the postsynaptic cell membrane and open channels so that ions from the extracellular fluid flow into the cell transferring the chemical signal into an electrical current response again.

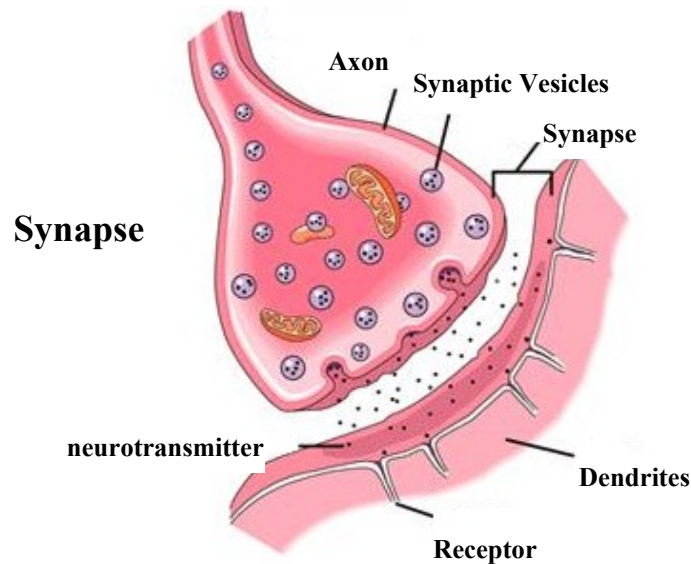


Figure 2-10 Chemical synapse structure [22]

2.8 Threshold and Action Potential

The neuronal signals consist of short electrical pulses called action potentials or spikes. It has amplitude of about 60-100 mV and typically duration of 1-2 ms., the form of the pulse does not change as the action potential propagates along the axon. Since all spikes of a given neuron are the same, the form of the action potential does not carry any information but the number and the timing of spikes matter.

The effect of a spike on the postsynaptic neuron can be recorded which measures the potential difference between the interior of the cell and its surroundings. This potential difference is called the membrane potential. Without any spike input, the neuron is at rest corresponding to a constant membrane potential. After the arrival of a spike, the potential changes and finally decays back to the resting potential as shown in Figure 2-11. It is impossible to excite a second

spike during or immediately after a first one [22, 23]. The minimal distance between two spikes defines the absolute refractory period of the neuron

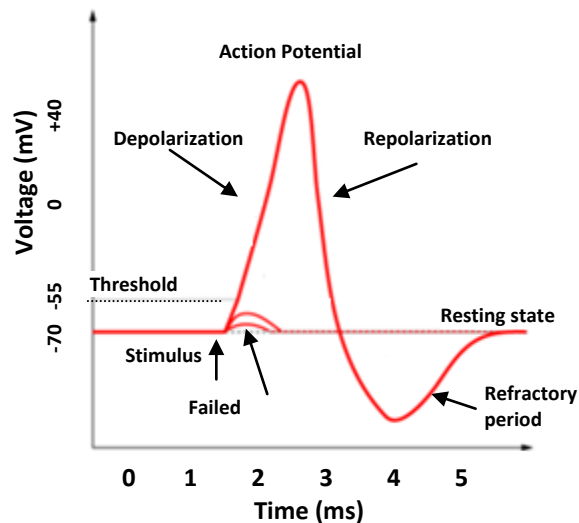


Figure 2-11 Action potential pulse levels and phases

If the change is positive, the synapse is said to be excitatory. If the change is negative, the synapse is inhibitory. At rest, the cell membrane has already a strong negative polarization of about -70mV . An input at an excitatory synapse reduces the negative polarization of the membrane and is therefore called depolarizing. An input that increases the negative polarization of the membrane even further is called hyperpolarizing.

2.8.1 Equilibrium Potential

The cell membrane consists of a thin bilayer of lipids and is a nearly perfect electrical insulator. Embedded in the cell membrane are, however, specific proteins which act as ion gates. A first type of gate is the ion pumps, a second one are ion channels. Ion pumps actively transport ions from one side to the other as shown in Figure 2-12. As a result, ion concentrations in the intracellular liquid differ from that of the surrounding.

While the sodium ions are continually removed from the intracellular fluid to extracellular fluid, the potassium ions are absorbed from the extracellular fluid in order to maintain an equilibrium condition [23]. Due to the difference in the ion concentrations inside and outside, the cell membrane becomes polarized. This difference in concentration generates an

electrical potential which plays an important role in neuronal dynamics. In equilibrium the interior of the cell is observed to be 70 mV negative with respect to the outside of the cell which is called the resting potential.

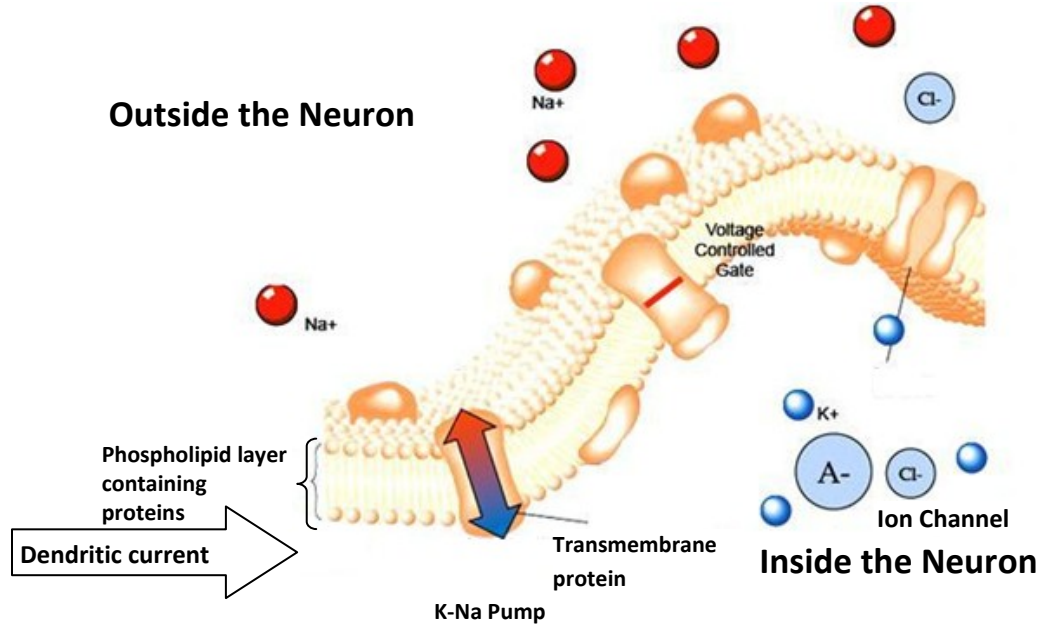


Figure 2-12 The cell membrane structure of the neuron cell [24]

2.8.2 Nernst Potential

It is known that the probability that a molecule takes a state of energy E is proportional to the Boltzmann factor k and the temperature T by the given equation:

$$p(E) \propto \exp(-E/KT) \quad (2.1)$$

At thermal equilibrium, positive ions in an electric field will be distributed so that fewer ions are in a state of high energy and more at low energy. Thus a voltage difference generates a gradient in concentration. Similarly, a difference in ion concentration generates an electrical potential. The concentration n_1 inside the neuron is different from the concentration n_2 outside the neuron. The resulting potential is called the Nernst-potential [25] that is given by:

$$\Delta V = V_1 - V_2 = \frac{KT}{q} \ln \frac{n_2}{n_1} \quad (2.2)$$

2.8.3 Reversal Potential

The sodium concentration inside the cell ($\approx 60\text{mM/l}$) is lower than that in the extracellular liquid ($\approx 440\text{mM/l}$). On the other hand, the potassium concentration inside is higher ($\approx 400\text{mM/l}$) than in the surrounding ($\approx 20\text{mM/l}$) [23]. At equilibrium the difference in concentration causes a Nernst potential $V_{NA} = +50\text{ mV}$. If the voltage difference V is smaller than the value of the Nernst potential V_{NA} more Na^+ ions flow into the cell so as to decrease the concentration difference. If the voltage is larger than the Nernst potential ions would flow out the cell. Thus the direction of the current is reversed when the voltage V is greater than V_{NA} . While in potassium $V_K = -77\text{ mV}$. It is found experimentally that the resting potential (V_M) of the membrane is about -70 millivolts. Since $V_K < V_M < V_{NA}$, potassium ions will, at the resting potential, flow out of the cell while sodium ions flow into the cell.

If V_M reaches threshold, Na^+ channels open and Na^+ influx ensues, depolarizing the cell and causing V_M to increase. This is the rising phase of an Action Potential as shown in Figure 2-13 [21]. Eventually, the Na^+ channel will be inactivated and the K^+ channels will be open. Now, K^+ effluxes and repolarization occurs. This is the falling phase of the curve. Since K^+ channels are slow to open and slow to close, this causes the V_M to take a brief dip below resting V_M . This dip is the undershoot and it is an example of hyperpolarization.

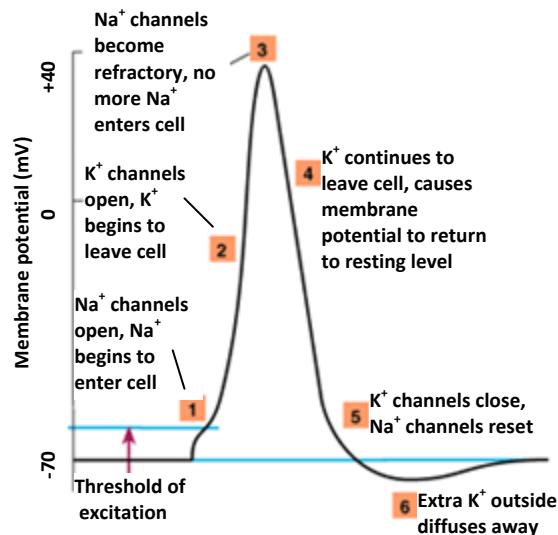
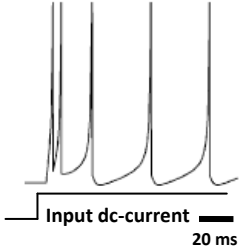
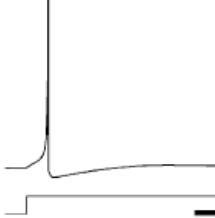
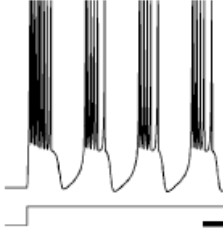
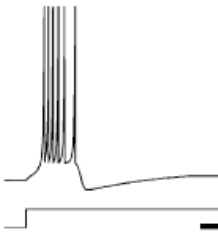


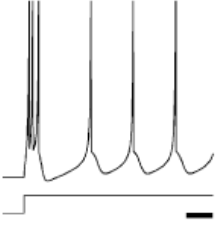
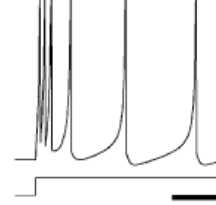
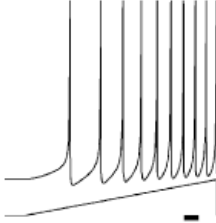
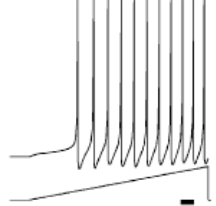
Figure 2-13 Action potential phases indicating depolarization, repolarization and hyperpolarization of the neuron cell [21]

2.9 Neuron Models Responses

There are various mathematical models that have been developed for biological neuron. These models are basically representing neural behavior in terms of membrane potential and action potential. While there is a tradeoff between detail and speed, Modeling always entails a balance between level of abstraction and computational tractability. A review of 8 of the most prominent features of biological spiking neurons has been introduced [26]. Table 2-2 introduces the spiking behavior of neurons in response to simple pulses of dc current.

Table 2-2 A review of 8 of the most biological spiking neurons responses [26]

Spiking Response	Definition
	<p>Tonic spiking - periodic spikes in response to a step in input current</p>
	<p>Phasic spiking - single spike in response to a step in input current</p>
	<p>Tonic bursting - periodic bursts of spikes in response to a step in input current</p>
	<p>Phasic bursting - single burst of spikes in response to a step in input current</p>

	<p>Mixed mode - initial burst followed by periodic spiking</p>
	<p>Spike frequency adaptation - spike frequency decreases over time</p>
	<p>Class 1 excitable - fire at low (above threshold) current and spike frequency is proportional to current</p>
	<p>Class 2 excitable - requires higher current to fire, then fires at constant, moderate Frequency</p>

No model can exhibit all of these response patterns with a single set of parameters; however, it is possible to achieve all of these behaviors using different parameter settings.

2.10 Detailed Neuron Models

Detailed neuron models can produce electrophysiological measurements to a high accuracy, but because of their complexity these models are difficult to analyze. For this reason, simple spiking neuron models are famous in neural coding. In this section we will discuss two of the most popular models of neuronal firing.

2.10.1 Leaky Integrate-and-Fire Model (LIF)

The leaky integrate-and-fire neuron (LIF) [27] is a well-known example of a spiking neuron model. The basic circuit of an integrate-and-fire model consists of a capacitor C in parallel with a resistor R driven by a current $I(t)$ as shown in Figure 2-14.

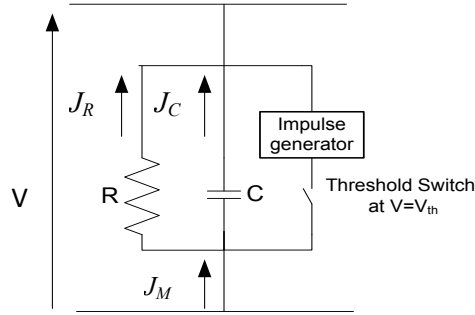


Figure 2-14 LIF neuron model [24]

The bilipid cell membrane acts like a capacitor, separating ions inside and outside the membrane; there is a passive flow of ions through the cell membrane ion channels that results in a ‘leak’ current. Neurons are firing spikes when the soma voltage passes a threshold. The spike cannot be repeated even with very high input for a short period (2ms) after a spike (absolute refractory period).

2.10.1.1 Derivation of the LIF Model

The LIF neuron is a passive RC circuit coupled to an active spike, $\delta(t)$, generator. The capacitor is the cell membrane. The current across the membrane (soma) can be found by:

$$J_M = J_c + J_R \quad (2.3)$$

Where $J_c = C \frac{dV}{dt}$ and $J_R = V/R$

J_R accounts for this passive leak of charge across the membrane. J_M is the current representing the input to the model resulting from all of the postsynaptic currents (PSCs) generated at the dendrites. It is comprised of two distinct components, the bias or background current, J^{bias} , and the drive current, J_d . Then,

$$J_M = C \frac{dV}{dt} + V/R \quad (2.4)$$

$$\frac{dV}{dt} = -1/\tau_{RC} (V - J_MR) \quad (2.5)$$

Where $\tau_{RC} = RC$

Once V crosses the neuron threshold, V_{th} , the gate denoted by τ^{Ref} closes and a delta function, $\delta(t-t_n)$, spike is generated. By short-circuiting the capacitor and resistor, the gate sets the potential across the membrane to zero (i.e., the assumed resting potential) since there is no way for a difference in charge to build up. This gate stays closed for a length of time, τ^{Ref} , equal to the absolute refractory period of the neuron as shown in Figure 2-15 [24].

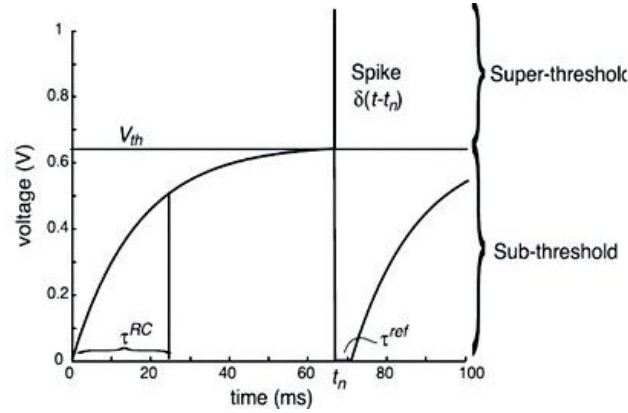


Figure 2-15 LIF spike response [24]

Evaluating the integral by assuming that the input current, J_M , is constant. This will give the firing rate as a function of the input current [24], Figure 2-16.

$$a(J_M) = \frac{1}{\tau^{Ref} - \tau^{RC} \ln \left(1 - \frac{V_{th}/R}{J_M} \right)} \quad (2.6)$$

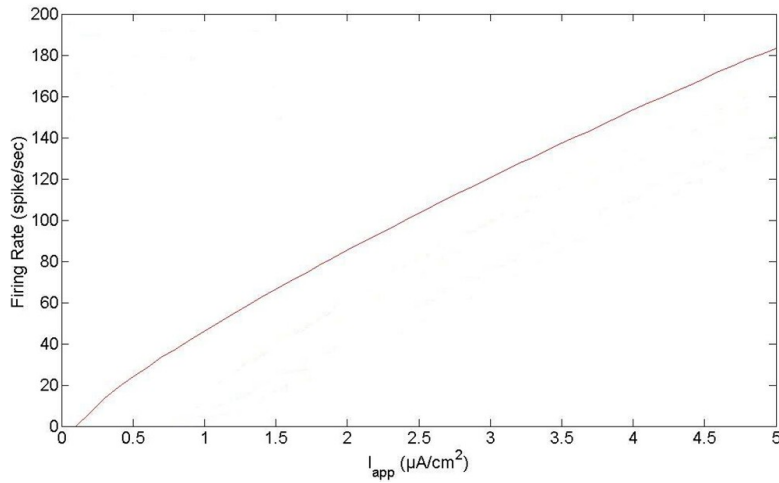


Figure 2-16 Firing rate of LIF model for a constant input current

The LIF neuron is a good model to use as a standard because of the following reasons:

- It is simple.
- It produces spikes.
- It is known to be a limiting case of more complex models.

While weaknesses of this model are:

- They are point neurons (i.e., no spatial extent; no dendrites, no axon, etc)
- Different ion conductances inside the neurons are not modeled.
- This model has many physiologically unrealistic assumptions such as R is constant, J_M is static, V_{th} is static, no adaptation, etc.

2.10.2 Hodgkin-Huxley Model

Hodgkin and Huxley [28] performed experiments on the giant axon of the squid and found three different types of ion currents; sodium, potassium, and a leak current that consists mainly of Cl^- ions. Specific voltage dependent ion channels, one for sodium and another one for potassium, control the flow of those ions through the cell membrane. The Hodgkin-Huxley model as shown in Figure 2-17 represents the cell membrane as a capacitor. The Nernst potential generated by the difference in ion concentration is represented by a battery for each ion type.

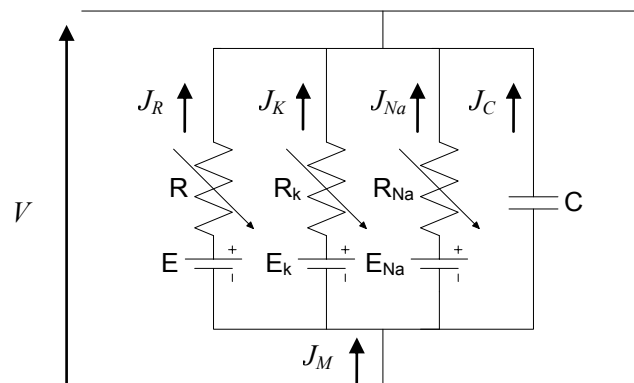


Figure 2-17 Schematic diagram for the Hodgkin-Huxley model

The current $I(t)$ may be split in a capacitive current I_C which charges the capacitor C and further components I_k which pass through the ion channels. There are only three types of channel: a sodium channel with index Na, a potassium channel with index K and an unspecific leakage channel with resistance R . The sum over all ion channels is given by [28]:

$$I(t) = I_C(t) + \sum_K I_K(t) \quad (2.7)$$

In Hodgkin-Huxley model All channels may be characterized by their resistance or, equivalently, by their conductance. The leakage channel is described by a voltage-independent conductance $g_L = 1/R$; the conductance of the other ion channels is voltage and time dependent. If all channels are open, they transmit currents with a maximum conductance g_{Na} or g_K , respectively. Normally, however, some of the channels are blocked. The probability that a channel is open is described by additional variables m , n , and h [28].

The combined action of m and h controls the Na⁺ channels. The K⁺ gates are controlled by n . specifically; Hodgkin and Huxley formulated the three current components as [28]:

$$\sum_K I_K = g_{Na} m^3 h (V - V_{Na}) + g_K n^4 (V - V_K) + g_L (V - V_L) \quad (2.8)$$

where the parameters V_{Na} , V_K , and V_L are the reversal potentials. Reversal potentials and conductances are empirical parameters listed in Table 2-3.

Table 2-3 The parameters of the Hodgkin-Huxley equations [23]

x	V_x	g_x
Na	50mV	120 mS/Cm ²
K	-77mV	36 mS/Cm ²
L	-54.4mV	0.3 mS/Cm ²

The three variables m , n , and h are called gating variables; m and n variables are to activate and h is the inactivation variable. They evolve according to the equations [28]:

$$\frac{dm}{dt} = \alpha_m(V)(1 - m) - \beta_m(V)m \quad (2.9)$$

$$\frac{dn}{dt} = \alpha_n(V)(1 - n) - \beta_n(V)n \quad (2.10)$$

$$\frac{dh}{dt} = \alpha_h(V)(1 - h) - \beta_h(V)h \quad (2.11)$$

Where the values of α and β are empirical given by Table 2-4.

Table 2-4 Values of α and β parameters of the Hodgkin-Huxley equations [23]

x	$\alpha_x(V/mV)$	$\beta_x(V/mV)$
n	$(0.1 - 0.01V)/[\exp(1 - 0.1V) - 1]$	$0.125\exp(-V/80)$
m	$(2.5 - 0.1V)/[\exp(2.5 - 0.1V) - 1]$	$4\exp(-V/18)$
h	$0.07\exp(-V/20)$	$1/[\exp(3 - 0.1V) + 1]$

The three equations (2.9-2.11) are always rewritten in the form [23]

$$\frac{dx}{dt} = -\frac{1}{\tau_x(V)}[x - x_0(V)] \quad (2.12)$$

where x stands for m , n , or h . For fixed voltage V , the variable x approaches the value $x_0(V)$ with a time constant $\tau_x(V)$ [23]. The asymptotic value $x_0(V)$ and the time constant $\tau_x(V)$ are given by equations 2.13 and 2.14 [28] and plotted in Figure 2-18 [23].

$$x_0(V) = \frac{\alpha_x(V)}{[\alpha_x(V) + \beta_x(V)]} \quad (2.13)$$

And

$$\tau_x(V) = \frac{1}{[\alpha_x(V) + \beta_x(V)]} \quad (2.14)$$

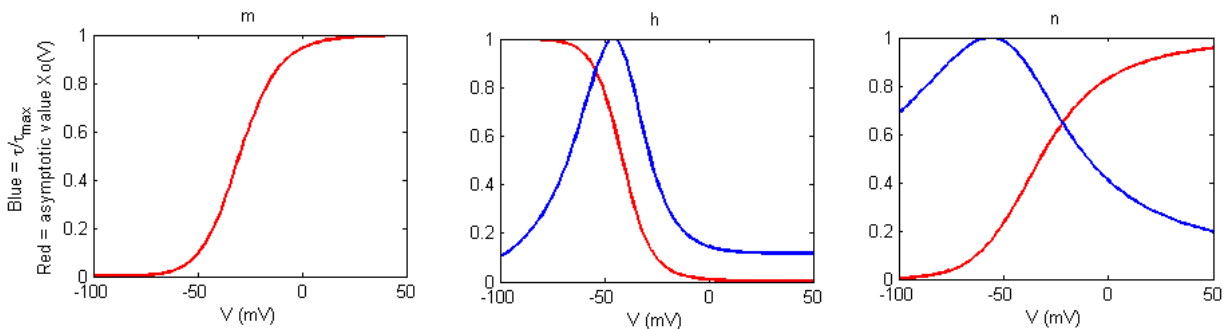


Figure 2-18 The asymptotic value $x_0(V)$ and the time constant $\tau_x(V)$ for the three variables m , n , h in the Hodgkin-Huxley model.

2.10.2.1 Advantages and Weakness of HH Model

The Hodgkin–Huxley model is one of the most important models in computational neuroscience. It consists of four equations and many parameters, describing membrane potential, activation of Na and K currents, and inactivation of Na current. It can actually exhibit all properties in Table 2-2. Such a model is important because their parameters are biophysically meaningful. The model is extremely expensive to implement. It takes large numbers of floating points relative to simple models. Thus, one can use the Hodgkin–Huxley formalism only to simulate a small number of neurons or when simulation time is not an issue [26].

2.11 Ion Channels

The equations of the Hodgkin and Huxley provide a good description of the spike generated by sodium and potassium ion channels. In Cortical neurons, there is a much richer range of electrophysiological properties than the squid axon studied by Hodgkin and Huxley. These properties are mostly due to a large variety of different ion channels [29, 30].

2.11.1 Sodium Channels

Apart from fast sodium ion channels, which are qualitatively similar to those of the Hodgkin-Huxley model and denoted by I_{Na} , some neurons contain a non-inactivating sodium current I_{NaP} [29, 30]. Non-inactivating means it is described by an activation variable m only and does not have a separate inactivation variable h given by:

$$I_{NaP} = g_{Na}m(V - V_{NA}) \quad (2.15)$$

2.11.2 Potassium Channels

Various neurons have more than just one type of potassium channel. In STN neurons, two different types of potassium channels are present, a rapidly inactivating potassium current I_K (inactivation time constant $\tau \approx 10$ ms) and a slowly inactivating potassium current I_{K2} (time constant $\tau \approx 200\text{...}2000$ ms) [31].

2.11.3 Low-Threshold and High-Threshold Calcium Current

Many central neurons contain also channels for calcium ions. Calcium currents are described in terms of a maximum permeability times a combination of activation m and inactivation h variables. Neurons of the deep cerebella nuclei, for example, contain two different types of calcium channels that give rise to a so-called high-threshold calcium current (I_L) and a low-threshold calcium current (I_T), respectively [32].

2.12 Which model should we choose?

In the previous sections many models of spiking neurons have been proposed. Which one to choose? The answer depends on the type of the problem. If the goal is to study how the neuronal behavior depends on measurable physiological parameters, then the Hodgkin–Huxley type model is the best [26]. In contrast, if you want to simulate thousands of spiking neurons in real time, then there are plenty of models to choose from. The most efficient is the LIF model as shown in Figure 2-19.

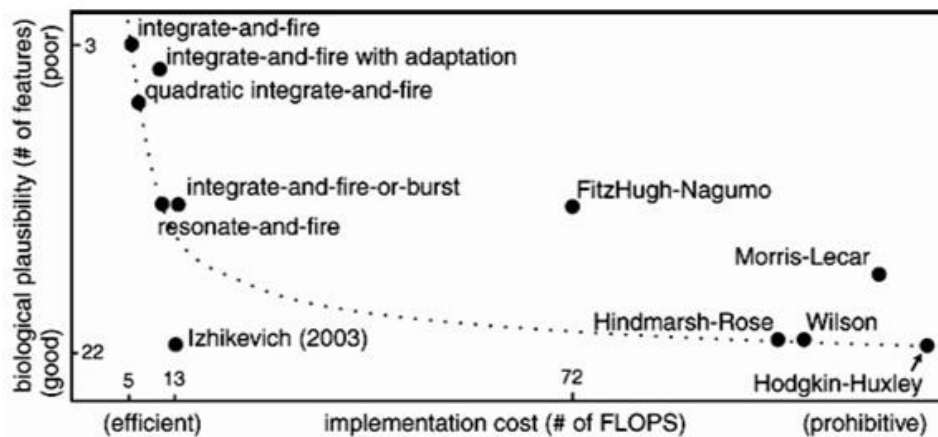


Figure 2-19 Comparison of the neuro-computational properties of spiking models [26]

2.13 Spatial Structure: the Dendritic Tree

Neurons in the cortex and other areas of the brain developed dendritic trees that may extend over several hundreds of meters. There are spatial separation of input and output, the electrical properties of point neurons have been described as a capacitor that is charged by synaptic currents and other transversal ion currents across the membrane. A non-uniform distribution of

the membrane potential on the dendritic tree and the soma induces additional longitudinal current along the dendrite [23]. To take into account these spatial structures including all types of currents, a cable equation is used to describe the membrane potential along a passive dendrite as a function of time and space.

2.13.1 Cable Theory

Consider a piece of a dendrite decomposed in short cylindrical segments of length dx as shown in Figure 2-20 by the corresponding circuit diagram. First, the voltage drop across the longitudinal resistor R_L can be given by:

$$V(t, x + dx) - V(t, x) = R_L i(t, x) \quad (2.16)$$

where $V(t, x)$ and $V(t, x + dx)$ is the membrane potential at the points x and $x + dx$ respectively. Second, the transversal current that passes through the RC is given by $C \partial V(t, x) / \partial t + V(t, x) / R_T$. According to the conservation of current at each node,

$$i(t, x + dx) - i(t, x) = C \partial V(t, x) / \partial t + V(t, x) / R_T - I_{\text{ext}}(t, x) \quad (2.17)$$

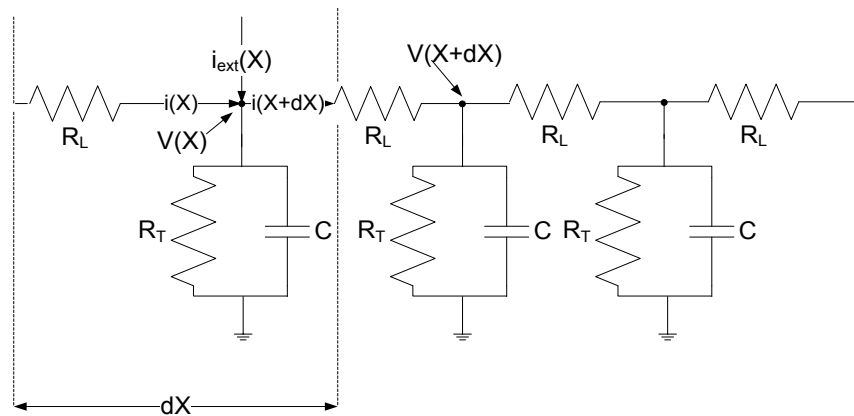


Figure 2-20 A schematic drawing of cable theory

Given that the values of the longitudinal resistance R_L , the transversal conductivity R_T^{-1} , the capacity C , and the externally applied current can be expressed in terms of specific quantities per unit length. Substituting these expressions in equations 2.16 and 2.17, dividing by ∂x , and taking the limit $\partial x \xrightarrow{\text{yields}} 0$ leads to the cable equations [23]:

$$\frac{\partial}{\partial t}V(t, x) = \frac{\partial^2}{\partial x^2}V(t, x) - V(t, x) + i_{ext}(t, x) \quad (2.18)$$

$$\frac{\partial}{\partial t}i(t, x) = \frac{\partial^2}{\partial x^2}i(t, x) - i(t, x) + \frac{\partial}{\partial x}i_{ext}(t, x) \quad (2.19)$$

The cable equations can be easily interpreted and solved by using neuron computing. These equations describe the change in time of voltage and longitudinal current.

2.14 Compartmental Models

Cable theory gives us the voltage along a passive cable with uniform geometrical and electrical properties. If we want to apply this method to describe the membrane potential along the dendritic tree of a neuron, many problems arise. Numerous bifurcations and variations in diameter and electrical properties are varying along the dendritic making it difficult to find a solution for the membrane potential analytically [33].

Numerical treatment of partial differential equations arises which requires a discretization of the spatial variable. This leads to changing derivatives with respect to space into differences by a discretizing method. In order to solve for the membrane potential of a complex dendritic tree numerically, compartmental models are used that use discretization [34].

The dendritic tree is divided into small cylindrical compartments with a uniform membrane. Each compartment is characterized by its capacity and transversal conductivity. Adjacent compartments are coupled by the longitudinal resistance that is determined by their geometrical properties as shown in Figure 2-21. And all nonlinear ion channels responsible for generating spikes are usually lumped together at the soma so that the dendritic tree is treated as a passive cable. As an example for a realistic neuron model, a model for cerebellar granule cells in a turtle was developed by Gabbiani and coworkers [35]. One of the major problems with multi-compartment models is the fact that the spatial distribution of the dendritics along the surface of the neuron is almost completely unknown.

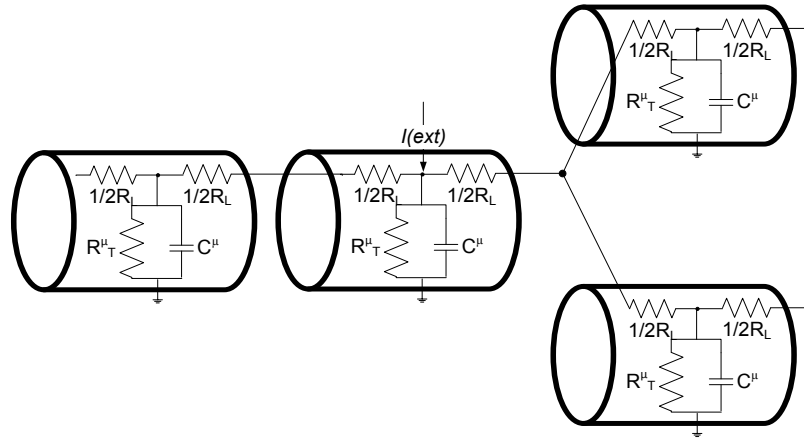


Figure 2-21 Multi-compartment neuron model [34]

2.15 Axon Models

A multi-compartment cable model of myelinated axons was proposed by McIntyre et al. [36], the models consisted of 21 nodes of Ranvier separated by 20 internodes. Each internode section of the model consisted of 2 paranodal myelin attachment segments (MYSA), 2 paranodal main segments (FLUT), and 6 internodal segments (STIN) regions of fiber as shown in Figure 2-22. The Model Geometric Parameters with fiber diameters ranging from $2 \mu\text{m}$ to $16.0 \mu\text{m}$ is listed in Table 2-5 [36, 37].

The nodal membrane dynamics included fast (Na_f) and persistent (Na_{ap}) sodium, slow potassium (K_s), and linear leakage (L_k) conductances in parallel with the nodal capacitance (C_n). A parallel combination of the membrane resistance with the membrane capacitance is connected in series with a parallel combination of the myelin resistance and the myelin capacitance. FLUT (paranode), MYSA (myelin attachment segment), R_a (axoplasmic resistance), R_p (periaxonal resistance), R_m (specific myelin resistance in Ωcm^2), C_m (specific myelin capacitance in μFcm^{-2}), C_i (specific membrane capacitance in μFcm^{-2}), R_L (specific leakage resistances in Ωcm^2) and Kf (fast K^+ channel).

Table 2-6 includes all electrical model parameters [37].

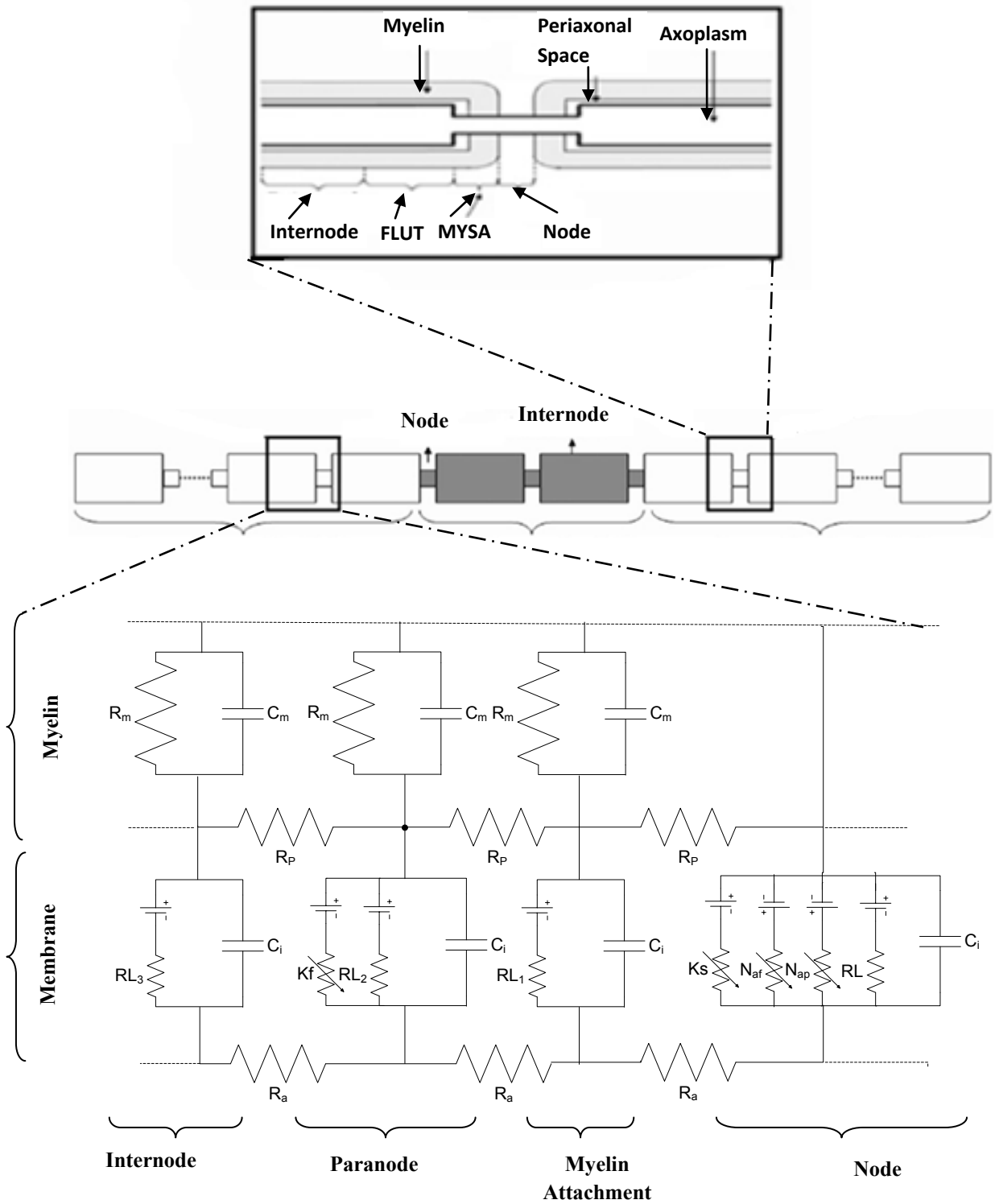


Figure 2-22 The axon segment model [37]

Table 2-5 Axon geometric parameters for different fiber diameters from 2-16 μm [36, 37].

	Fiber Diameters								
	2.0	3.0	5.7	7.3	10.0	11.5	14.0	15.0	16.0
Node-node separation (μm)	200	278	500	750	1150	1250	1400	1450	1500
Number of myelin lamella	30	43	80	100	120	130	140	145	150
Node length (μm)	1	1	1	1	1	1	1	1	1
Node diameter (μm)	1.4	1.52	1.9	2.4	3.3	3.7	4.7	5.0	5.5
MYSAs length (μm)	3	3	3	3	3	3	3	3	3
MYSAs diameter (μm)	1.4	1.52	1.9	2.4	3.3	3.7	4.7	5.0	5.5
MYSAs periaxonal space width (μm)	0.002	0.002	0.002	0.002	0.002	0.002	0.002	0.002	0.002
FLUT length (μm)	10	17	35	38	46	50	56	58	60
FLUT diameter (μm)	1.6	2.1	3.4	4.6	6.9	8.1	10.4	11.5	12.7
FLUT periaxonal space width (μm)	0.004	0.004	0.004	0.004	0.004	0.004	0.004	0.004	0.004
STIN length (μm)	57.7	79	70.5	111.2	175.2	190.5	213.5	221.2	228.8
STIN diameter (μm)	1.6	2.1	3.4	4.6	6.9	8.7	10.4	11.5	12.7
STIN periaxonal space width (μm)	0.004	0.004	0.004	0.004	0.004	0.004	0.004	0.004	0.004
MYSAs compartments between nodes	2	2	2	2	2	2	2	2	2
FLUT compartments between nodes	2	2	2	2	2	2	2	2	2
STIN compartments between nodes	3	3	6	6	6	6	6	6	6
MYSAs, myelin attachment section of paranode; FLUT, main section of paranode; STIN, intermodal section									

Table 2-6 Axon model electrical parameters [36]

Nodal capacitance (C_n)	2 $\mu\text{F}/\text{cm}^2$
Internodal capacitance (C_i)	2 $\mu\text{F}/\text{cm}^2$
Myelin capacitance (C_m)	0.1 $\mu\text{F}/\text{cm}^2$
Axoplasmic resistivity (ρ_a)	70 $\Omega\text{ cm}$
Periaxonal resistivity (ρ_b)	70 $\Omega\text{ cm}$
Myelin conductance (g_m)	0.001 S/cm^2
MUSA conductance (g_a)	0.001 S/cm^2
FLUT conductance (g_f)	0.0001 S/cm^2
STIN conductance (g_i)	0.0001 S/cm^2
Maximum fast Na^+ conductance (g_{Naf})	3.0 S/cm^2
Maximum slow K^+ conductance (g_{Ks})	0.08 S/cm^2
Maximum persistent Na^+ conductance (g_{Nap})	0.01 S/cm^2
Nodal leakage conductance (g_{LK})	0.007 S/cm^2
Na^+ Nernst potential (E_{Na})	50.0 mV
K^+ Nernst potential (E_{K})	-90.0 mV
Leakage reversal potential (E_{LK})	-90.0 mV
Rest potential (V_{rest})	-80.0 mV

2.16 Complete STN Neuron Model

A multi-compartment cable model of a STN neuron was also proposed by (McIntyre et al. [38]). This model was discovered by (Destexhe et al. [39]). It consisted of a 3-D branching dendritic tree, a multi-compartment soma and an initial segment, and a myelinated axon with explicit representation of the myelin and underlying axolemma. (Figure 2-23, Table 2-7). The cell body and dendritic compartments included the parallel combination of nonlinear fast Na^+ , delayed rectifier K^- , slow K^- , T-type Ca^{2+} , Na^+ , K^- linear leakage conductances, and the membrane

capacitance. The initial segment compartments included the parallel combination of nonlinear fast Na^+ , delayed rectifier K^+ , slow K^+ conductances, a linear leakage conductance, and the membrane capacitance as shown in Figure 2-23 and Table 2-8.

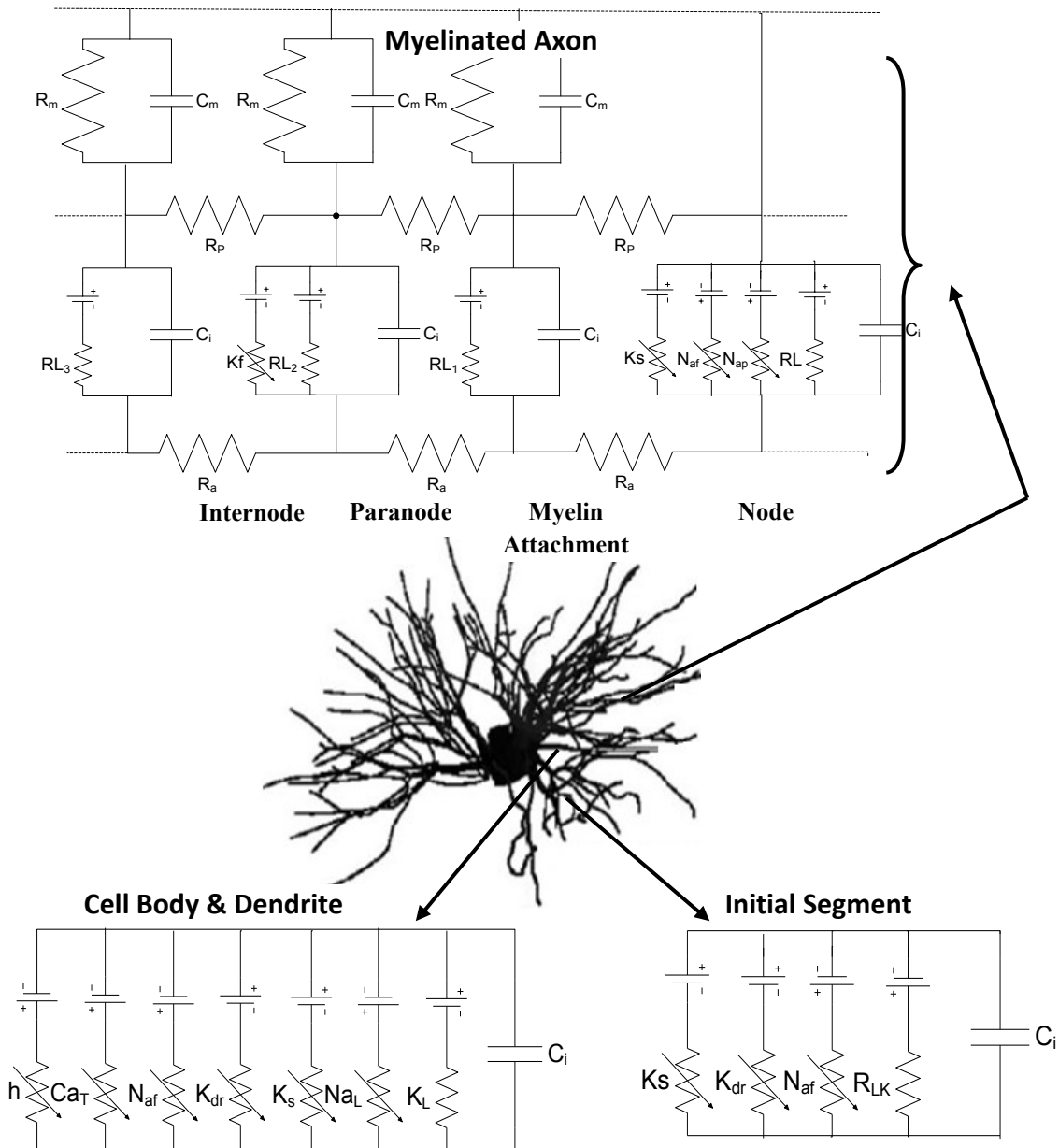


Figure 2-23 Cable model of a STN neuron [38]

Table 2-7 STN model geometric parameters
[38]

Cell body	
Soma compartments	3
Soma surface area	3.171 μm^2
Initial segment compartments	3
Initial segment surface area	173 μm^2
Dendrites	
Dendritic compartments	251
Primary dendrites	11
Dendritic surface area	21.356
Myelinated axon	
Fiber diameter	2 μm
Number of myelin lamella	30
Node length	1 μm
Node diameter	1.4 μm
MYSa length	3 μm
MYSa diameter	1.4 μm
MYSa periaxonal space width	0.002 μm
FLUT length	10 μm
FLUT diameter	1.6 μm
FLUT periaxonal space width	0.004
STIN length	57.7 μm
STIN diameter	1.6 μm
STIN periaxonal space width	0.004 μm

Table 2-8 STN cell body and dendrite electrical parameters [38]

Na ⁺ Nernst potential (E_{Na})	45 mV
K ⁺ Nernst potential (E_{K})	-95 mV
Leakage reversal potential (E_{LK})	-70 mV
Soma and dendrite	
Max. T-type Ca ²⁺ permeability (P_{CaT})	0.0001 cm/s
Max. fast Na ⁺ conductance (g_{NaF})	0.03 S/cm ²
Max. delayed rectifier K ⁺ conductance (g_{Kdr})	0.003 S/cm ²
Max. slow K ⁺ conductance (g_{Ks})	0.0007 S/cm ²
Max. I _h conductance (g_{h})	0.0005 S/cm ²
Na ⁺ leakage conductance (g_{NaL})	0.00095 S/cm ²
K ⁺ leakage conductance (g_{KL})	0.00005 S/cm ²
Initial segment parameters	
Max. fast Na ⁺ conductance (g_{NaF})	0.3 S/cm ²
Max. delayed rectifier K ⁺ conductance (g_{Kdr})	0.03 S/cm ²
Max. slow K ⁺ conductance (g_{Ks})	0.007 S/cm ²
leakage conductance (g_{LK})	0.00005 S/cm ²

2.17 Rate versus Time Codes

The information (code) that comes from the spiking of neurons can be defined by:

- 1- Rate codes (Temporal Average): The firing rate of the neuron is what carries information.
- 2- Timing codes: The precise pattern of spike generation carries information.

The firing rate is usually defined by a temporal average as shown in Figure 2-24. A time window of $T = 100\text{ms}$ or $T = 500\text{ms}$ is set and counts the number of spikes $n_{sp}(T)$ that occur in this interval then the mean firing rate is equal to: $a = n_{sp}(T)/T$

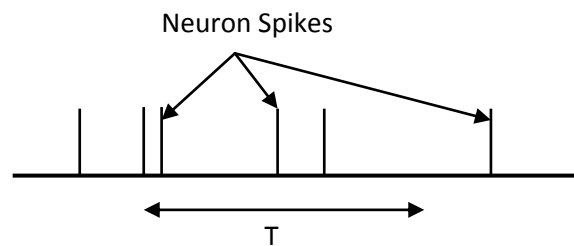


Figure 2-24 Mean firing rate vs. a temporal average

Measurement of firing rates is considered a standard tool for describing the properties of all types of sensory or cortical neurons [40]. Temporal averaging can work well in cases where the stimulus is constant or slowly varying since it neglects all the information possibly contained in the exact timing of the spikes.

The other type of coding which is the time code, the exact time at which the firing occurs is very important and has to be determined precisely in order to get the full neuron information. In this case the temporal details of the input signal $x(t)$ are a significant measure in order to reconstruct the stimulus input and do a reverse correlation.

2.18 Summary of the Survey

Deep Brain Stimulation explores the functionality of biological neural networks in processing sensory information and controlling different motor functions. The administration of high-frequency continuous electrical stimulation to the subthalamic nucleus (STN) through a surgically implanted device has been shown to improve motor symptoms in patients with advanced stages of Parkinson's disease. The progress of DBS requires understanding and quantifying the functionality of biological neural networks in processing sensory information and controlling different motor functions.

The signal processing in the brain takes place by the neurons which provide access to motor intent and sensory perception. There are various mathematical models that have been developed for biological neurons. These models are basically representing neural behavior in terms of membrane potential and action potentials. While there is a tradeoff between detail and speed, the proposed DBS modeling will deal with the H-H cell model with all its compartment details for the STN regions as discussed in section 2.16. This proposed model will describe the spiking rate activity that comes from the neural structure that is surrounded by the DBS electrode and hence it takes into consideration the applied physical parameters to the electrode.

Chapter 3

Proposed Interactive Real Time Comprehensive DBS System

3.1 Introduction

The Deep Brain Stimulation (DBS) problem is tackled in this research from an engineering point of view. DBS employs electrical stimulation of a specific part of the brain called the subthalamic nucleus (STN), a small but integral part of the basal ganglia. Different types of motor disorders have been treated by this electrical stimulation produced from an implanted electrode inside the brain.

The main goals of this research are to determine the DBS stimulation parameters and to develop a brain neuron model that can be readily used in DBS analysis. We will also study the effect of these stimulation parameters on the neurons firing activity. In order to achieve our goal, we propose a model that we named the DBS model. Figure 3-1 shows a schematic diagram for input and output components of the proposed DBS model.

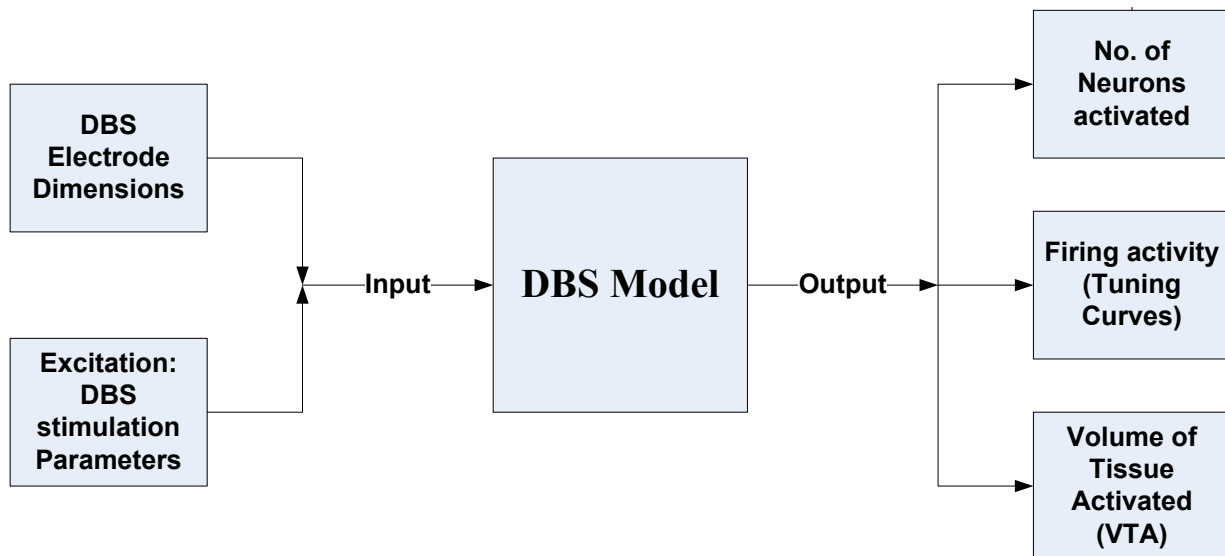


Figure 3-1 A schematic diagram of the proposed DBS model with its input and output parameters

To have a complete quantitative analysis of the DBS problem, we develop a DBS model that its input is controlled by the DBS stimulation electrode and the stimulation parameters applied on this electrode as an excitation to our model. The output of this model represents the region in the brain that is excited through the numbers of neuron that are activated, the firing activity of the neurons which will be used to build the neurons tuning curves and finally the volume of tissue activated (VTA).

The proposed DBS model has many components and phases of interaction to build up the real time comprehensive DBS model as shown in Figure 3-2.

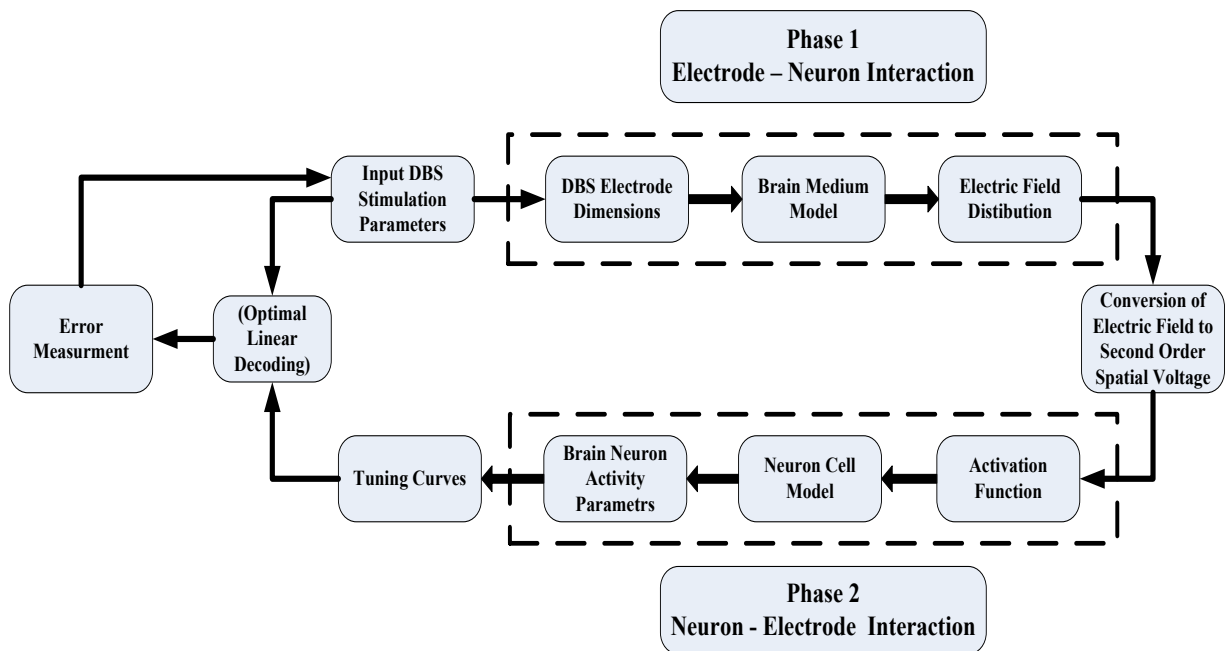


Figure 3-2 A complete detailed diagram of the proposed DBS model

There are two main phases of interaction in our DBS model: Electrode-Neuron Interaction and Neuron-Electrode Interaction. The first interaction phase is responsible for calculating the electric field distribution inside the brain medium due to the DBS electrode. While the second phase is developed for calculating the neuron firing activity from the neuron cells due to the calculated activating function.

DBS stimulation parameters are the input to the DBS model and play an essential role in stimulating the brain neural cells through the electric field intensity produced by the DBS electrode. To find the electric field distribution produced by the DBS electrode, we are going to introduce the brain as passive medium which means that taking into account only its microscopic properties (conductivity and permittivity). Of course the electric field intensity distribution that comes from this step is not accurate since the brain neurons have in themselves an electric charge which also produces an electric field. Therefore to study these phenomena of DBS interaction with brain neurons we need to use some sort of superposition theory; stimulation parameters applied on the DBS electrode produced electric field and brain neurons at this stage have no electric effect (i.e., voltage source is short circuit as in superposition theory in circuit) then we activate the neurons and the electrode has no applied electric effect. In our model we need two additional processes to implement this superposition theory; the conversion of the electric field to second order spatial voltage and the optimal linear decoder filter.

Thus to have a complete study of the DBS problem and taking into consideration the charge distribution of the neuron cells (as our neurons now no longer behave like a switch on/off firing elements as many previous research proposed [18,38]), two components were added between the two interaction phases. The first component is responsible for the conversion from electric field distribution to the activating function, while the other component is the optimal linear decoder which is responsible for calculating the stimulation parameters and applied them back to the DBS electrode. Thus by minimizing the error between the applied electrode stimulation parameters and the estimated ones, the DBS model will be completed.

3.2 The Main Components of the DBS Model

As we mentioned in the last section, the proposed DBS model is divided into two phases of interaction to build up the real time comprehensive DBS model. In this section we define the components inside this model.

We start with a standard DBS electrode manufactured by Medtronic which is an FDA approved. This electrode will be the source of the electrical stimulation which is controlled by pulse width, amplitude and frequency. All of these values will be taken from a standard experiments conducted with the DBS problem. However, we will study the impact of changing

the DBS input parameters on the electric field distribution and the volume of tissue activated (VTA) during the stimulation process of the brain as shown in Figure 3-3.

The DBS electrode in this stage of the analysis is assumed to be inserted in a brain medium that does not account for the charges inside the neurons and their coupling to the brain medium. Therefore, the Laplacian equation is used to find the electric field distribution inside the passive brain region.

In a charge-free region of space, Laplace's equation is given by:

$$\nabla^2 V = 0 \quad (3.1)$$

which is the divergence of the gradient of an electric potential.

The study will include the effect of the characteristics of different brain tissue layers (different dielectric properties such as permittivity and conductivity) on the electric field distribution. We will start with the case of a homogeneous and isotropic tissue medium, rather than biophysically based conductivities. Next we will use inhomogeneous medium. Also, we will take into account the low conductivity encapsulation layer that surrounds the electrode *in vivo* and limits the spread of electric field around the electrode and can reduce the VTA

In order to proceed to the second phase of the interaction and to calculate the neuron firing rates (spikes/s.) and the volume of tissue activated (VTA) within the brain, we have to measure the second spatial difference of the field's electric potential, known as the activating function. The concept of this function was developed and suggested in [41]. This function is defined as the second derivative of the extracellular potential along the neurons axon and represents the driving function of the cable equation for the neurons for studying its firing pattern and activity. Thus the brain region under study becomes an active medium due to this introduced neural coupling. This activating function will take into consideration all of the issues that control the electric fields within the brain, i.e., DBS electrode configuration and DBS stimulation pulse width, amplitude and frequency. We will study the firing of neurons evoked by the activating function during DBS and the electrophysiological parameters will be implemented through computer simulations.

There are many neural cell models that describe the dynamic behavior of the neural cell, but in this research we are going to focus on the Hodgkin-Huxley model. The population and distribution of these neural cells will vary in order to study their effect on the VTA as shown in Figure 3-3. Also, the proposed DBS model will address the position of the electrodes with respect to the neuron axons orientation which has the effect on facilitating the inward current flow into the cell and hence maximal depolarization and firing.

All of the performance analysis will make the proposed DBS model robust. Our goal is to study the immediate direct effects of the stimulating field and examine where the beneficial effects of DBS originate since the mechanism of DBS is not yet fully understood and hence a comprehensive performance study will be done for the DBS problem.

The research proposed in this chapter is a novel approach to study the interaction between the DBS electrode and the firing activity of brain neural cells. This approach will lead to better understanding of the DBS problem in real time. Our target is to build a complete DBS model that is capable to interact with the DBS problem in a forward and backward relation. In the forward manner for certain stimulation parameters applied to the DBS electrode we will be able to calculate the neural firing activity and the volume of tissue activated. In the backward manner we will use the measured firing activities to calculate the stimulation parameters. Thus, a closed loop system will be established to develop the proposed DBS model.

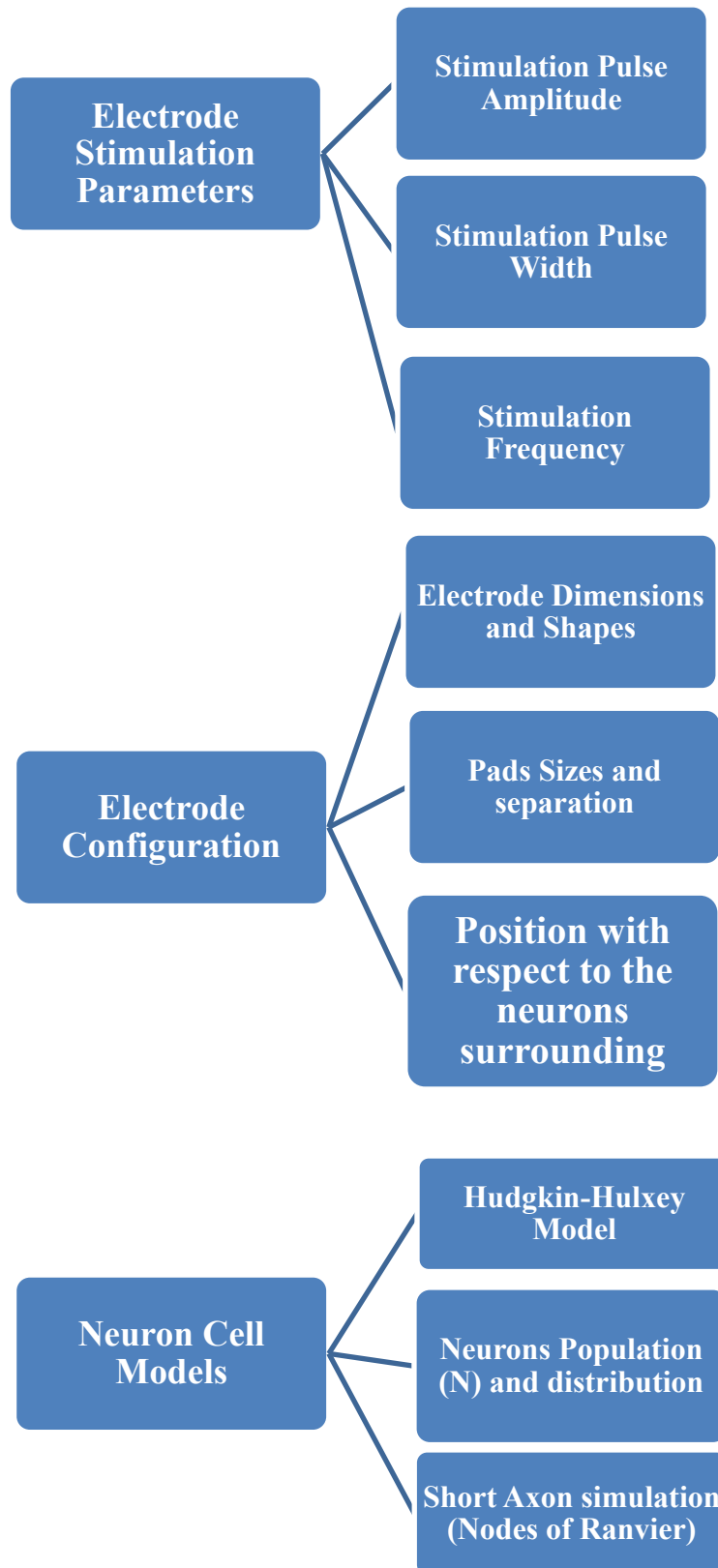


Figure 3-3 A detailed flow chart of some of the components in the proposed DBS model

3.3 Methodology

3.3.1 Electrode Modeling

Progress in DBS techniques requires the knowledge of the brain response to electrical stimulation which is manipulated by the electric field distribution within the brain tissue. This motivated the development of simulation models for the implanted Medtronic 3387 DBS electrode (Medtronic Inc, Minneapolis, MN) in order to estimate the electric field distribution in an ambient brain. Since the electric field is dependent on the electrode geometry, the distribution of pads contact and their separation are one of the goals of this proposal. We are planning to quantitatively evaluate a range of DBS electrode parameters and examine the effects of electrode geometry on the VTA by varying the height and radius of the electrode contact to maintain a constant surface area. In all cases, the results are evaluated relative to the Medtronic 3387 electrode contact dimensions (1.27 mm diameter, 1.5 mm height, 5.98 mm² surface areas)

3.3.2 Brain Modeling

Different brain tissue medium (permittivity and conductivity) have a specific response to the electric fields. The permittivity and conductivity of brain tissues are frequency dependant; as frequency decreases, conductivity drops and the dielectric constant increases remarkably. The values for the dielectric properties of brain tissue were extracted from a parametric database of biological tissue which was developed based on the Gabriel model [42-44]. As a first step, we will start to model the STN inside the brain as a homogeneous layer of a lossy dielectric with isotropic and frequency independent characteristics disregarding the anatomical details of the brain. Next, we will propose the inhomogeneous tissue medium.

3.3.3 Electric Field Solver

We apply two approaches to calculate the electric field intensity within the brain; these two solvers are the Finite Difference Time Domain (FDTD) technique and the Finite Element Method (FEM). For both methods of solving, a detailed model of the electrode and the brain tissue mediums is built and simulated. In the FDTD model, we solve time domain computational electrodynamics modeling technique developed for solving time-dependent Maxwell's equations. While in the FEM model, we solve the Laplace equation to find the tissue medium. The problem

with the FEM is that it doesn't account for the time dependence of the stimulus waveform. In order to address this problem, we use a Fourier decomposition of the stimulus signal and solve the Laplacian equation at multiple frequencies to calculate the voltage distribution due to this time-dependent stimulus waveform.

3.3.4 Stimulation Waveform

Electric field intensity calculated from the previous sections is depending on the stimulation input signal parameters which are localized in the stimulated amplitude (V), pulse width (μs), and frequency (Hz). Each of these parameters have a direct effect on our models and hence on the VTA. According to DBS experimental results, the stimulus amplitude is changing from 1-10 volts in an increment of 0.5V [45], while the pulse width is changing from 60 and 450 μs and the stimulation frequency ranging from 100-185Hz [45]. We will address all of these parameters and build quantitative equations that describe these relations.

3.3.5 Neural Modeling

The activating function of the neuron which is the second spatial difference of the extracellular potential distribution along the brain is providing an estimate of the polarization of the neuron in response to an applied electric field and can be used to predict action potential initiation. This activating function is coupled to the neurons surrounding the electrode through NEURON v7.0 program [46]. Then, this action potential prediction determines the neuron spiking activity (firing rate) and the VTA.

We propose a complete neuron model that interacts with this activating function, we not only deal with the axons model but we also take into effect the neuron cell body using Hodgkin-Huxley which concerns about the dynamics of the action potential inside the cell, H-H model takes into consideration the adaptation of the firing rate and hence all of temporal neuron spiking data. For the axon models used in this research, we use a multi-compartment cable model of myelinated axons (5.7 μm) proposed by McIntyre et al [36]. We focus on a short axon length with 4 nodes of Ranvier.

We start with a neuron population (N) uniformly spaced and perpendicular to the electrode shaft in a matrix form. A comparison is made on the percentage of neurons that are firing and hence affecting the calculation of VTA. Another issue studies the neurons orientation with respect to the position of the electrode shaft. We change this orientation angle between the two extreme scenarios which are the perpendicular and parallel cases.

In the next section, the algorithm that estimates the electrode stimulation parameters is proposed based on the study of the spiking activity measured at the neuron level.

3.3.6 Neuron Decoding

To find the accurate decoding of neural firing activity representing the input parameters, we propose a linear filter analysis decoding algorithm that deals with neuron rate codes (temporal average).

3.3.7 Linear Filter Technique

We define the biological representation as encoders representing the neurons, and the decoding is linear with unknown weights [24]. We then have an encoder:

$$a_i(x) = G_i[x] \quad (3.2)$$

Where $a_i(x)$ is called the tuning curve (spikes/s.) that directly relates an external signal, x , to neural responses a_i , $G_i[x]$ is a non linear function that is neuron cell dependent. One of the most neurally plausible cell models is the leaky integrate and- fire (LIF) model which was discussed in Chapter 2 section 2.10. Then the decoder is given by a linear representation as:

$$\hat{x} = \sum_i a_i(x)\varphi_i \quad (3.3)$$

Where i indexes the neuron number, x is the physical external signal and φ the weighting function, we want the error between x and the estimate, \hat{x} , to be small over the range of signal so that:

$$\text{Minimize } \langle (x - \hat{x})^2 \rangle_x \quad (3.4)$$

We normalize the range of the input signal from 0 to 1 so that the error is given by:

$$E = \int_0^1 [x - \sum_{i=1}^N a_i(x)\varphi_i]^2 dx \quad (3.5)$$

To minimize this error we differentiate with respect to φ_i to calculate the MMSE.

$$\frac{\partial E}{\partial \varphi_i} = - \int_0^1 2[x - \sum_j^N a_j(x)\varphi_j]a_i(x)dx \quad (3.6)$$

$$0 = -2 \int_0^1 a_i(x)x dx + 2 \int_0^1 \sum_j^N a_i(x)a_j(x)\varphi_j dx$$

$$\int_0^1 a_i(x)x dx = \sum_j^N \left(\int_0^1 a_i(x)a_j(x)dx \right) \varphi_j$$

This can be written using matrix vector notation

$$Y = \Gamma\Phi \quad (3.7)$$

then

$$\Phi = \Gamma^{-1}Y$$

Where

$$\Gamma_{ij} = \langle a_i(x)a_j(x) \rangle_x$$

This is defined as the Gram matrix or the correlation matrix and can be written as:

$$\Gamma_{ij} = A^T A \quad (3.8)$$

Where A matrix ($N_\Delta \times N$) is the transpose of the neuron tuning curves. Let the input signal x be discretized by interval Δx such that we have N_Δ steps then:

$$A^T = \begin{bmatrix} a_1(x_{min}) & a_1(x_{min} + \Delta x) & \dots & a_1(x_{max} - \Delta x) & a_1(x_{max}) \\ a_2(x_{min}) & \vdots & \dots & \vdots & a_2(x_{max}) \\ \vdots & \vdots & \dots & \vdots & \vdots \\ a_{N-1}(x_{min}) & \vdots & \dots & \vdots & a_{N-1}(x_{max}) \\ a_N(x_{min}) & a_N(x_{min} + \Delta x) & \dots & a_N(x_{max} - \Delta x) & a_N(x_{max}) \end{bmatrix} \quad (3.9)$$

So Γ_{ij} is a $(N \times N)$ matrix while,

$$Y_i = \langle x a_i(x) \rangle_x = A^T X \quad (3.10)$$

Where X is a $(N_{\Delta} \times 1)$ matrix then

$$\phi_i = \sum_j^N \Gamma_{ij}^{-1} Y_j = \Gamma^{-1} Y = (A^T A)^{-1} A^T X \quad (3.11)$$

Which is a $(N \times 1)$ matrix, and then the estimate signal is given by [24]:

$$\begin{aligned} \hat{X} &= A\phi \\ &= A(A^T A)^{-1} A^T X \end{aligned} \quad (3.12)$$

3.3.8 Singular Value Decomposition (SVD)

The major assumption in the previous technique is that we can take the inverse of the Γ matrix but because this matrix has no noise term and hence some tuning curves that are likely to be similar for a large population [24], the matrix Γ is likely to be singular or not invertible. That is why we have to use Singular Value Decomposition (SVD) in analyzing such matrices.

SVD decomposition of a $M \times N$ matrix, B is a result of this factorization which gives three matrices whose products gives B such that:

$$B_{M \times N} = U_{M \times M} S_{M \times N} V_{N \times N}^T \quad (3.13)$$

- Obtaining an approximation of the original matrix is quite easy. This is done by truncating the three matrices obtained from a full SVD. Essentially we keep the first k columns of U , the first k rows of V^T and the first k rows and columns of S ; that is, the first k singular values. This removes noisy dimensions and exposes the effect of the largest k singular values on the original data.
- The reduction process is illustrated in Figure 3-4 and is often referred to as "computing the reduced SVD", dimensionality reduction or the Rank k Approximation.

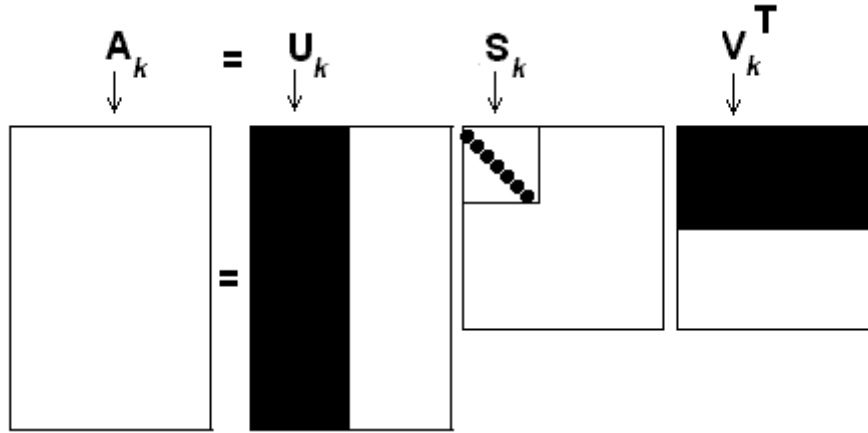


Figure 3-4 The reduced SVD or rank approximation

In case when B is square and symmetrical as the Gram matrix Γ , this can be simplified to:

$$\Gamma = USU^T \quad (3.14)$$

or in summation notation,

$$\Gamma_{ij} = \sum_m U_{im} S_m U_{jm} \quad (3.15)$$

In the case where Γ is singular, some elements of S are zero or very small so the inverse of S will include infinite or very large terms which is an indication that the matrix Γ is ill-matrix. So that the SVD is defined where for $S_i = 0$, the inverse is set to zero.

Thus, given the properties of SVD, we guarantee that our optimal decoding functions that minimizing the error is given by:

$$\phi = US^{-1}U^T A^T X \quad (3.16)$$

3.4 Challenges

One of the challenges that we are facing in this research is to have a measured imaging or 3D model anatomy to the STN regions which act as a representative stimulation target to have biophysically based conductivities, our model is highly simplified in comparison with the real basal ganglia.

Another challenge is to find clinical and experimental recorded data that we can use to verify our models and give us a close insight about how close or far our estimation input parameters are from real and experimental data.

3.5 Conclusion

In this chapter, a complete proposal for the DBS model has been introduced. The proposed algorithm is a novel approach to study the interaction between DBS electrodes and the neuron world. The proposed model is capable of quantifying and analyzing the spiking rate activity and to estimate the DBS parameters that were applied to the electrode and hence a reverse engineering concept can be applied to determine the proper input parameters of the DBS electrode needed by a physician to stimulate a given part of the brain.

This proposal is a fundamental step toward the full understanding of mechanisms and effects of the DBS problem and in order to gain a complete optimization of the DBS technique. In the next three chapters, the implementation of the DBS model and the results that come from applying these proposed algorithms are discussed.

Chapter 4

The Effect of Medium Brain Tissue and Stimulation Pulse Parameters on the Electric Field Distribution in a Deep Brain Stimulation System

4.1 Introduction

As mentioned in the literature survey, the advancement of electrotherapeutic techniques requires qualitative and quantitative perception of the brain response to electrical stimulation which is controlled by the electric field distribution within the brain tissue. Many papers concerned with the quantitative description of electric field inside the subthalamic brain tissue have been published [51, 72], but all of these previous studies have assumed that the DBS electrode is located in a large homogenous isotropic medium as in free space. Our contribution in this research is that we build a model for a DBS electrode inside the brain taking into effect the low conductivity encapsulation layer that surrounds the electrode *in vivo* and limits the spread of electric field around the electrode which can reduce the VTA. Also, due to the lack of information on the exact position of the DBS electrode inside the STN which consist of Grey tissue matter surrounded by a region of White tissue matter, we studied the position of the DBS electrode with respect to the boundary regions between the White and Grey tissue matter and how this affects the electric field distribution around the DBS electrode. This motivated us to develop simulation models for implanted DBS electrodes in order to estimate the electric field distribution in ambient brain tissue.

This chapter introduces modeling, simulation and analysis of an implanted Medtronic deep brain stimulation (DBS) electrode. The analysis are developed using the finite difference time domain (FDTD) method (which is a time-domain analysis) and a single simulation run with a wide frequency range is used to calculate the electric field due to the DBS electrode. While the simulation is applicable to electrodes with uniform and non-uniform shapes, we will focus in the analysis in this proposal on the Medtronic 3387 DBS electrode (Medtronic Inc., Minneapolis, MN) because it is FDA approved commercial electrode.

In this study we focus on three different situations of the implanted electrode inside brain tissue, starting with the electrode represented and surrounded with a homogenous and isotropic

brain tissue medium (Model-I) which represents the main Grey tissue matter of the STN and this will be our basic brain model to study the influence of brain tissue dielectric properties (permittivity and conductivity) on the electric field distribution around the DBS electrode. Moreover as we explained earlier, the encapsulation layer surrounding an implanted electrode will be added to the basic brain model, thus we have Model-II which represents the aging process of implanted electrode inside brain tissue. Finally a non-homogenous tissue structure situation which will be presented in Model-III includes the Grey and White tissue matters in order to investigate the effect of the electrode position with respect to different tissue layers. All three models were investigated to study their effect on the electric field distribution. Also, the effect of DBS pulse parameters (amplitude, width and frequency) on controlling the electric field distribution inside brain tissue Model-I have also been discussed in this chapter.

These analyses are used to provide a relationship between brain tissue properties, the DBS electrode configuration, DBS stimulation parameters and the electric field inside the brain. A quantitative formulation of all of the previous issues is created for predicting the field distribution within brain tissue and estimating the volume of tissue activated (VTA).

Moreover, the voltage distribution in brain tissue is calculated from the electric field values as is shown in Chapter 5. This voltage distribution is our input to the neurons surrounding the electrode through the activating function concept that was discussed before. The firing neurons activity is executed using the NEURON program which is the link between the calculated electric field distribution and the neuron models shown in Chapter 6. This will finally allow us to find the interaction between the inputs and the outputs of the proposed DBS model.

Information elicited from the simulation results will provide:

- Guidelines for the design specifications and development of new DBS electrodes as well as the optimum electrode configuration, pad geometry and layout that are best fit for DBS operation.

4.2 Brain Tissue Properties

The brain tissue represents the ambient medium in which the electrode is implanted. The dielectric properties of these tissues affect the electric field distribution inside the brain and thus control the neurons responses to the applied electric fields produced by stimulation. Brain tissue dielectric properties (dielectric constant and conductivity) are functions of frequency [49]. An accurate brain tissue model has to embrace detailed data covering the bandwidth being studied. At extremely low frequencies (<100Hz); dielectric constant of body tissue can reach values of 10^6 or 10^7 [42] and conductivity drops to a few milli-Siemens per meter ($\text{mS}\cdot\text{m}^{-1}$) [49, 50]. As frequency increases, conductivity increases and the dielectric constant values drop along the spectrum.

4.2.1 Brain Conductivity

Different materials have specific responses to externally applied electric fields; this can be expressed by dielectric material properties. Values for brain tissue conductivity range between $0.05 - 3.3 \text{ S}\cdot\text{m}^{-1}$, the exact value depends on the type of brain tissue and the anisotropic electric characteristics of the biological tissue [50]. The composition of brain tissue differs according to the species (rodents, primates and humans) and this affects the conductivity as well as the dielectric constant values. Moreover, different tissue types (e.g. White matter, Grey matter and encapsulation tissue) have different conductivities and directivity. Table 4-1 lists the average low frequency conductivity values used in modeling brain tissue [51-56].

4.2.2 Brain Permittivity

In studying the effect of time varying fields, complex permittivity ($\hat{\epsilon}$) is used to model the tissue response and express the phase shift of polarization with respect to the polarization field as well as the magnitude represented by ϵ'' and ϵ' respectively:

$$\hat{\epsilon} = \epsilon' - j\epsilon'' \quad (4.1)$$

Complex permittivity is a function of frequency and it exhibits dispersions through the spectrum. Experimental data collected was modeled in several forms. Several models were developed to represent the experimental dielectric properties data (e.g. Debye and Cole-Cole

models) and a parametric biological tissue model database was developed [42] and adopted by commercial simulation tools.

Table 4-1 Mean values for brain tissue conductivity

Tissue	σ [S.m⁻¹]	Reference
Bulk neural tissue (average value)	0.2	Buston et al [51, 52]
encapsulation layer (0.5mm thick)	0.1	Buston et al [51, 52]
encapsulation layer (0 – 1mm thick)	0.05 – 0.2	Grill and Mortimer [52]
White matter	0.15	Geddes and Baker, Malmivuo and Plonsey [52]
Grey matter	0.45	Geddes and Baker, Malmivuo and Plonsey [52]
Mean conductivity	0.17	Geddes and Baker, Malmivuo and Plonsey [52]
Average head conductivity	0.33	Geddes and Baker [53, 54]
Grey matter	0.1	Gabriel [42], Nicholson [55], Apollonio [56]

4.2.3 Biological Tissue Parameters Database

Based on large experimental studies and data published by Gabriel and his group, experimental database for the dielectric properties of biological tissue was collected and established in 1996 from excised animal tissue at 37°C.

The values for relative permittivity, conductivity and loss tangents for White and Grey human brain tissue extracted from the Gabriel model [42-44, 57-58] are shown in Figure 4-1, Figure 4-2, Figure 4-3 and Figure 4-4.

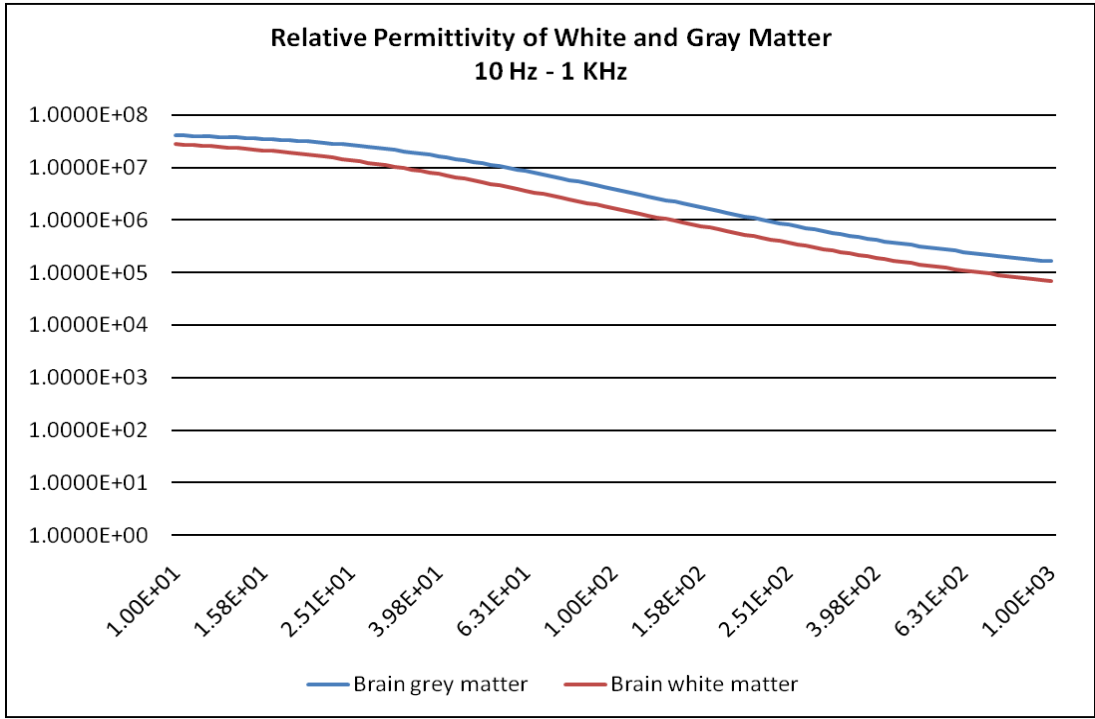


Figure 4-1 Semi-log plot of the relative permittivity of White and Grey matter 10 Hz – 1 KHz

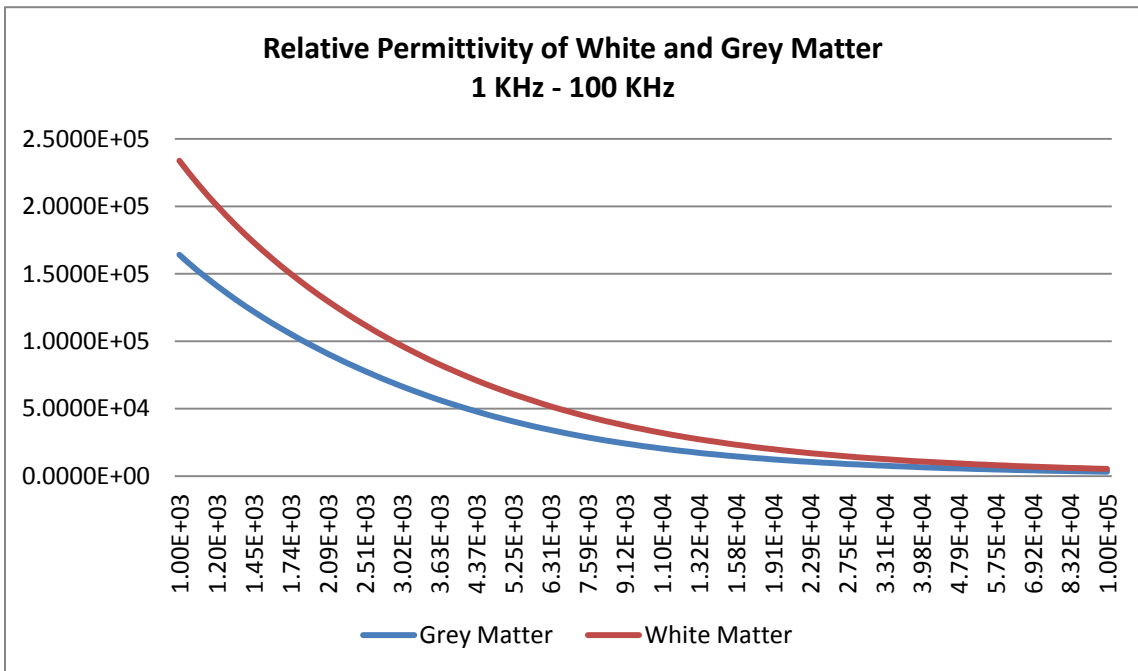


Figure 4-2 Semi-log plot of the relative permittivity of White and Grey matter 1 KHz – 100KHz

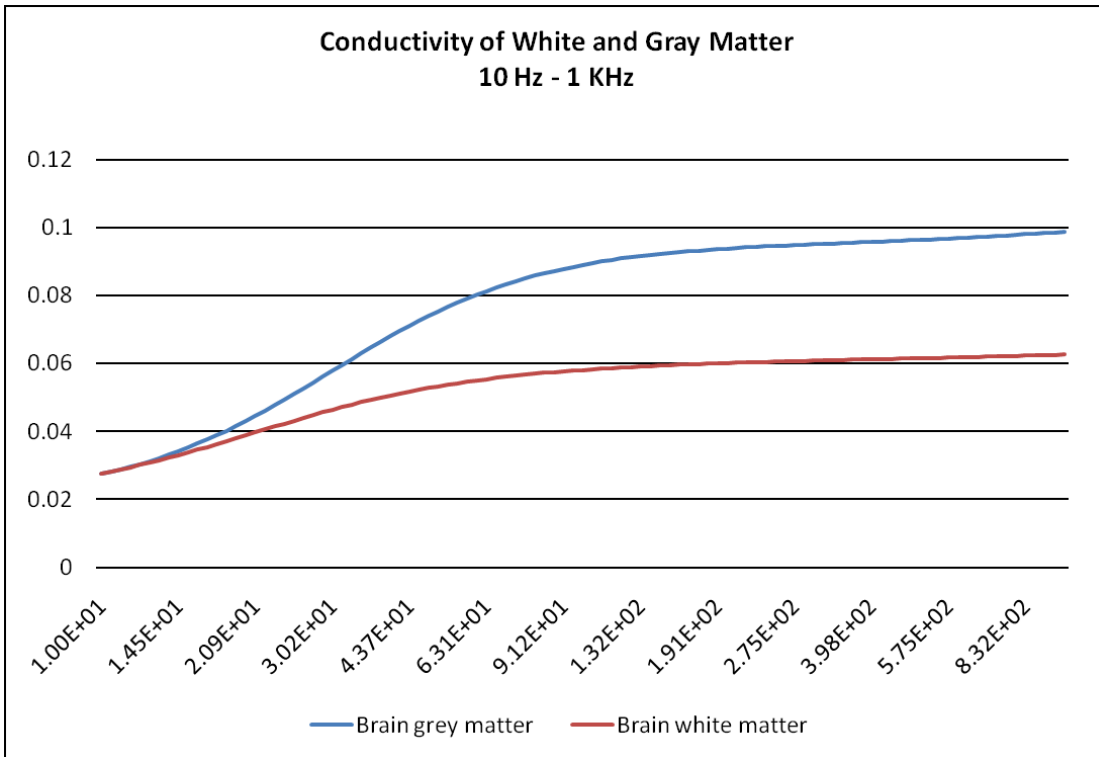


Figure 4-3 Conductivity of White and Grey matter 10 Hz – KHz

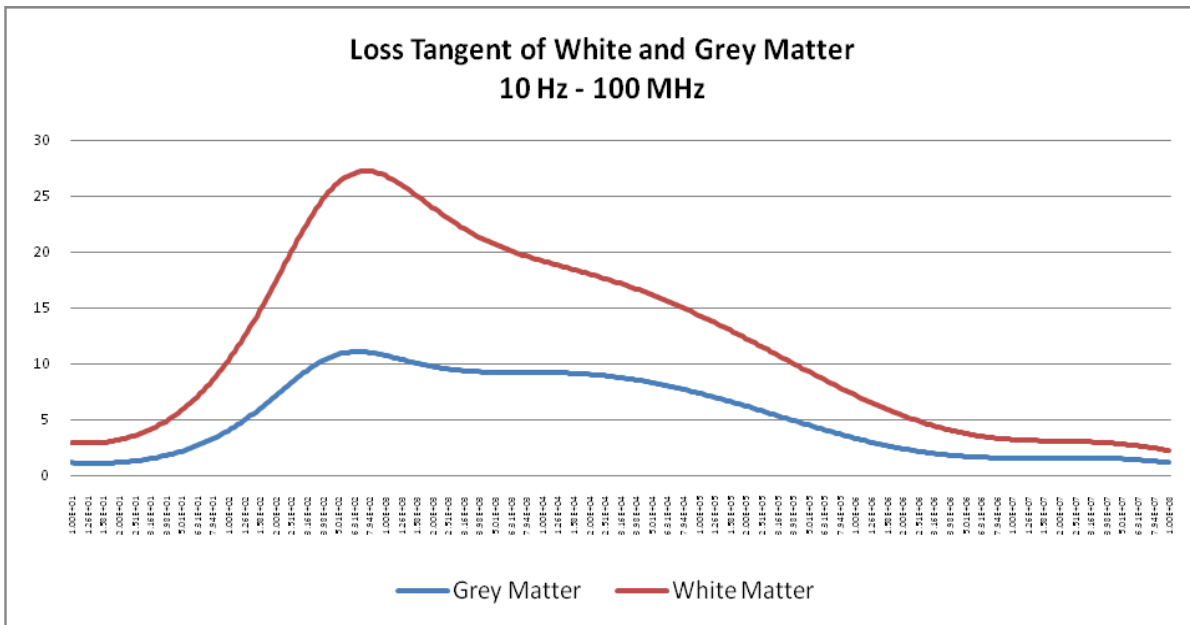


Figure 4-4 Loss Tangent of White and Grey matter 10 Hz – 100 MHz

4.2.4 Discussion

The effect of the Grey and the White brain tissue layers were discussed for different dielectric properties (permittivity and conductivity). The dielectric properties of the biological tissue are frequency dependant, they also vary widely between different species (rodents, primates and humans) according to the tissue composition. As frequency decreases, tissue conductivity drops, on the other hand, its dielectric permittivity constant increases considerably along the spectrum [44, 57]. The values for the dielectric properties of the brain tissue are extracted from the parametric database of the biological tissue which was developed based on Gabriel model.

Dielectric properties of biological tissue is a function of frequency exhibiting remarkable leaps in value as the frequency approaches low and near DC values (<1MHz). The accuracy of the models relies on the abundance of experimental data which is elaborately detailed for high frequencies motivated by wireless and mobile communication industry. On the other hand, available low frequency data is not enough to provide accurate models. Moreover some of the available data is distorted by electrode polarization errors as well as errors inherent in low frequency in vitro measurements. These factors limit the truthfulness of low frequency data available in the 1996 database and commercial simulators. In summary, low frequency simulation results are to be considered as an estimate and further accurate experimental measurements would be of much value to the biological tissue database.

4.3 Finite Difference Time Domain (FDTD)

FDTD is a time domain computational electrodynamics modeling technique developed for solving time-dependent Maxwell's equations after discretizing the model using central-difference approximations to the space and time partial derivatives. This yields a set of finite-difference equations which are solved in a leapfrog manner to evaluate the electric field vector components in a volume of space at a given instant in time followed by solving for the magnetic field vector components in the same spatial volume at the next instant in time. This time stepping technique makes FDTD more privilege than FEM which requires solving a system of equations at each time step and requires multiple runs to achieve similar temporal detail. Also in FDTD, there is no matrix to be stored during the solution, which reduces memory requirements.

Simulations were executed using Empire XCcel 5.2 (IMST GmbH, Kamp-Lintfort Germany) [59]. EMPIRE XCcel is a 3-D electromagnetic field simulator which employs the Finite Difference Time Domain (FDTD) method for modeling and solving electromagnetic problems. This algorithm together with the embedded human body models makes it a suitable tool for modeling and simulating implanted DBS electrodes capable of providing accurate results using readily available computational resources (desktop PCs). FDTD also is able to solve electromagnetic problems ranging from near DC (quasistatic) models to all the way through microwaves.

4.4 Brain Modeling

As was discussed before, three different situations (Model I-III) of the implanted electrode inside brain tissue was modeled. In the next section the steps to build these models as well as the biological parameters for each of these models are introduced.

4.4.1 Modeling a DBS Electrode Inside Homogeneous Brain Tissue (Model-I)

The first model (Model-I) is a simple representation of brain Grey tissue as a homogenous lossy dielectric with isotropic and frequency independent characteristics. This model disregards anatomical details of the brain [7, 51]. Figure 4-5 illustrates a schematic diagram of the Medtronic 3387 deep brain stimulation electrode at the right section of the figure. The electrode is made of a cylindrical polyurethane polymer core ($\varnothing = 1.28$ mm) with four platinum contact rings on its perimeter for charge delivery. The rings have a thickness of 80 μm and 1.5 mm in height with a spacing of 0.5 mm. FDTD has a limited ability to mesh non-cartesian grids [60], and in order to model the circular features of the electrode while maintaining high accuracy, the perfect geometric approximation (PGA) algorithm [59] was used. The PGA algorithm can map the circular features to a Cartesian grid by adjusting the FDTD coefficients to minimize the staircasing effects as shown in Figure 4-6.

In addition, the electrode was located at the center of a cubic Model-I with its length equal to 15.0 mm. This Model-I is comprised of isotropic homogeneous brain tissue from Grey matter of the subthalamic nucleus (STN) located in the basal ganglia where the electrode is usually inserted. An x-y cross section of this model is shown in the left section of Figure 4-5.

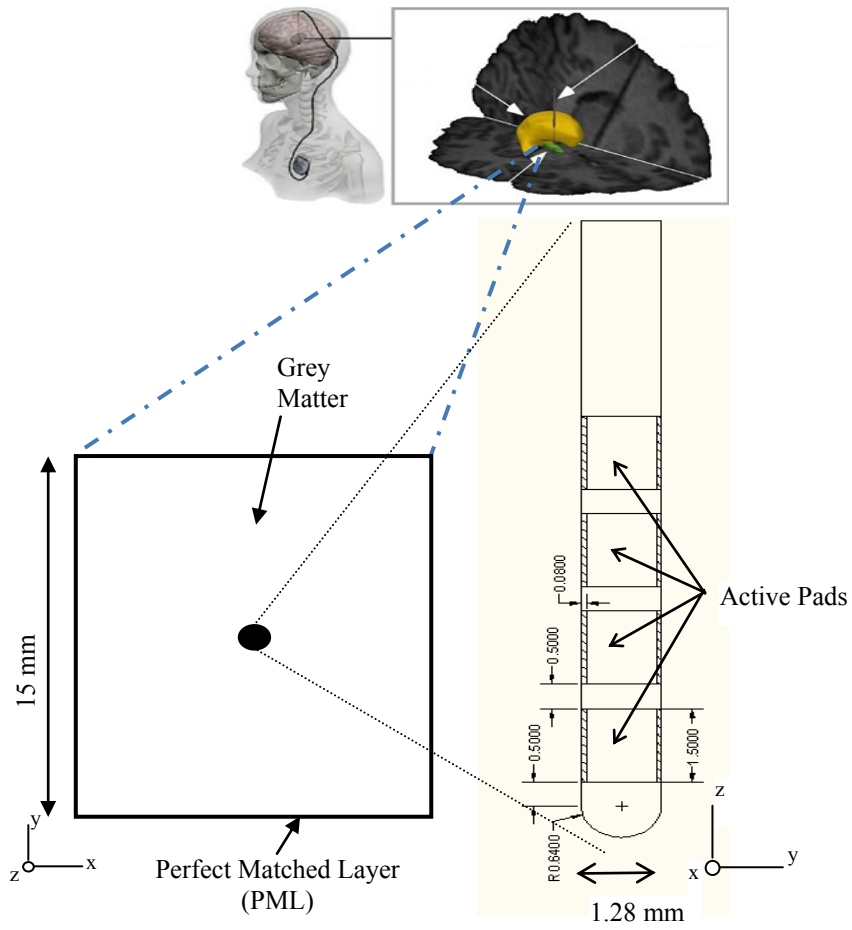


Figure 4-5 Schematic diagram of the proposed Model-I

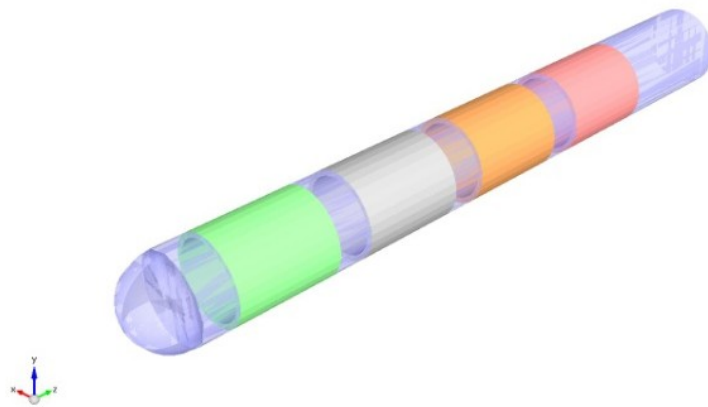


Figure 4-6 FDTD Medtronic 3387 DBS electrode

Since FDTD problems involve open regions and of course it is not practical to discretize an infinite region, instead, cubic boundaries have been used to terminate the computational region; these boundary conditions serve to absorb outgoing waves, and are called absorbing boundary conditions (ABC). A popular set of absorbing boundary conditions is the perfectly matched layer (PML) invented by [73]. The PML is a layer of artificial material surrounding the computational region and designed to damp waves propagating in the normal direction as shown in Figure 4-5.

Since the stimulus waveform is a train of square voltage pulses with a main frequency between 100-150 Hz. To account for all frequency dependence of brain tissue; permittivity, conductivity and the constant loss tangent of the brain medium for a Grey and White matter are extracted at 130 Hz (median frequency) from the Figure 4-1, Figure 4-2, Figure 4-3 and Figure 4-4.

The DBS electrode usually resides in the internal globus pallidus (GPi) or subthalamic nucleus (STN) located in the basal ganglia; these tissues are composed of Grey matter which at 130 Hz has a dielectric constant $\epsilon_r = 2.46 \times 10^6$, conductivity $\sigma = 0.097 \text{ S.m}^{-1}$, and a constant loss tangent equal to 5.20 [58]. The outer layer is made of White matter with a dielectric constant $\epsilon_r = 1.06904 \times 10^6$, conductivity $\sigma = 0.059 \text{ S.m}^{-1}$ and a constant loss tangent equal to 7.71 at 130 Hz [58] as shown in Table 4-2.

Table 4-2 Tissue conductivities, σ , relative permittivity, ϵ_r , and loss tangent calculated at a median frequency of 130 Hz for the Grey and White tissue matter.

Layer	σ (s/m)	ϵ_r	Loss Tangent
Grey Matter	0.097	2.46×10^6	5.20
White Matter	0.059	1.06904×10^6	7.71

4.4.2 Foreign Body Response and Encapsulation Formation (Model-II)

Neuro compatibility represents the quality of the electrode-tissue interface. Because these electrodes are intended for prolonged application, tissue active response has to be considered due to the tendency of proteins and cells to adhere to foreign bodies inserted in the human body. Proteins adhere to the electrode being a foreign body which encourages further skin adhesion forming an organic layer. This layer encapsulates the electrode by an inexcitable tissue layer

increasing the contact impedance and degrading functionality. The capsule thickness depends on the degree of reactivity of the tissue to the implanted object as well its shape and surface condition.

Inserting an electrode in a body provokes a Foreign Body Reaction (FBR) [63-66] and this inflammatory reaction attempts to get rid of the foreign body by an encapsulation effect. The capsule can be fully formed within 15 days to four months [67] depending on the provocativeness of the electrode material [68] and the thickness of the capsule depends on the electrode biocompatibility which is a function of electrode material and geometry [69].

During a period of 2–12 weeks, a continuous sheath of cells grows (in a loosely organized pattern within 2 weeks and develops a highly compacted and continuous layer in 6 to 12 weeks) and is capable of electrically isolating the electrode. During the development process of the layer, the sheath is more strongly attached to the surface of the electrode than surrounding tissue [70]. Metals that invoke high tissue response exhibited formation of thick capsules after 15 days [67]. Also, the electrode geometry and size control the formation of capsules; for example, micro-sized implants invoke thin capsule [69].

The conductivity of the encapsulation layer has a minimum value of $0.05 \text{ S} \cdot \text{m}^{-1}$ ranging between $0.05 - 0.2 \text{ S} \cdot \text{m}^{-1}$ [55, 61]. The second Model-II (Figure 4-7) includes the encapsulation tissue layer which has a similar permittivity value as Grey tissue and a lower conductivity of $0.05 \text{ S} \cdot \text{m}^{-1}$. The encapsulation layer thickness varies between 0.1 to 1 mm [52] and is influenced by the electrode material biocompatibility and the inserting duration.

4.4.3 DBS Electrode Position with Respect to Two Different Brain Tissues (Model-III)

Model-III has two layers representing the Grey and White tissue as shown in Figure 4-8. Several models were proposed in [51, 72] assuming a homogeneous tissue structure and including a fixed thickness encapsulation of 0.5 mm. In order to investigate the effects of non homogeneity on the field distribution, model-III with nonhomogeneous layers and a variable thickness of Grey matter layer was used. The results exhibited effects on the electric field distribution which accordingly controls the spatial penetration of the electric field.

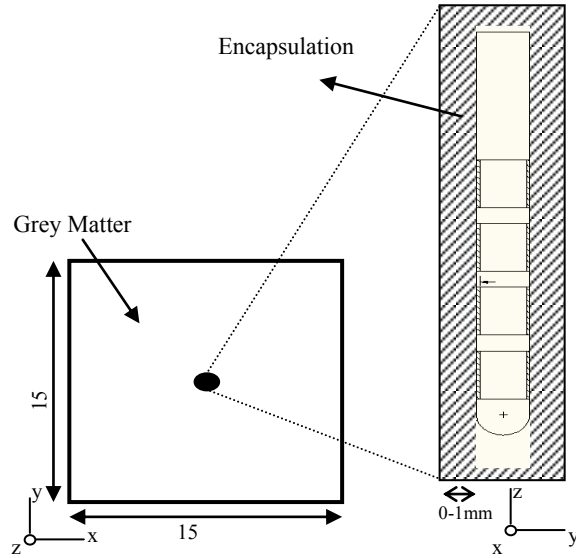


Figure 4-7 A schematic diagram of the proposed Model-II representing the electrode surrounded with an encapsulation layer inside the Grey tissue.

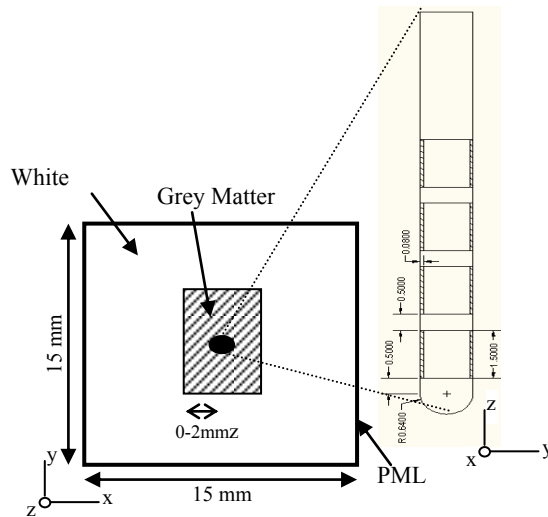


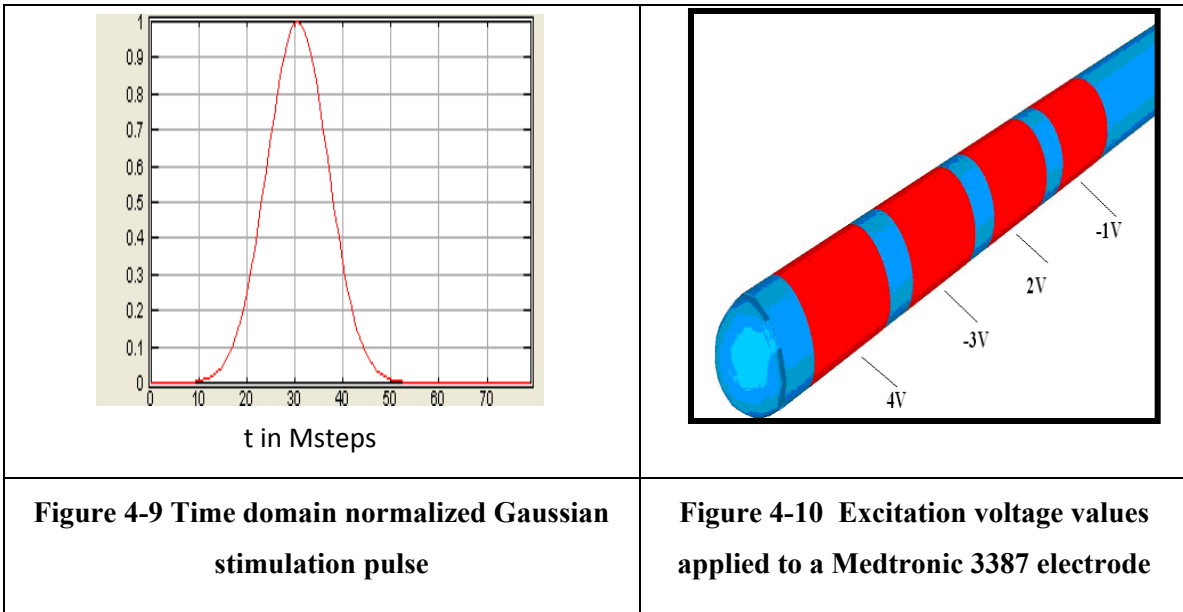
Figure 4-8 A schematic diagram of the proposed Model-III representing the electrode surrounded with Grey tissue and inserted in White matter

4.5 Simulation Setup

In the previous section we have introduced the three models (Models I-III) that represented the implanted DBS electrode inside the brain tissue, and in order to study their influence on the electric field distribution we need to apply DBS stimulation pulse parameters (Amplitude and

width). In this section we discuss these parameters as well as the discretization and model stability.

The deep brain stimulation pattern is a sequence of monophasic square pulses with pulse duration of $0.1\mu\text{s}$ and a frequency of 130 Hz (median) and maximum amplitude ranging from 1 – 4 volts and can reach 10 volts [37, 51, 71]. In the FDTD analysis, the monophasic pattern is replaced with a Gaussian pulse (Figure 4-9) which is more appropriate for time domain analysis. When a Gaussian pulse is used, the electric field intensity is underestimated by 0.27 – 2.7% [74, 75]. Figure 4-10 presents the developed and simulated Medtronic 3387 electrode’s information using the Empire package and different excitation voltages at its different cylindrical rings. Each ring is excited with the voltage values shown in Figure 4-10.



4.5.1 Discretization and Model Stability

Mesh resolution has a significant effect on simulation results and the Raytrace meshing algorithm was used to maintain second order accuracy of the FDTD scheme [60]. Manipulating the grid line spacing optimizes memory consumption and this fulfills the following conditions: First, the smallest cell size determines the time step for the simulation; very small cells will create long simulation runs. The space has to be resolved such that the smallest wavelength is sampled properly: $\delta x < (\lambda/10)$, where δx is the smallest cell dimension and λ is the wavelength of the input signal (stimulation pulse). Second, if the field values are changing rapidly in a

region, the resolution of the space should be chosen in a way that the desired accuracy is obtained. The automatic discretization algorithm was configured to control the meshing density and resolution. Meshing is disabled for all contact rings to save memory. On average, a total of 1.844 Mcells were used for meshing the model. Finally, to create a finite computational domain, a level 6 perfect matched layer (PML6) was used as an absorbing artificial boundary condition. A simulation pulse was tuned to test its effect on model accuracy and stability. The optimal simulation pulse configuration was automatically set by the simulator. Lower oversampling values degrade the smoothness of the input voltage waveform as shown in Figure 4-11a, increasing the oversampling value to 3 improves the waveform shape (Figure 4-11b) and further increase in its value has no apparent effect (Figure 4-11c, d).

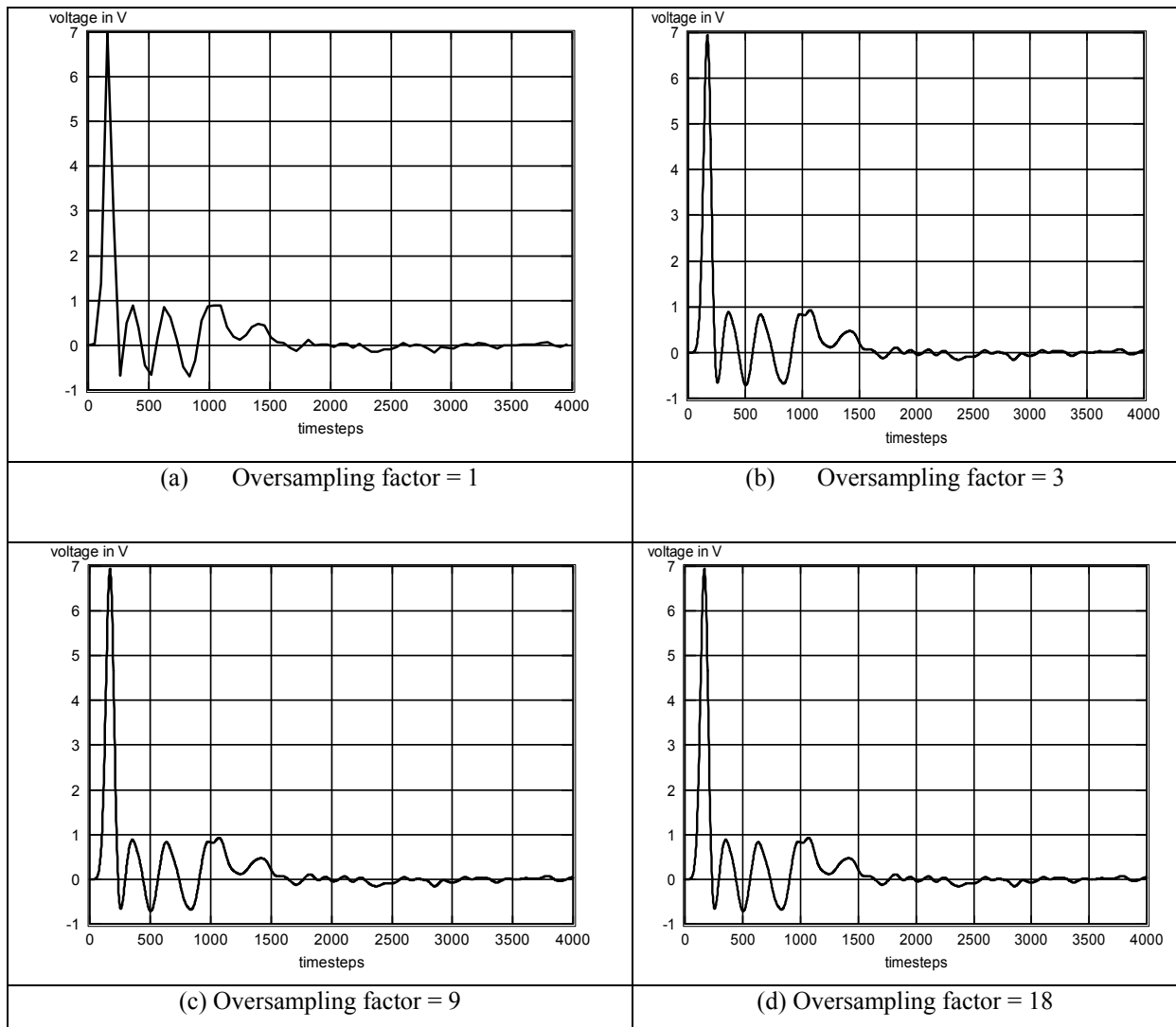


Figure 4-11 Effect of oversampling on the input simulation pulse

A number of input voltage pulses are plotted for oversampling values of 1, 3, 9 and 18; where 9 is the optimal value set by the simulator. The number of stimulation steps and the bandwidth must be large enough for sweeping the input voltage pulse waveform; otherwise simulation will terminate prior to completion of the input pulse which can yield non-converging incomplete results. Expanding the value of the simulation bandwidth consumes more memory and requires more processing time.

4.6 Simulation Results

Several parameters of deep brain stimulation were controlled to study their influence on the electric field distribution within the brain tissue and the associated volume of tissue activated. These parameters include: tissue dielectric properties (permittivity and conductivity), non-homogenous tissue structure, encapsulation tissue thickness, stimulation pulse characteristics (width and amplitude) and finally the firing pattern (current steering). The output of the simulations is the maximum electric field intensity distribution within the brain tissue represented by equipotential contours. This output can be used to estimate the (VTA) according to the depth of the electric field penetration into the brain tissue as shown in Figure 4-12.

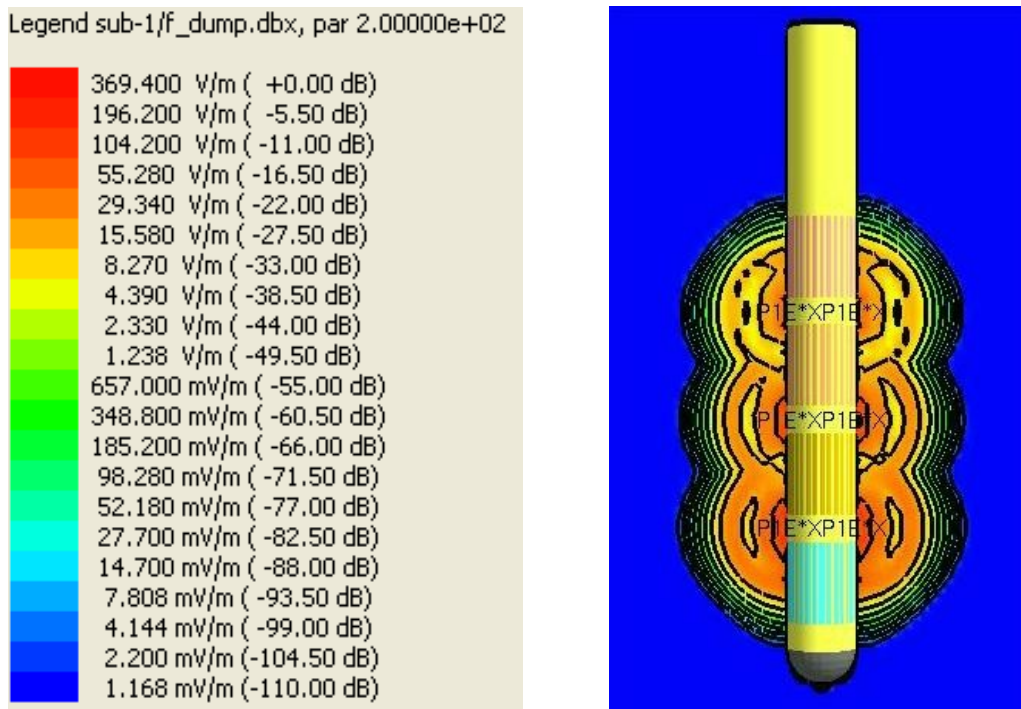


Figure 4-12 Electric field distribution for Gaussian pulse, $\epsilon_r = 1 \times 10^5$, $\sigma = 0.1 \text{ S} \cdot \text{m}^{-1}$

Starting with Model-I which is a homogenous and isotropic representation of the Grey tissue; the tissue exhibits a significant increase in dielectric permittivity and a drop in the conductivity values near DC (10 – 1000 Hz) demonstrating the characteristics of a poor conductor. This leads to lowering the associated field intensity and accordingly the electric field penetration will drop. The electric field intensity due to different dielectric properties values are plotted in Figure 4-13 and the results show that the elevated permittivity values have a dominant influence on the field distribution. On the other hand, a variation in tissue conductivity has a negligible effect, the maximum field values are listed in Table 4-3. The electric field penetration depth values for different relative permittivity values are listed in Table 4-4. The field penetration depth reaches 1.5 mm at a relative permittivity of 10^5 which drops to 1 mm at $\epsilon_r = 10^6$, and increases to 6 mm when the relative permittivity drops to 10^4 .

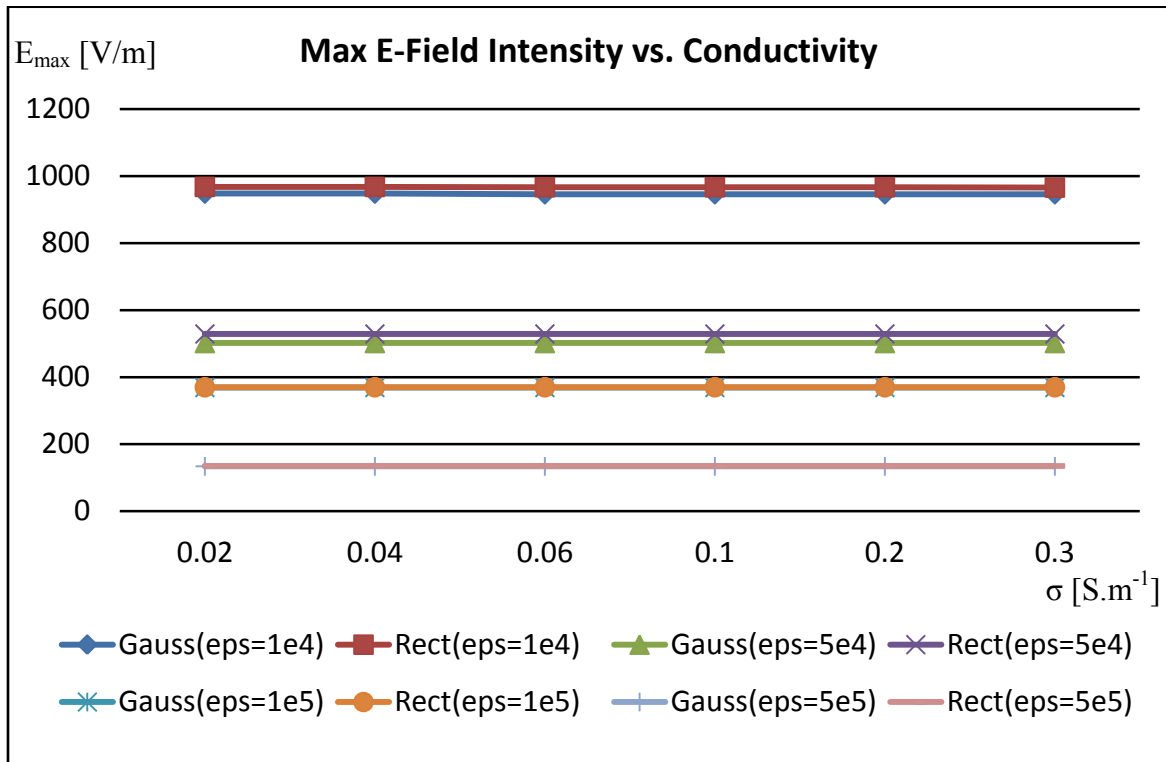


Figure 4-13 Maximum electric field values for different permittivities estimated for several conductivities.

Table 4-3 Maximum electric field intensities [V/m] for different tissue dielectric properties

Stimulation Pulse and Permittivity	Conductivity					
	0.02	0.04	0.06	0.1	0.2	0.3
Gauss, $\epsilon_r = 10^4$	948	948	946	946	946	946
Monophasic, $\epsilon_r = 104$	968	968	967	967	967	966
Gauss, $\epsilon_r = 5 \times 10^4$	502	502	502	502	502	502
Monophasic, $\epsilon_r = 5 \times 10^4$	529	529	529	529	529	529
Gauss, $\epsilon_r = 10^5$	369	369	369	369	369	369
Monophasic, $\epsilon_r = 10^5$	370	370	370	370	370	370
Gauss, $\epsilon_r = 5 \times 10^5$	134	134	134	134	134	134
Monophasic, $\epsilon_r = 5 \times 10^5$	135	135	135	135	135	135

Table 4-4 Electric field penetration depth activated vs. tissue permittivity values

Permittivity	Electric field penetration depth
1×10^4	6.0 mm
1×10^5	1.5 mm
1×10^6	1.0 mm

The effect of tissue dielectric constant on the field intensity distribution for $\epsilon_r = 10^4$ up to 10^6 is modeled. Matlab Linear regression with the power series equation provided the most accurate model with a minimum root mean square error (RMSE) and maximum coefficient of determination R^2 , with confidence bounds of 95% Figure 4-14. The extracted equation is:

$$E_{\max}(\epsilon_r) = (4.499 \times 10^4) \cdot (\epsilon_r)^{-0.4157} \text{ [V/m]} \dots (4.2)$$

where $R^2 = 94\%$, and $RMSE = 64.56$,

Equation (4.2) represents the relation between the maximum electric field intensity and tissue relative permittivity values. The results in Figure 4-13 exhibit the negligible influence of the conductivity on the field distribution.

The coefficient of determination R^2 measures the goodness of the estimated regression equation. The higher the r -squared, the more confidence one can have in the equation. It also provides a measure of how well future outcomes are likely to be predicted by this equation. r -squared has the range of values between 0 and 1 in this analysis.

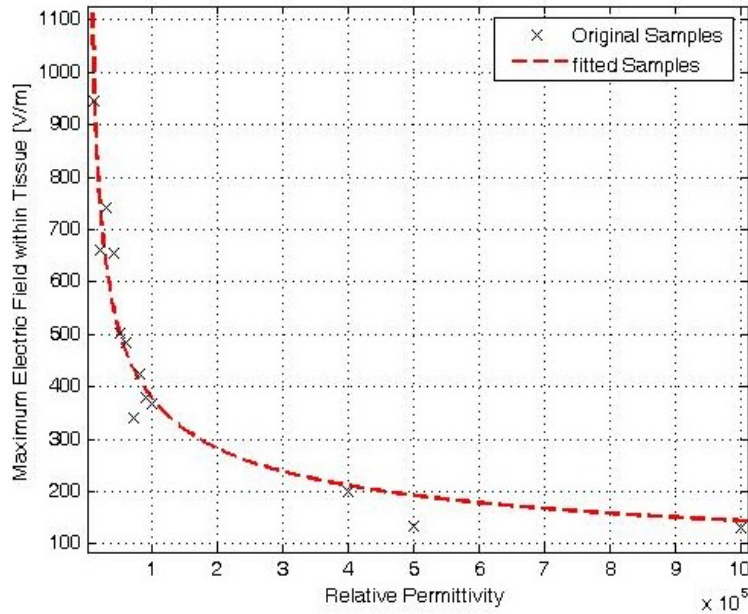


Figure 4-14 Electric field intensity vs. permittivity @ $\sigma = 0.1 \text{ S.m}^{-1}$

Since from Model-I we conclude that the variation in tissue conductivity has a negligible effect on the maximum field values and even its distribution, i.e. the relative permittivity value is the only parameter that controls the distribution of the electric field inside the brain. Due to computational time and capability, we can scale down the relative permittivity values by a factor of 2.5 (the same factor between the Grey and White tissue matter calculated at 130Hz), thus in model-II and model-III we have chosen the relative permittivity value of the Grey tissue matter equal to 1×10^5 and hence the White tissue matter will be 4×10^4 . These factors were the largest values suitable to our processing time.

Model-II (Figure 4-15) shows the encapsulation tissue layer and its thickness. This thickness is varied from 0.1 mm to 1 mm with 0.1 mm increments to investigate its effect on the field distribution. The results are plotted in Figure 4-16 showing that the field intensity is inversely proportional to the capsule thickness. In order to compensate for the field attenuation

due to the formation of the capsule, the stimulation pulse has to be altered to maintain the targeted depth of the electric field. The results were modeled to demonstrate the effect of capsule thickness (T_{Capsule}) on the field distribution:

$$E_{\text{max}}(T_{\text{Capsule}}) = 47.6(T_{\text{Capsule}})^{-1.01} + 401 \text{ [V/m]} \dots (4.3)$$

where $R^2 = 91\%$, and $RMSE = 47.1$

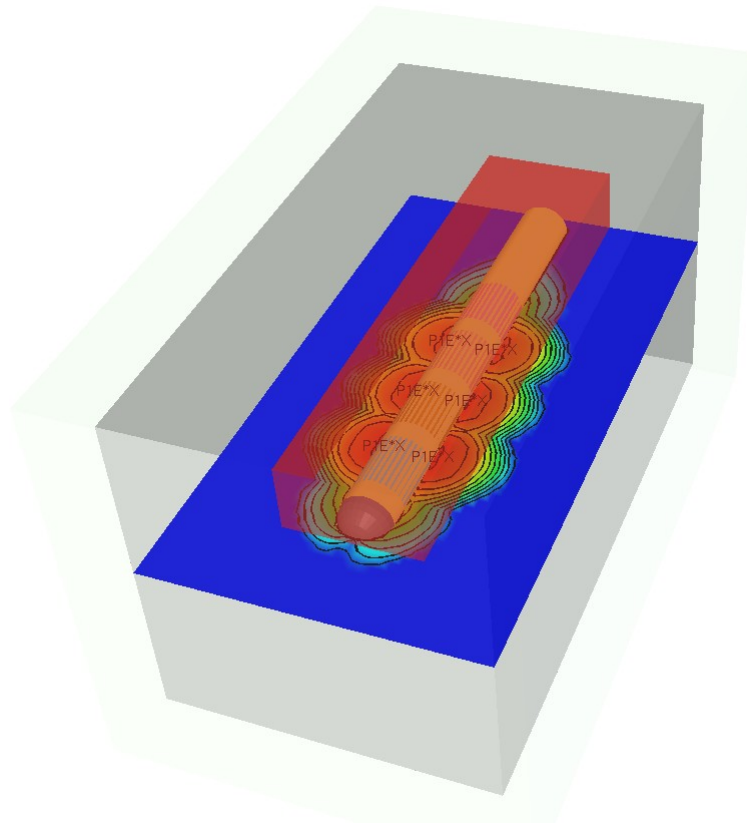


Figure 4-15 Model-II: Homogenous model with encapsulation layer; $\epsilon_r = 1 \times 10^5$, gray box (Grey tissue): $\sigma_{\text{Gray tissue}} = 0.1 \text{ S. m}^{-1}$, red box (encapsulation layer): $\sigma_{\text{capsule}} = 0.05 \text{ S. m}^{-1}$

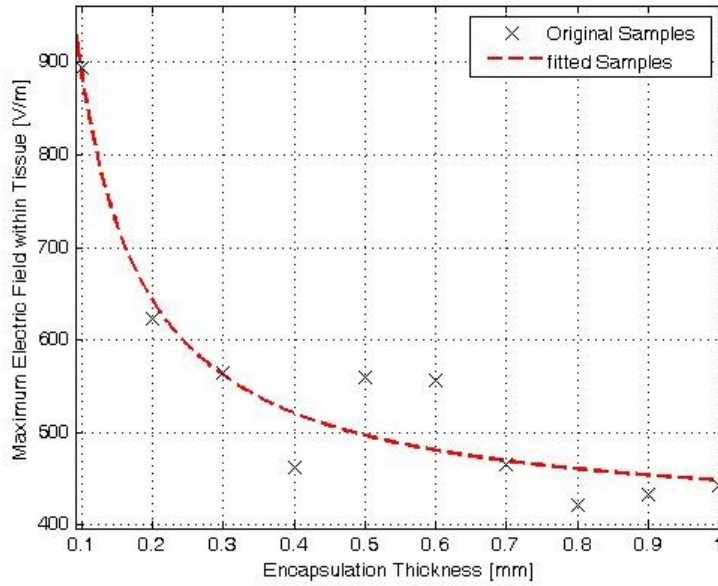


Figure 4-16 Maximum electric field intensity vs. capsule thickness (T_{Capsule}) for tissue permittivity of ; $\epsilon_r = 1 \times 10^5$ and $\sigma_{\text{Gray tissue}} = 0.1 \text{ S. m}^{-1}$, $\sigma_{\text{Capsule}} = 0.05 \text{ S. m}^{-1}$

To simulate the change of the electrode proximity to the Grey-White tissue boundary. Model-III represents the electrode position within the tissue boundary by changing the Grey tissue layer thickness (T_{Grey}) from 0 – 2 mm. The results in Figure 4-17 exhibit a pinch in the field lines at the Grey-White matter boundary associated with more dense distribution of the field equipotential lines. As a result; the penetration of the electric field within the Grey matter decreases. The effect of Grey tissue thickness (T_{Grey}) on the field intensity is plotted in Figure 4-18 and expressed by equation 4.4.

$$E_{\text{max}}(T_{\text{Grey}}) = 200.3(T_{\text{Grey}})^{-0.452} + 139.2 \dots (4.4)$$

$R^2 = 98.5\%$, and $RMSE = 34.6$

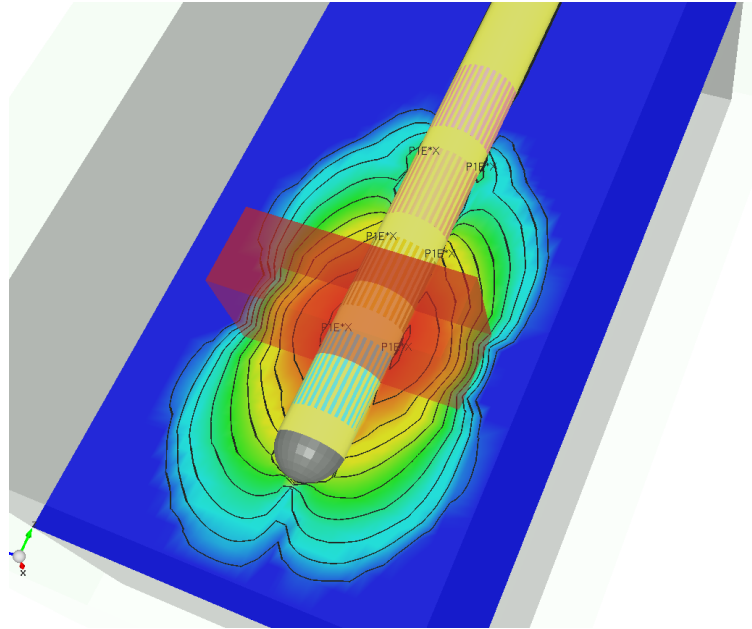


Figure 4-17 Model-III: Non-homogeneous model for Grey and White tissue layers, red box (Grey tissue): $\epsilon_{r\text{-Grey tissue}} = 1 \times 10^5$, $\sigma_{\text{Grey tissue}} = 0.1 \text{ S} \cdot \text{m}^{-1}$, gray box (White tissue): $\epsilon_{r\text{-White tissue}} = 4 \times 10^4$, $\sigma_{\text{White tissue}} = 0.06 \text{ S} \cdot \text{m}^{-1}$

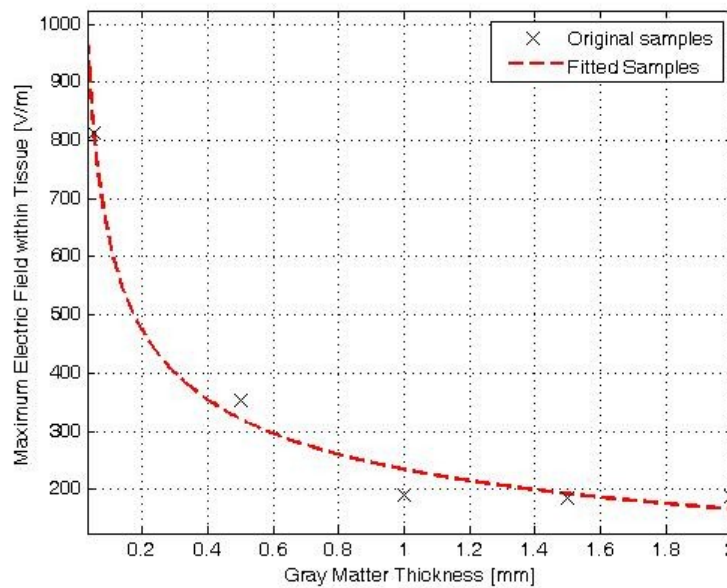


Figure 4-18 Maximum electric field intensity vs. Grey matter thickness (T_{Gray}) for $\epsilon_{r\text{-Grey tissue}} = 1 \times 10^5$, $\sigma_{\text{Grey tissue}} = 0.1 \text{ S} \cdot \text{m}^{-1}$ and $\epsilon_{r\text{-White tissue}} = 4 \times 10^4$, $\sigma_{\text{White tissue}} = 0.06 \text{ S} \cdot \text{m}^{-1}$

4.7 Stimulation Pulse

The stimulation pulse has two degrees of freedom (amplitude and width) that are manipulated to study the effect of the pulse characteristics on the field distribution. In this study, a single layer homogenous (Model-I) was used and the simulation was iterated for two different values of relative permittivity (10^4 and 10^5) and conductivity $\sigma = 0.1 \text{ S.m}^{-1}$ as shown in Figure 4-19. Sweeping the pulse amplitude (A) from 1 to 10 volts had no effect on the depth of field penetration within the tissue while it directly controlled the levels of field intensity. The results were modeled by linear relation characteristics which provided the most accurate model with a minimum $RMSE = 18.2$ and 5.88 for $\epsilon_r = 10^4$ and $\epsilon_r = 10^5$ respectively, and maximum coefficient of determination $R^2 = 99.8\%$ as shown in Figure 4-20. The extracted equations are:

$$\epsilon_r = 10^4: E_{\max}(A) = 162.* A \text{ [V/m]} \dots (4.5)$$

$$\epsilon_r = 10^5: E_{\max}(A) = 53.0 * A \text{ [V/m]} \dots (4.6)$$

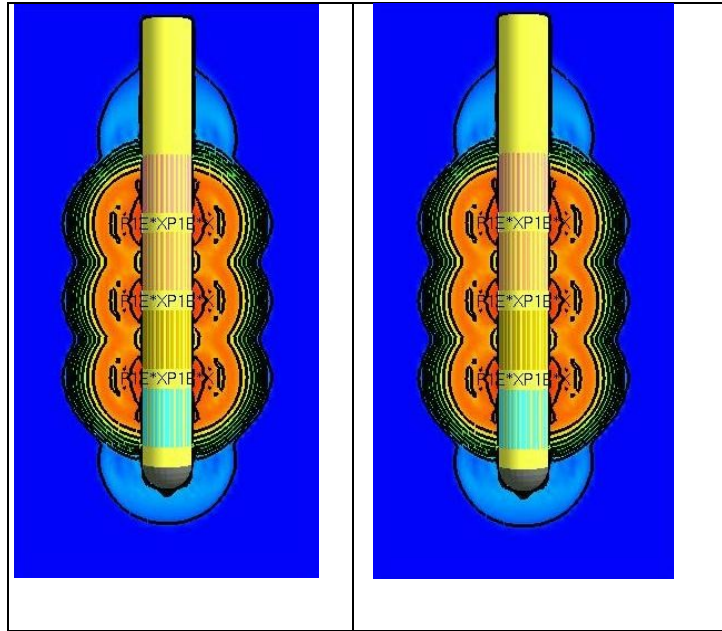


Figure 4-19 Effect of pulse amplitude on field distribution, (left: 1 V, right: 10 V) @ $\epsilon_r = 10^5$, $\sigma = 0.1 \text{ S.m}^{-1}$

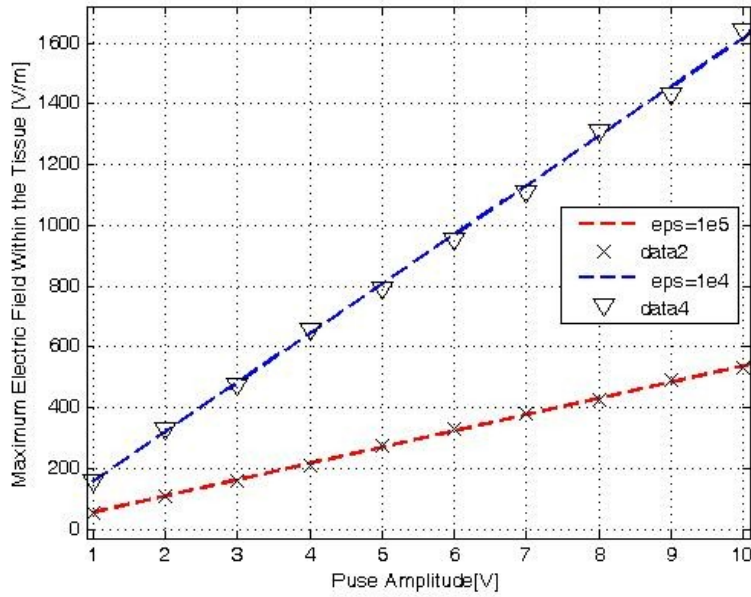


Figure 4-20 Electric field intensity vs. simulation pulse amplitude (A) for $\epsilon_r = 10^4$ and 10^5 @ $\sigma = 0.1 \text{ S. m}^{-1}$

The results in Figure 4-19 and Figure 4-20 show the dominance of the pulse amplitude on the field intensity at lower tissue permittivity, where the slope at $\epsilon_r = 1 \times 10^4$ is almost 3 times that of $\epsilon_r = 1 \times 10^5$.

To study the effect of pulse width on the electric field distribution, a constant amplitude pulse of 5 volts and width (PW) varying from 52 to 52000 steps (time step is set to 0.5 psec due to computational limitations) was defined for the stimulation pattern using Model-I with $\epsilon_r = 1 \times 10^5$ and $\sigma = 0.1 \text{ S. m}^{-1}$ (Figure 4-21). A semi-log presentation of the maximum electric field versus pulse width is shown in Figure 4-22. These results infer that the electric field spatial depth is mainly controlled by changing the simulation pulse width rather than its amplitude. Therefore the amplitude of the stimulation current injected can be reduced by increasing the pulse width, to obtain the same effect on the spatial distribution of the electric field. The results were represented by power relation characteristics with $RMSE = 131$ and $R^2 = 98\%$, the model equation is:

$$E_{\max}(W) = 21.6(\text{pulse width})^{0.4} \text{ [V/m]} \dots (4.7)$$

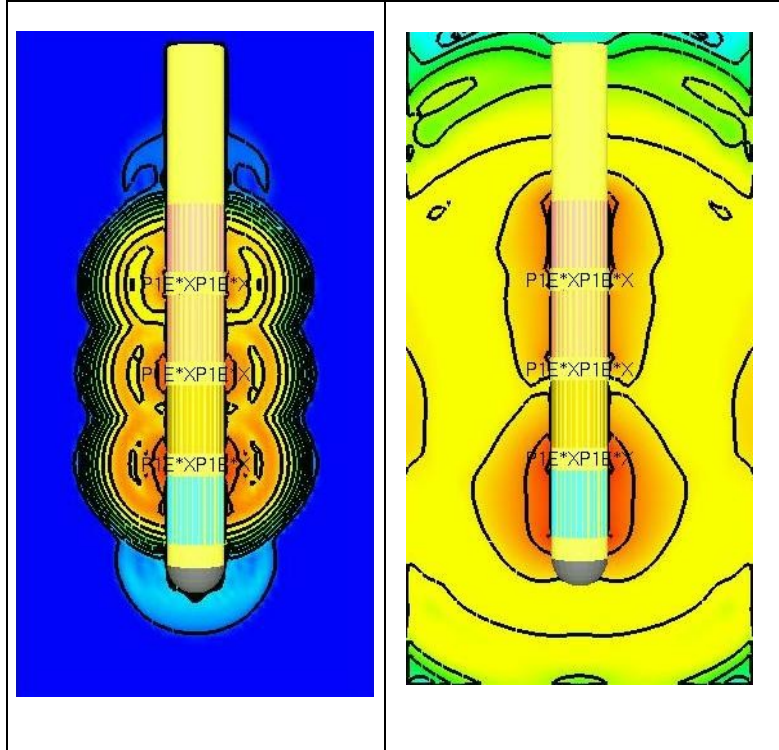


Figure 4-21 Effect of pulse width on field distribution (52 and 52000 steps) @ $\epsilon_r = 10^5$, $\sigma = 0.1 \text{ S.m}^{-1}$

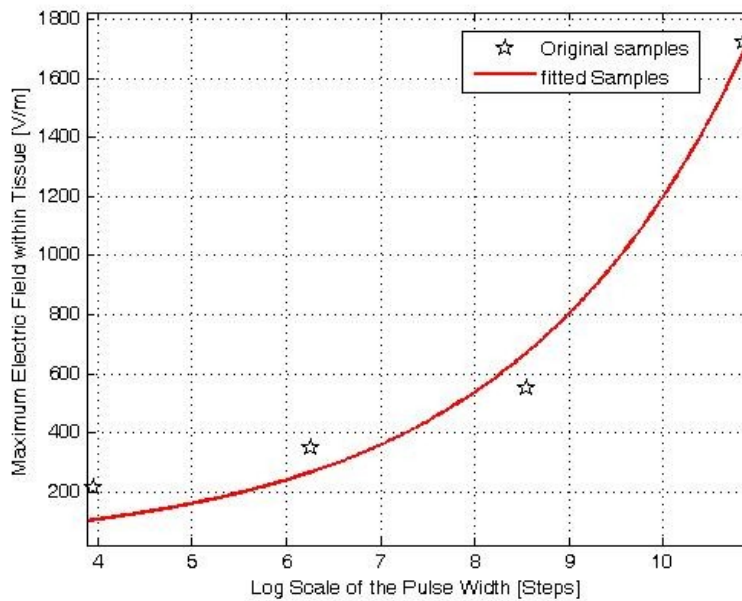


Figure 4-22 Electric field intensity vs. simulation pulse width @ $\sigma = 0.1 \text{ S.m}^{-1}$, $\epsilon_r = 10^5$

4.8 Firing Pattern Stimulation

In order to improve the effectiveness of DBS it is required to enhance the spatial precision of charge delivery and to minimize the risk of undesired stimulation of non-targeted regions. Current steering mechanisms can be employed to control the spatial distribution of the created electric field by sculpturing it within the brain tissue. Several parameters can be manipulated to achieve current steering and electric field shaping; these include contact shapes and distribution, stimulation pulse waveform and tissue dielectric properties.

To investigate the influence of current steering on sculpturing the electric field, a variable firing pattern was applied as differential currents between the contact rings using 2 and 3 rings. A constant current source model was used for stimulation, and the weights of the differential currents applied between the rings were controlled to yield different ratios. A single layer homogenous model is used ($\epsilon_r = 1 \times 10^5$, $\sigma = 0.1 \text{ S. m}^{-1}$).

The electric field distribution for different firing patterns is shown in Figure 4-23 which shows the flexibility in shaping the electric field distribution and controlling it as the number of firing rings increases. As an example of the effect of current steering on field distribution: single ring firing yields electric spatial distribution represented in Figure 4-23a; this distribution is doubled by applying half the stimulation current level while simultaneously firing from two rings as shown in Figure 4-23d. It is obvious that it is possible to shape the electric field distribution within the brain tissue by changing the stimulation pattern as well as the pads distributions. Figure 4-24 shows the maximum electric field versus current steering ratio for different permittivity $\epsilon_r = 1 \times 10^4$ and $\epsilon_r = 1 \times 10^5$ at $\sigma = 0.1 \text{ S. m}^{-1}$.

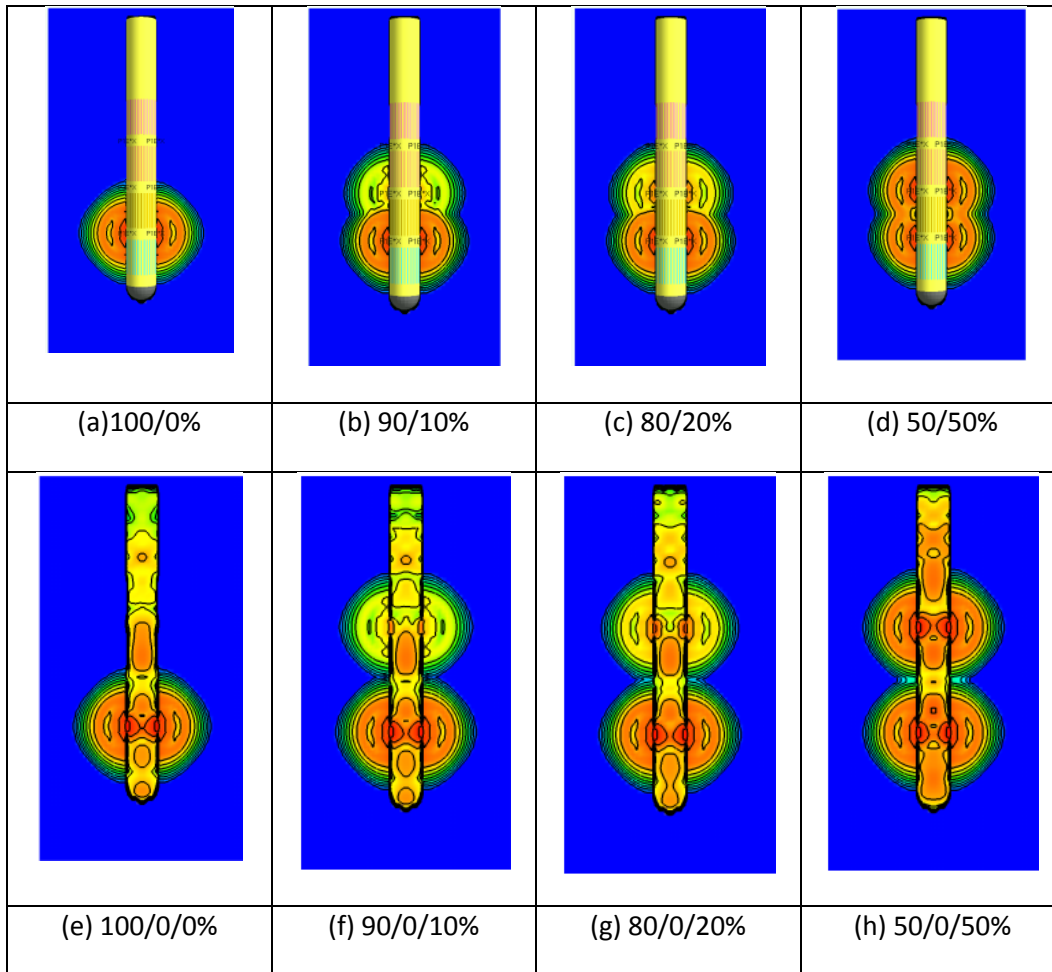


Figure 4-23 Current steering and field shaping, top: 2 rings firing, bottom: 3 rings firing

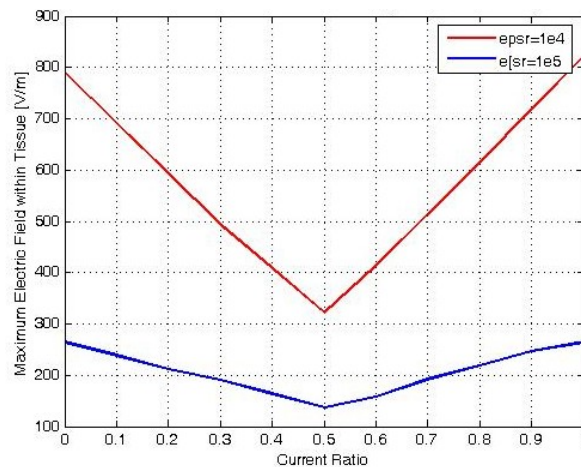


Figure 4-24 Maximum electric field vs. current steering ratio for different permittivity $\epsilon_r = 10^4$ and $\epsilon_r = 10^5$ at $\sigma = 0.1 \text{ S.m}^{-1}$

4.9 Electrode Array

Electrode array arrangement improves current steering and the spatial precision of charge delivery to targeted regions. A multi-shaft electrode array with 4 mm inter-electrode spacing was modeled and simulated as shown in Figure 4-25. The results emphasized the improved flexibility provided by electrode arrays in controlling field distribution.

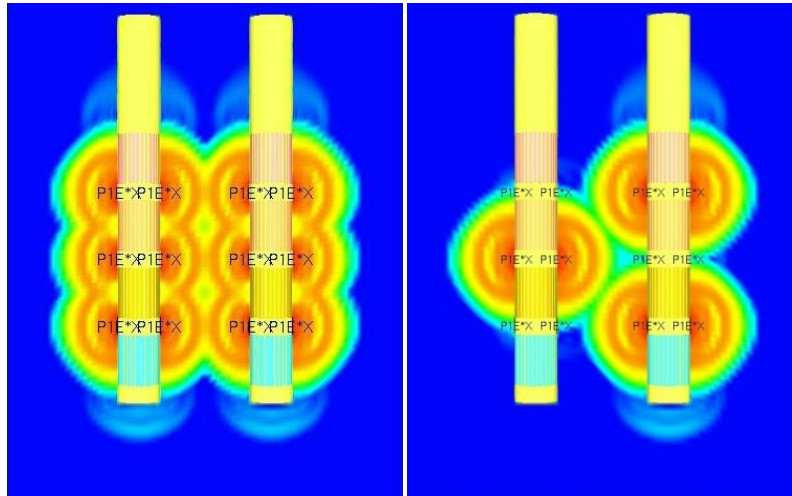


Figure 4-25 Two DBS electrode array, left: 100% current level on all rings, right: 0-100-0% (left shaft), 100-0-100% (right shaft).

4.10 Conclusion

The objective of this analysis was to investigate the effects of several DBS electrode parameters and brain tissue in controlling the electric field distribution within brain tissue and to provide a quantitative evaluation of the maximum electric field within the brain. These parameters include: tissue dielectric properties (permittivity and conductivity), non-homogenous tissue structure (Grey and White matter), encapsulation tissue thickness, stimulation pulse characteristics (width and amplitude) and stimulation pattern (current steering ratio). Low frequency models representing the Medtronic 3387 DBS electrode in the STN were developed based on the Gabriel biological tissue model.

Finite difference time domain (FDTD) was used for modeling and simulating the DBS electrode and the brain tissue medium for different DBS parameters. It is a very accurate method to solve the electric field since it deals with the temporal details of the input DBS parameters, hence, the influence of each parameter on the electric field distribution can be readily observed using FDTD analysis compared to FEM analysis. For the FEM method, we need to solve a system of linear equations at each time step and to run multiple executions to achieve similar temporal detail.

All of these parameters have an effect on the calculation of the activating functions as discussed in section 3.2, i.e. we do not need to study the effect of changing brain conductivity values ($0.02 - 0.3 \text{ S.m}^{-1}$) on the activating function since we already show that it has no effect on the electric field distribution, then a mean value of 0.1 S.m^{-1} was chosen in our analysis.

The simulation results showed that it is possible to maximize the efficacy of the charge delivered to a tissue by maximizing the spatial electric field distribution ; this can be achieved first by increasing stimulation pulse width especially when we used model-III as there was a shrink in the field between the layers in brain tissue (White and Grey matter). Second, when we took the encapsulation layer thickness into considerations (Model-II) as the values of the maximum electric field decreases when the encapsulation thickness increases. This encapsulation tissue layer was created in response to implanting a foreign body and thus attenuated the electric field.

Finally, we show that increasing stimulation pulse amplitude has only affected the field values without changing the depth of the field distribution. Also, stimulation pattern was modeled to investigate their efficacy in controlling the charge delivery and field shaping through current steering. The simulation results exhibited the ability to manipulate the electric field distribution within the brain tissue though controlling the ratios of the differential stimulation signal components between ring pairs.

In conclusion, we have focused on three different models of the implanted electrode inside brain tissue, starting with a homogenous and isotropic brain tissue medium (Model-I), an encapsulation layer surrounding the implanted electrode (Model-II) which represents the aging process of the implanted electrode inside brain tissue and finally, a non-homogenous tissue structure (Model-III) including Grey and White tissue matter in order to investigate the effect of the insertion of the electrode with respect to different tissue layers. All of these three models were investigated to study their effect on the electric field distribution and the results show the capability of controlling the field distribution to conform to the brain target of the stimulation and thus minimizing the stimulation of undesired brain structures.

Chapter 5

Evaluating the Activating Function in Deep Brain Stimulation System

5.1 Introduction

As mentioned in Chapter 3, Figure 3-2, there is a component (second order spatial voltage) that is responsible for conversion from electric field distribution to activating function. This activating function is needed to stimulate neuron cells inside the brain. This conversion component uses the electric field as its input in order to calculate the second order spatial voltage as shown in

Figure 5-1.

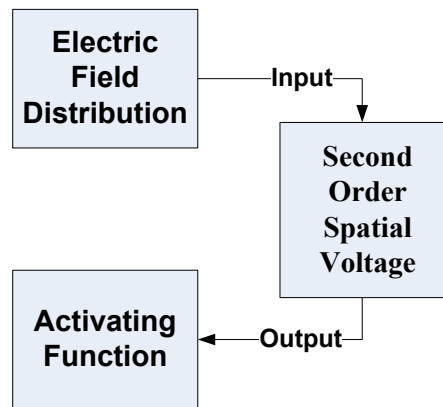


Figure 5-1 A schematic diagram for the input and output of the second order spatial voltage component

The EMPIRE XCcel 5.2 tool (FDTD electromagnetic solver) allows only dealing with electric field distribution. Using this tool, we cannot integrate the electric field along any path around the DBS electrode. This spatial integration along any path emitted from the DBS electrode at any position is required to find the spatial voltage distribution which as mentioned before is required to stimulate the neuron cells. This was a major reason behind changing the simulation tool and searching for another electromagnetic solver with such capabilities to find the electric field and voltage distribution at any spatial position from the DBS electrode.

The finite element method (FEM) was considered in the modeling of the Medtronic DBS electrode to solve for the electric field and the voltage distribution. However, FEM is a

frequency domain solver which does not handle temporal signal details, thus, in order to estimate the field distribution associated with a certain pulse; the time domain signals should be sampled, transformed into the corresponding discrete frequency domain representation using Finite Fourier Transform (FFT). The result at each component frequency is converted back to the time domain with an inverse Fourier transform. Although this technique allows calculation of the voltage distribution, it doesn't lend itself easily to investigate the effects of the DBS electrode stimulation parameters on the electric field as we showed in the previous chapter.

In DBS, pulse widths are varied and it was clinically suggested that stimulus pulse durations should range from 60-450 μ s. The Fourier transform of the stimulus waveform in the frequency domain using a 1024 point FFT technique is shown in Figure 5-2 for a 60 μ s Monophasic Pulse.

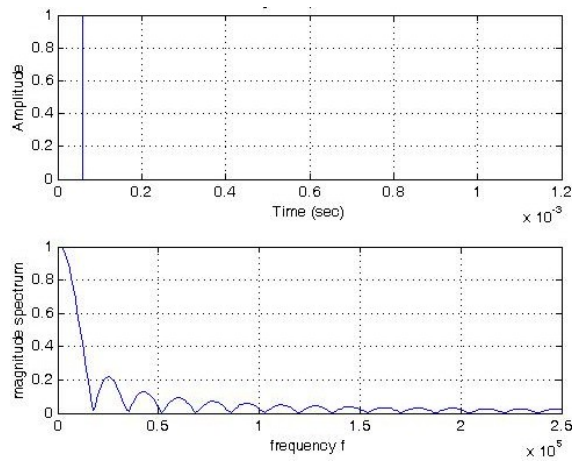


Figure 5-2 A 60 μ s monophasic pulse and its FFT magnitude

5.2 Electromagnetic Solution

The electric and voltage field distribution were solved using a numerical technique based on Finite Element Methods (FEM). The commercially available software package COMSOL Multiphysics v3.2 (Comsol Inc, Burlington, Massachusetts) [48] was used to determine the electric field and the electric potential (V) distribution in the brain medium due to the stimulating electrodes by solving the Laplace Equation:

$$\nabla \cdot \sigma_c \nabla V = 0 \quad (5.1)$$

where σ_c is the electrical conductivity of the media involved in the model.

The stimulus waveform is a train of voltage square pulses with a main frequency between 100-150 Hz. To account for frequency dependence of the brain tissue, complex conductivities of tissues were considered:

$$\sigma_c = \sigma + j\omega\epsilon_0(\epsilon' - j\epsilon'') \quad (5.2)$$

where σ is the ionic conductivity, ϵ' (free charge) and ϵ'' (bound charge) are the real and imaginary parts of the tissue permittivity. These values were extracted at 130 Hz from the Figure 4-1, Figure 4-2, Figure 4-3 and Figure 4-4

5.3 Finite Element Model

Axisymmetric finite element models of DBS electrodes were created with 17,560 nodes using COMSOL. The axisymmetric volume representing the brain medium measured 20 mm tall by 10 mm wide to evaluate the electric field and voltage distribution. This axisymmetric 2D space was chosen instead of a more realistic 3D to achieve a reliable solution without a high computational effort as shown in Figure 5-3.

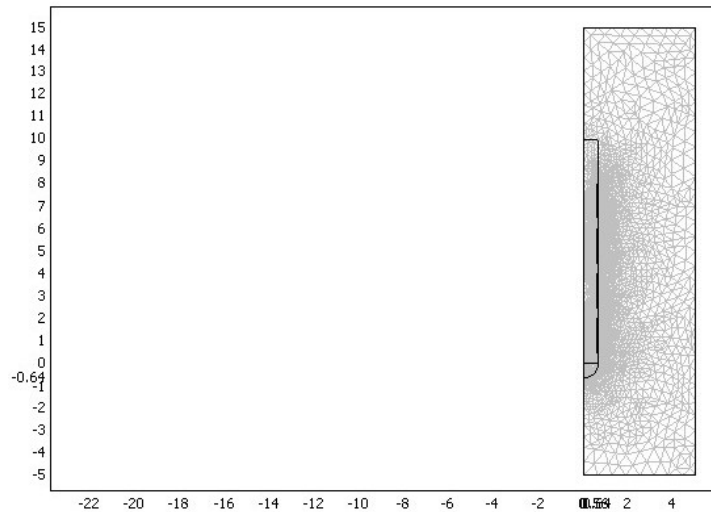


Figure 5-3 Finite element meshing for the DBS electrode in Model-I

The brain tissue medium was modeled as Grey tissue as a homogenous lossy dielectric (Model-I) with isotropic conductivity of 0.1 S/m, a representative value for brain tissue. The electrode geometry was based on the Medtronic 3387 quadripolar DBS electrode with four platinum contact rings ($\sigma = 8.6 \cdot 10^6$ S/m) on its perimeter for charge delivery. The rings have a thickness of 80 μm and 1.5 mm in height with a spacing of 0.5 mm. The voltage sources were specified at the electrode contacts, and the electrode shaft was modeled as an electrical insulator polyurethane polymer.

5.4 Stimulation Results

Monophasic stimulation pulse was considered because it is the common approach used in DBS procedure. All the stimulus pulses applied to the electrode contacts have a frequency of 130 Hz and 60 μs width. First, we implied a negative square pulse voltage at the first DBS electrode contact of negative 0.5 volt. Therefore, we set contact No. 1 to $V = -0.5$ volt and the system were solved using a FEM solver. Figure 5-4 shows the electrical potential contour results. The data provided by the simulations is the maximum electric field intensity distribution within the brain tissue.

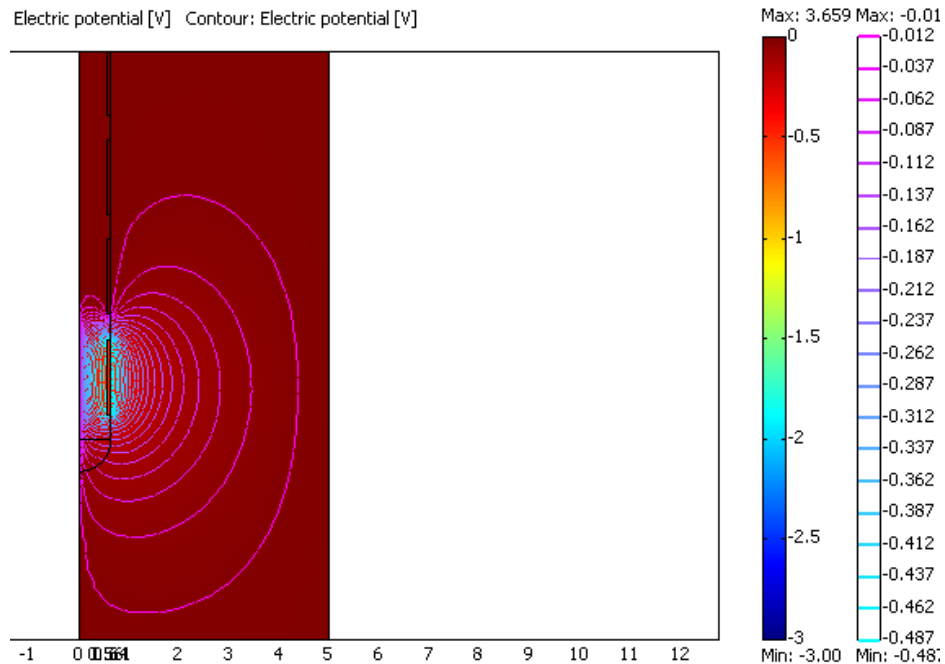


Figure 5-4 Finite element potential contour of DBS electrode for $V = -0.5$ Volt

Secondly, this scenario was repeated for different negative square pulse voltages applied at the first electrode contact with the same width $60 \mu\text{s}$ but different amplitudes ranging -1,-2 and -3 voltages. Figure 5-5, Figure 5-6 and Figure 5-7 show the electrical potential contour results for this applied voltages as well as how the electrical voltage intensities increase through the brain tissue with the applied voltage. We kept the same voltage scale legend for all figures.

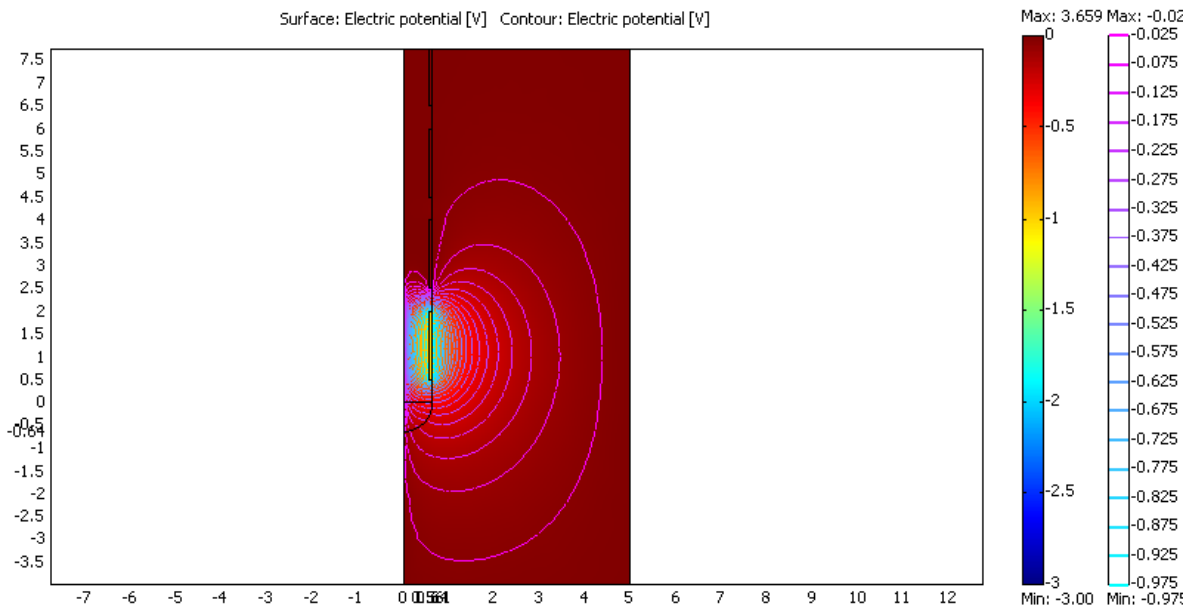


Figure 5-5 Finite element potential contour of DBS electrode for $V = -1.0$ Volt

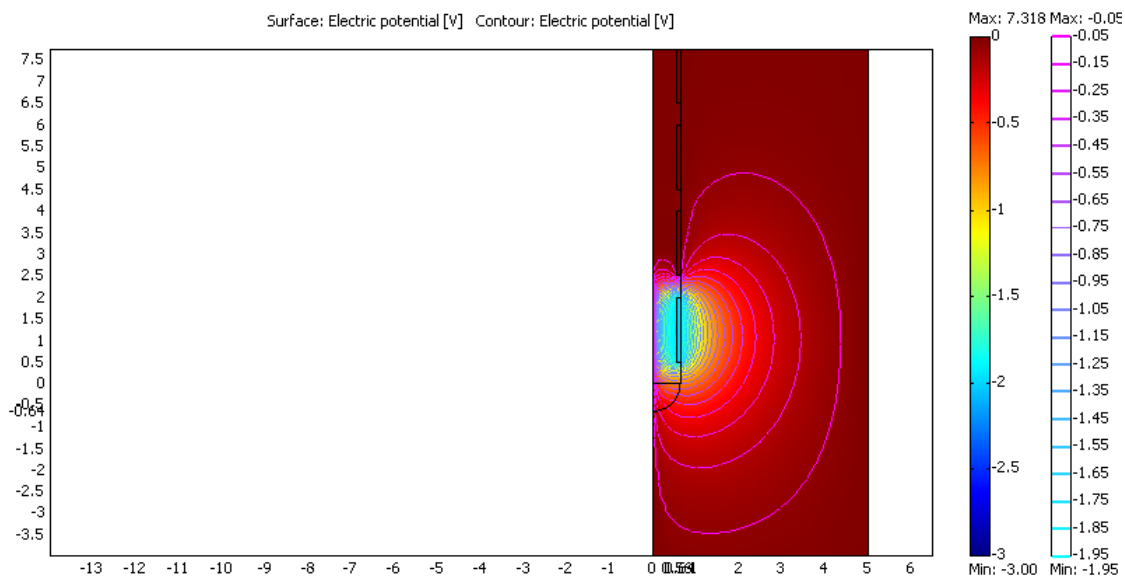


Figure 5-6 Finite element potential contour of DBS electrode for $V = -2.0$ Volt

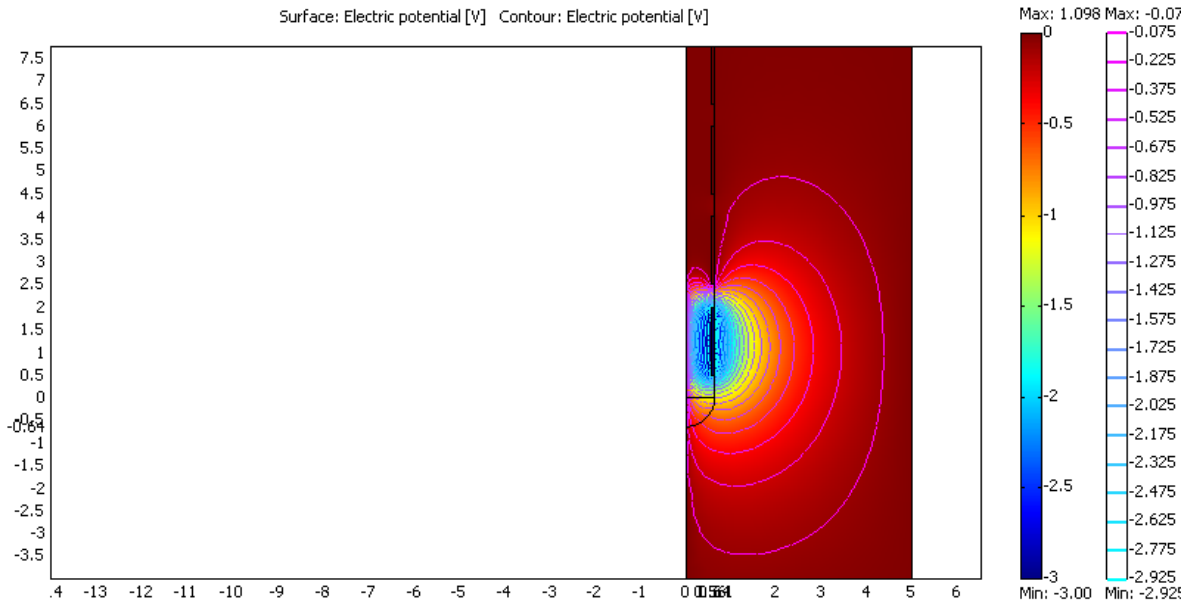


Figure 5-7 Finite element potential contour of DBS electrode for V= -3.0 Volt

From these electric field distributions, we can integrate the electric field along any path from the DBS electrode shaft which was the main reason behind the switching from FDTD into FEM. As an example, the electrical voltage distribution along a vertical line passing 1 mm on the right of the active Contact No. 1 is calculated for two applied voltage cases of -1 and -3 respectively as shown in Figure 5-8 and Figure 5-9.

The maximum electric field intensity within the brain tissue was found to be equal to 7.828 KV/m within 4.5 mm penetration depth for the case when the applied voltage equal to -1 Volt; this estimates the volume of tissue activated (VTA) according to the depth of the electric field penetration into the brain tissue. This calculation was repeated for a different contact voltage of -3 volt and the maximum electric field intensity within the brain tissue was equal to 33.484 KV/m within the same 4.5 mm penetration depth. This confirms the same result done before with FDTD that the pulse amplitude had no effect on the depth of field penetration within the tissue while directly controlled the levels of field intensity.

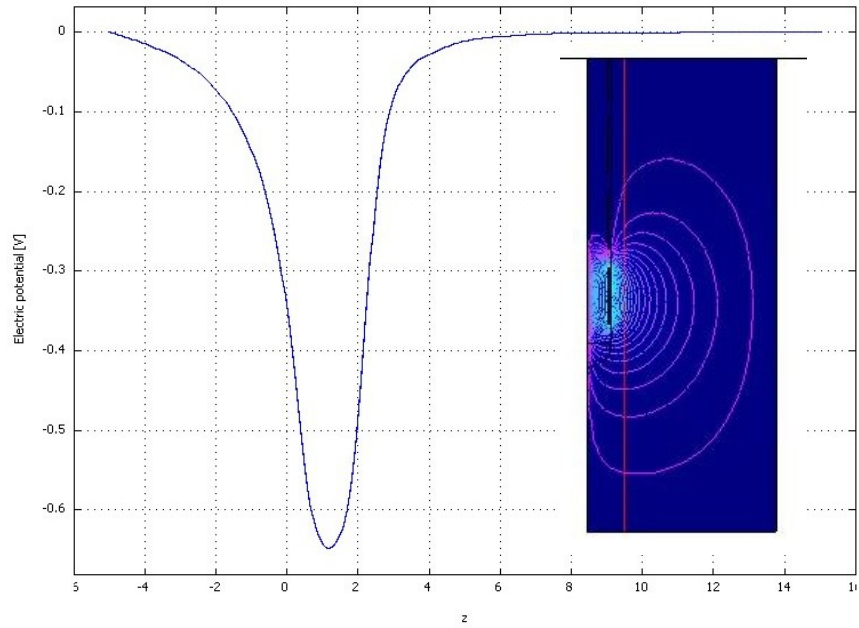


Figure 5-8 Electric potential along a vertical line passing 1 mm on the right of the active contact No. 1 for $V = -1$ volt.

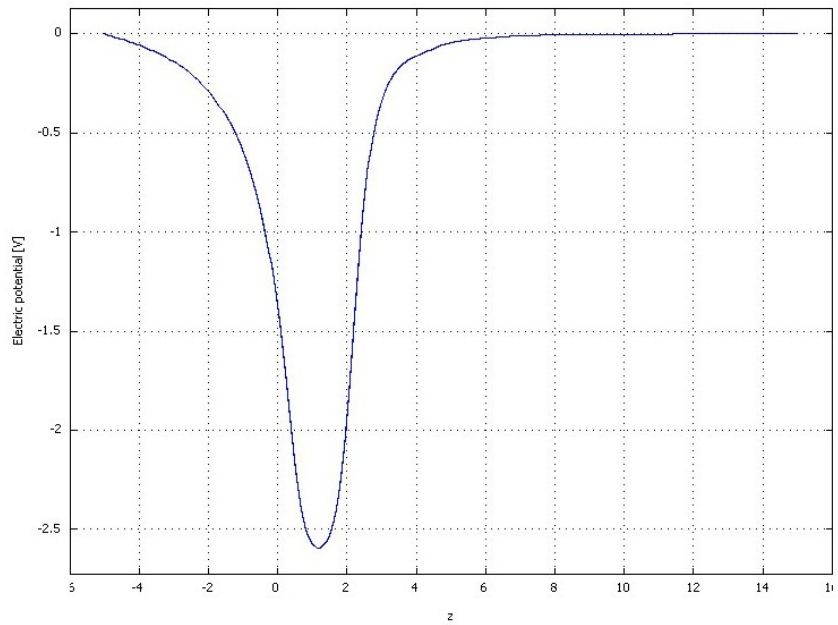


Figure 5-9 Electric potential along a vertical line passing 1 mm on the right of the active contact No. 1 for $V = -3$ volt.

Finally, the DBS electrode four contacts were activated with a pattern (-3, -2, -1 and -0.5 volts) for contacts 1 to 4 respectively, the electric potential contours around the electrode were shown in Figure 5-10 where the maximum electric field within the tissue was found to be 23.637 KV/m which is approximately the same value when we applied a negative 3 volt on one active contact. Figure 5-11 also shows the voltage distribution along a horizontal axis passing through the first contact and the brain tissue.

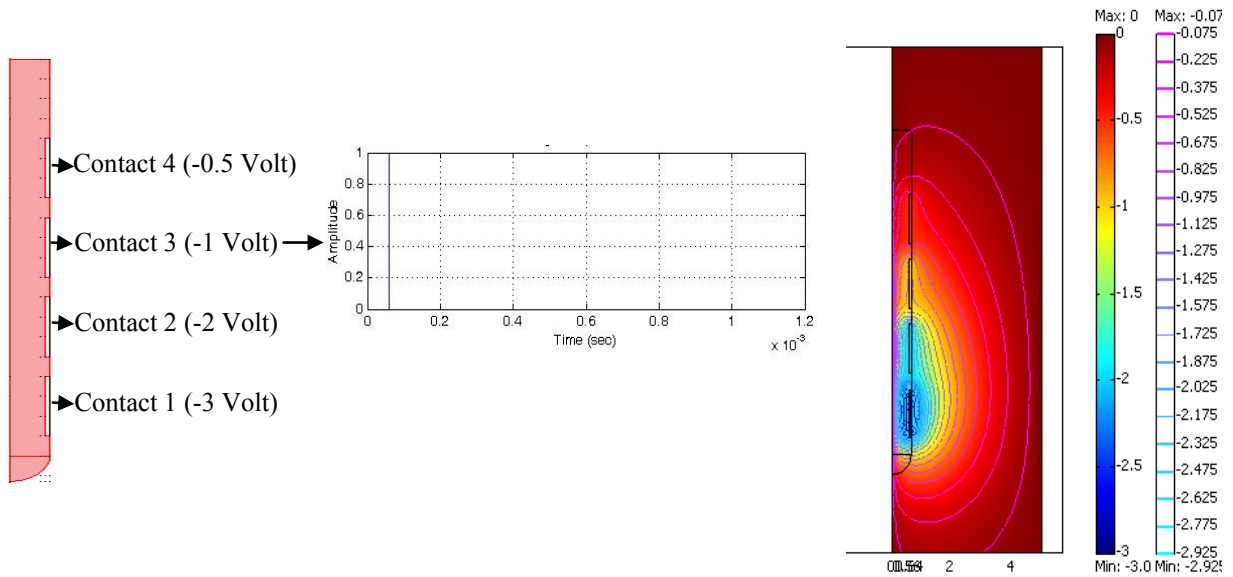


Figure 5-10 Finite element potential contour of DBS electrode for 4 active contacts (-3, -2, -1 and -0.5 volts.)

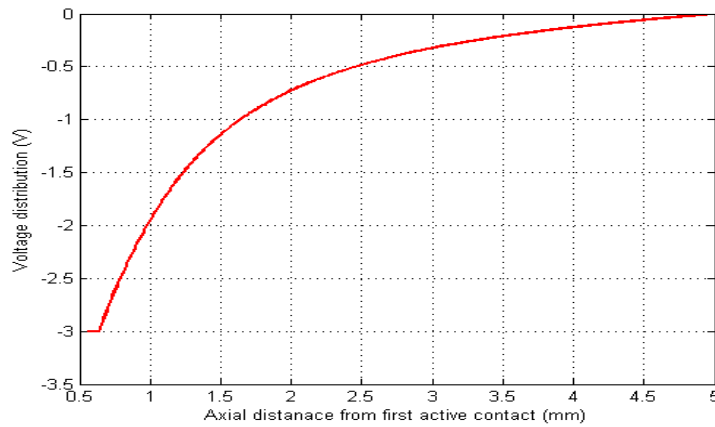


Figure 5-11 Electric potential along a horizontal axis passing through the first active contact.

5.4.1 Activating Function Calculation along Lateral Axis of the Electrode

The space-dependent voltages are used to calculate the activating functions for neurons. The concept of an activating function was developed and suggested in [41]. In order to describe and simplify the computations involved in determining the response of excitable tissue to an electric field. This function is defined as the second derivative of the extracellular potential along a fiber and represents the driving function of a neuron. It has mainly been used to estimate the existence of regions of polarization in the (depolarization and hyperpolarization) and can be used to predict action potential initiation.

The activating function was calculated along multiple vertical lines located at different distances from the DBS electrode shaft. These positions will later represent locations of neuron cells. In this way we will be able to find the activity of each neuron relative to its position with respect to either a positive activating or negative activating function as shown in Figure 5-12.

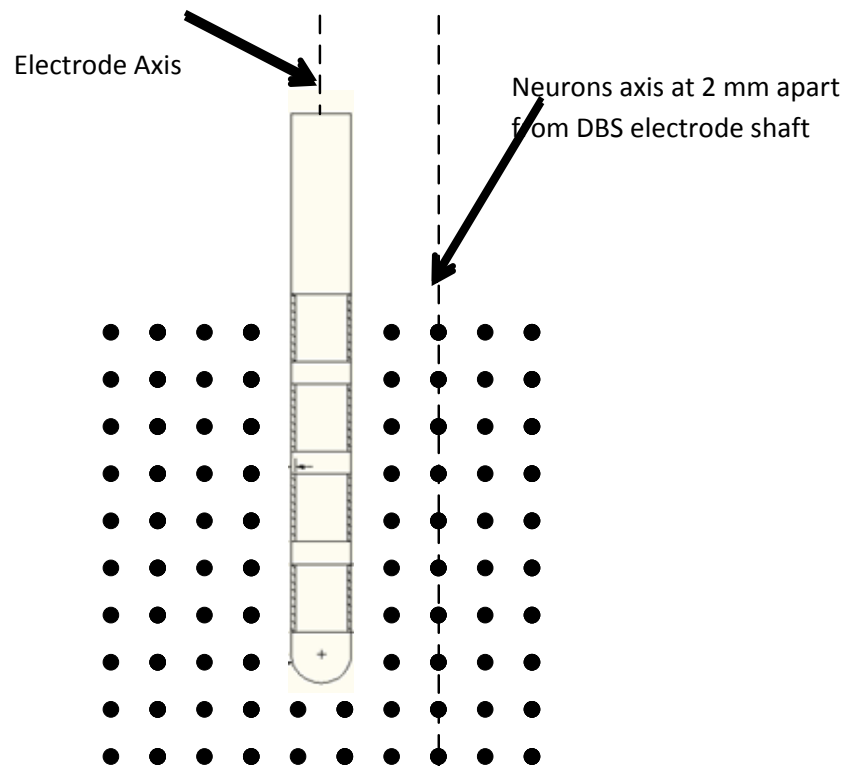


Figure 5-12 A schematic diagram of DBS electrode with respect to surrounding neurons where the activating function will be calculated at positions lateral to the electrode shaft

First, We will start our calculations by applying a negative one voltage at the first contact of the DBS electrode, Figure 5-13 reports the voltage distribution (panel a) and the activating function (panel b) along a vertical line passing 1 mm to the right of the active contact No. 1 with -1 volt. It can be shown that positive activating function value will lead to a higher probability of depolarization and negative activating function values lead to hyperpolarization.

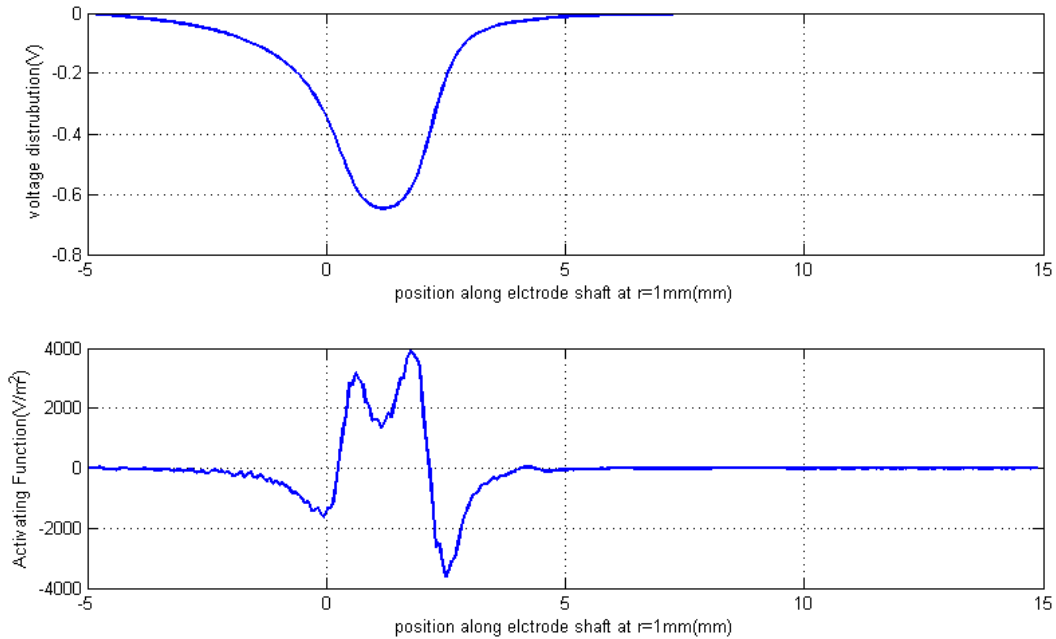


Figure 5-13 Electric potential and activating function along a vertical line passing 1 mm from DBS active contact No. 1 for $V = -1$ volt.

The activating function was then calculated along multiple vertical lines passing 2mm and 3mm to the right of the position of the DBS electrode due to symmetry as shown in Figure 5-14 and Figure 5-15. It can be shown that the maximum and the minimum values of the activating function are decreasing relative to the distance apart from the electrode which will affect action potential initiation and hence the volume of tissue activated (VTA) inside the brain. Table 5-1 summarizes these values.

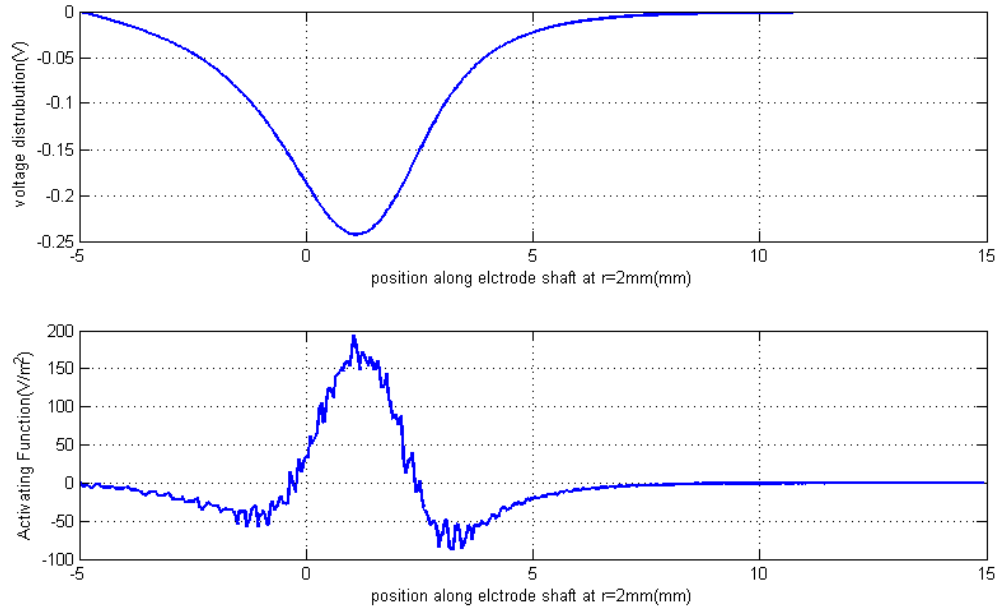


Figure 5-14 Electric potential and activating function along a vertical line passing 2 mm from DBS active contact No. 1 for $V = -1$ volt.

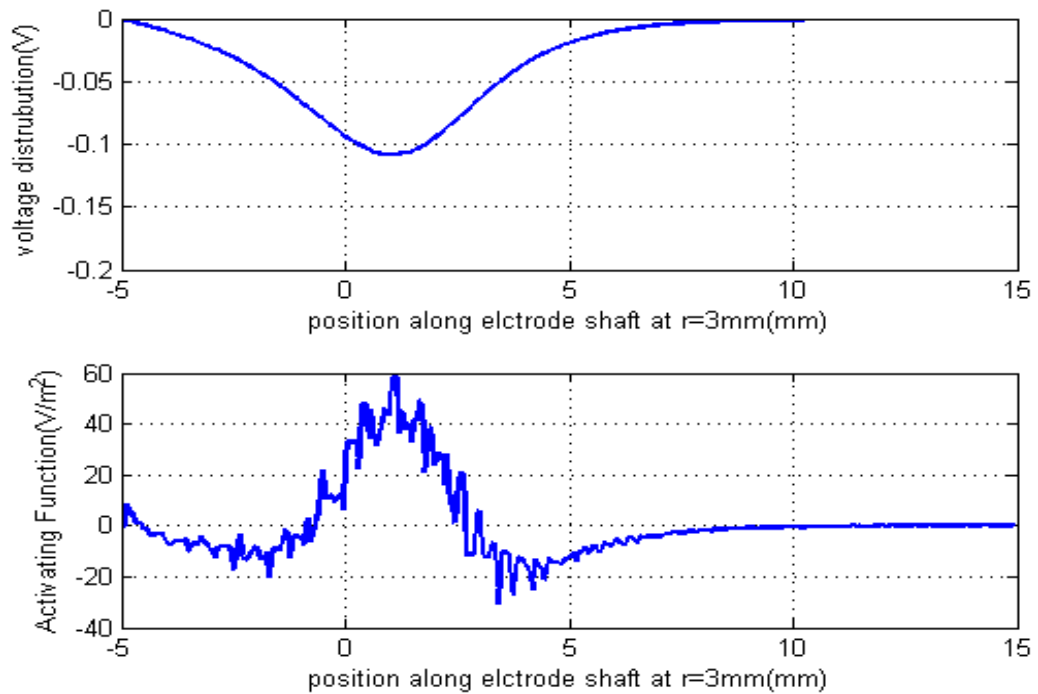


Figure 5-15 Electric potential and activating function along a vertical line passing 3 mm from DBS active contact No. 1 for $V = -1$ volt.

Table 5-1 Maximum and minimum activating function (AF) [V/m²] for different positions from the electrode shaft

Position	AF(Max) V/m ²	AF(Min) V/m ²
1mm	3.919*10 ³	-3.601*10 ³
2mm	0.1936*10 ³	-0.08646*10 ³
3mm	0.05804*10 ³	-0.03072*10 ³

The effect of neuron position from the DBS electrode shaft, were calculated based on the activating function maximum value, is modeled for the case when a negative one voltage was applied to the DBS electrode first contact. Matlab Linear regression with Power series equation provided the most accurate model with a minimum root mean square error (RMSE) and maximum coefficient of determination R^2 , with confidence bounds of 95% (Figure 5-16). The extracted equation for the maximum activating function AF_{max} is:

$$AF_{max}(x) = 3.919 * 10^3 x^{-4.292} \quad [V/m^2] \dots (5.3)$$

where x in mm and $R^2 = 99.98\%$, and $RMSE = 23.83$

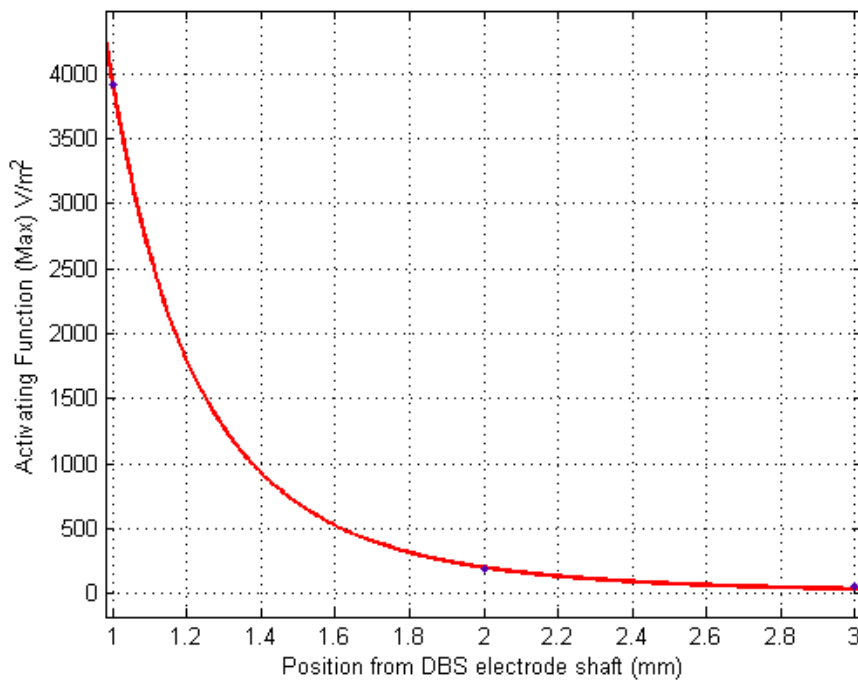


Figure 5-16 Maximum activating function (AF_{max})[V/m²] for different positions from the electrode shaft for V= -1 volt applied to the DBS electrode first contact.

Secondly, we applied a negative three volts at the first contact of the DBS electrode ($V = -3$ Volt); Figure 5-17 reports the voltage distribution and the activating function along a vertical line passing 1 mm on the right of the active contact No. 1 with -3 volt.

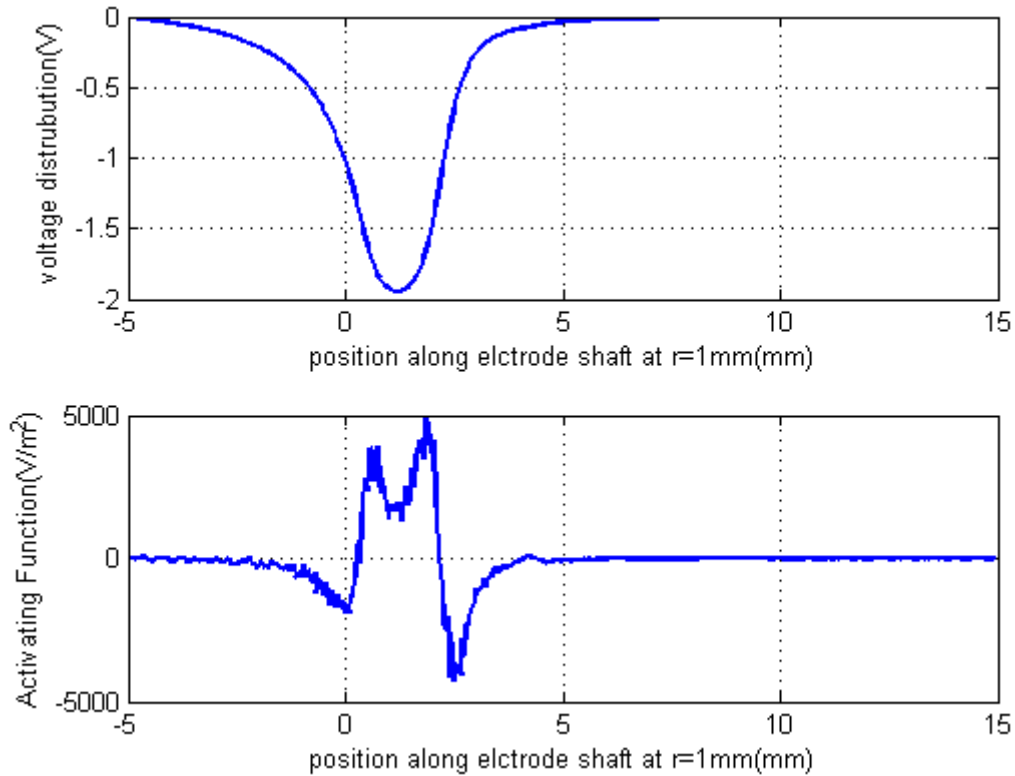


Figure 5-17 Electric potential and activating function along a vertical line passing 1 mm from DBS active contact No. 1 for $V = -3$ volt.

The activating function was subsequently calculated along a multiple vertical line passing 2mm, 3mm and we add the 4mm distance from the DBS electrode since we are expecting the values of this function to decay at a lower rate compared to the case when we applied negative one voltage. It can be shown in Figure 5-18, Figure 5-19 and Figure 5-20 that the maximum and the minimum values of the activating function are still decreasing relative to the distance apart from the electrode but these values are greater than the previous case when a negative one volt was applied. Hence, the probability of the number of neurons that are firing and the volume of tissue activated are expected to be much larger. Table 5-2 summarizes these values.

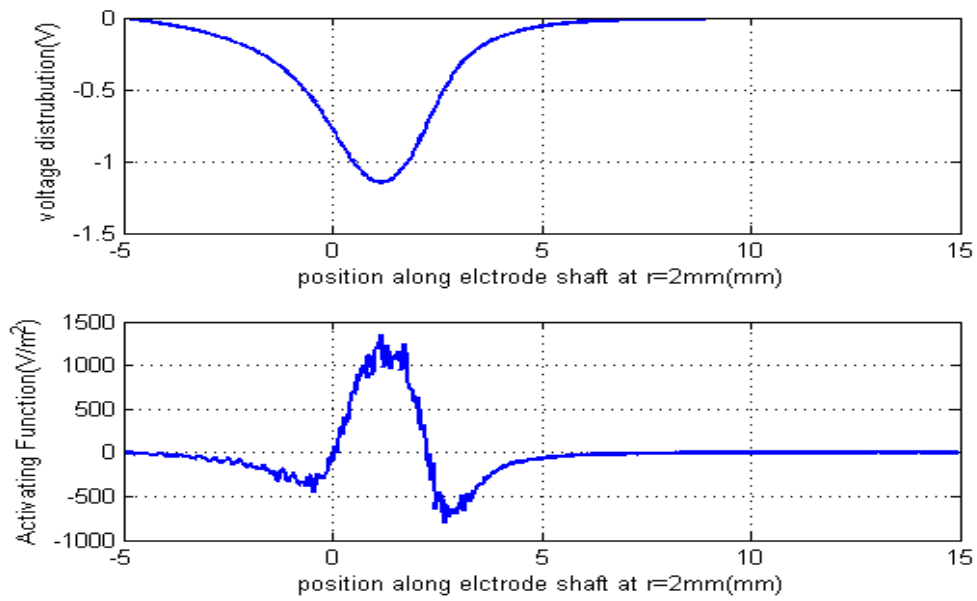


Figure 5-18 Electric potential and activating function along a vertical line passing 2 mm from DBS active contact No. 1 for $V= -3$ volt.

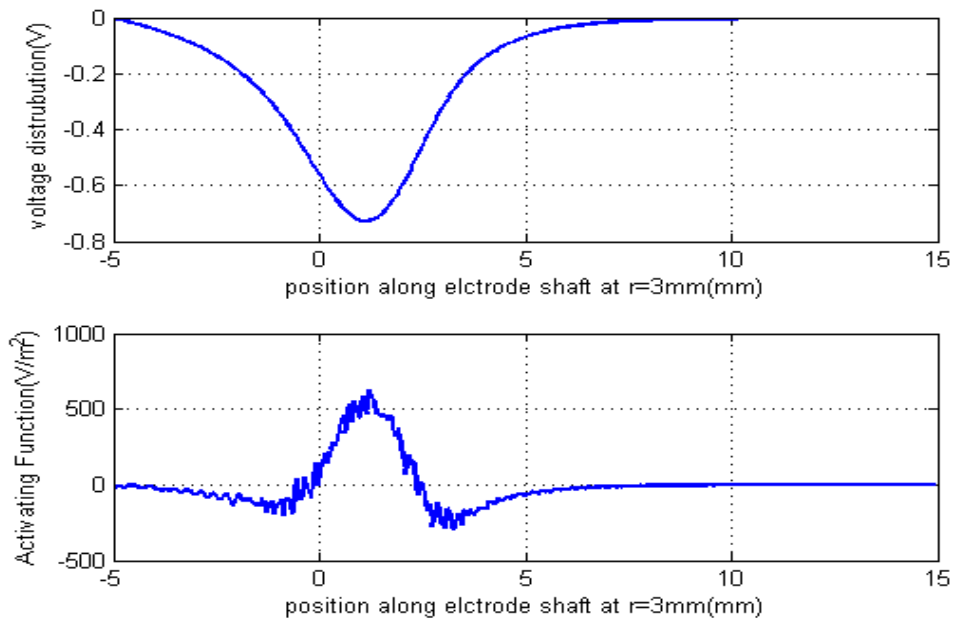


Figure 5-19 Electric potential and activating function along a vertical line passing 3 mm from DBS active contact No. 1 for $V= -3$ volt.

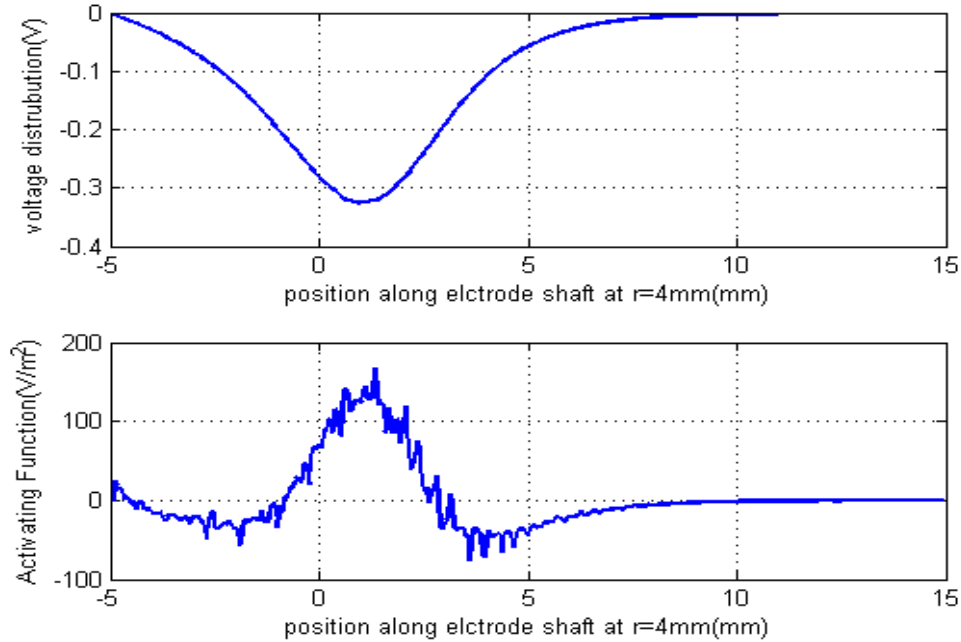


Figure 5-20 Electric potential and activating function along a vertical line passing 4 mm from DBS active contact No. 1 for V= -3 volt.

Table 5-2 Maximum and minimum activating function (AF) [V/m²] for different positions from the electrode shaft

Position	AF(Max) V/m ²	AF(Min) V/m ²
1mm	4.942*10 ³	-4.261*10 ³
2mm	1.351*10 ³	-0.851*10 ³
3mm	0.6242*10 ³	-0.2926*10 ³
4mm	0.1674*10 ³	-0.07671*10 ³

Again, the effect of the position of neurons from the DBS electrode shaft is modeled for this case as shown in Figure 5-21 (we used the activating function curve for the case when V= -1 volt and we deduce the value of the AF_{max} at 4 mm from equation 5.3 which leads to a value of 0.0102*10³ V/m²) to show how this function is affected with respect to the applied voltage. Matlab Linear regression with Power series equation provided the most accurate model with a minimum root mean square error (RMSE) and maximum coefficient of determination R², with confidence bounds of 95% The extracted equation for AF_{max} is:

$$AF_{max}(x) = 4.951 * 10^3 x^{-1.941} \quad [V/m^2] \dots (5.4)$$

where x in mm and $R^2 = 99.76\%$, and $RMSE = 129.7$

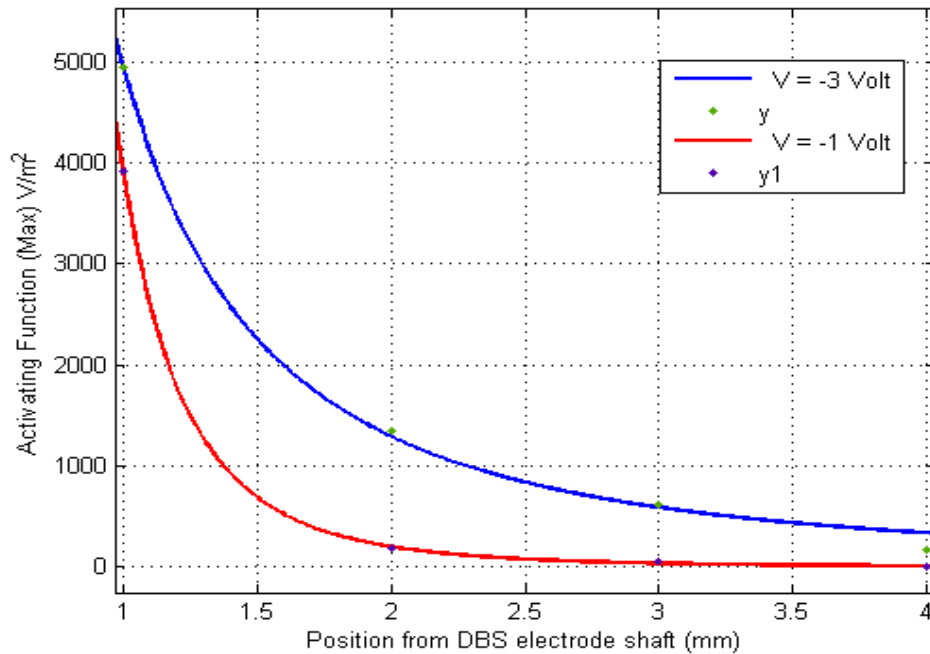


Figure 5-21 Maximum activating function (AF_{max}) $[V/m^2]$ for different positions from the electrode shaft for $V = -3$ volt compared to the case when $V = -1$ volt applied to the DBS electrode contact.

5.4.2 Activating Function along Tilted Axis with Respect to DBS Electrode Shaft

In the previous section, we calculated activating function along parallel axis to the DBS electrode shaft, in this section we studied the effect of calculating the activating function on multiple tilted axes along different degree angles from the DBS electrode shaft as shown in Figure 5-22. To prove that maximum depolarization at which there is a highest possibility for the neurons to fire occurs when activating function calculated on axis's that are parallel to the electrode shaft due to the rate of change of the electric field assigned to the DBS electrode.

The electric potential and activating function was calculated along multiple axes with different degree angles starting from 10 degree angle till 55 degree as shown in Figure 5-23, Figure 5-24, Figure 5-25, Figure 5-26 and Figure 5-27.

The maximum and the minimum values of the activating function are decreased relative to the different angles from the DBS electrode shaft and it drops to relatively small values when the

angle between the DBS electrode and axis of calculation reached 30 degree or more indicating less probability of firing neurons. Furthermore, the electric potential and activating function were calculated at an axis that is perpendicular to the DBS electrode shaft (90 degree) as shown in Figure 5-28 which shows only a negative value of activating function meaning that there will be no action potential initiated and hence all the neurons located along this path are in the hyperpolarization region and there will be no firing initiated. Table 5-3 summarizes these values.

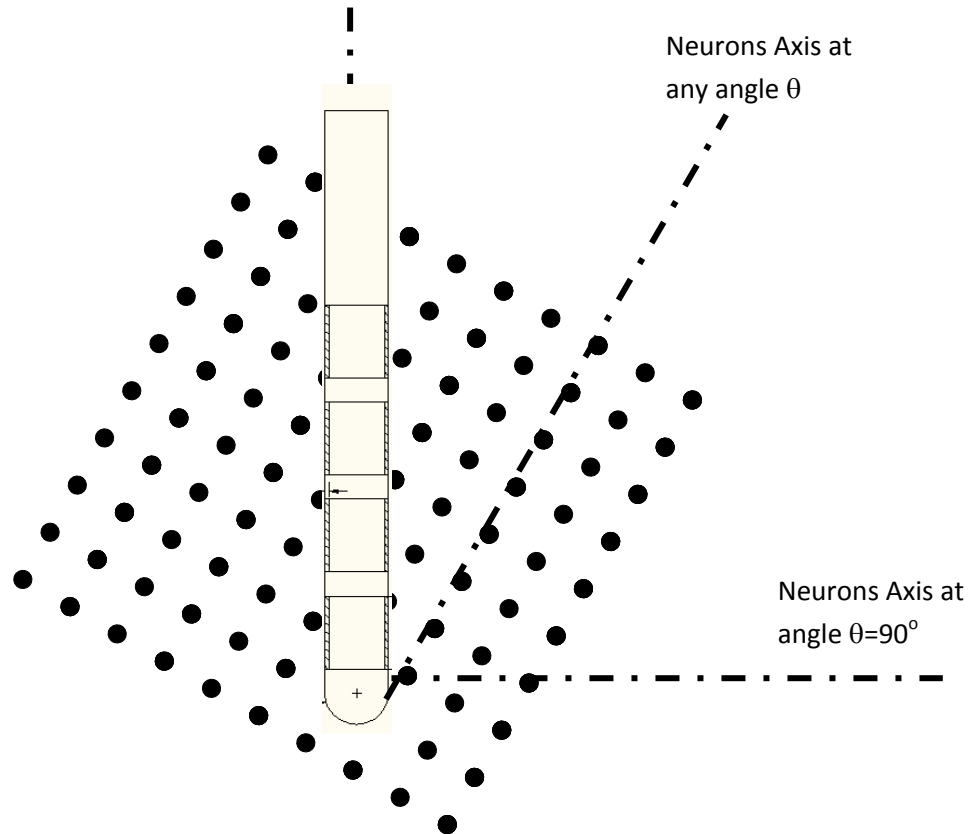


Figure 5-22 A schematic diagram of DBS electrode with respect to surrounded neurons where the activating function will be calculated along tilted axis with respect to electrode shaft

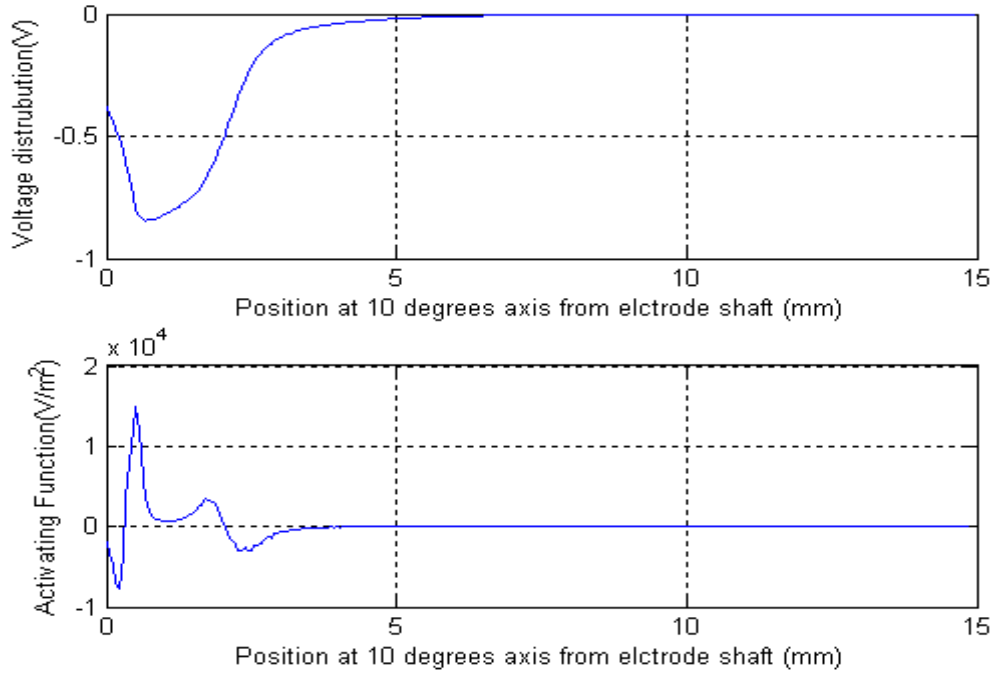


Figure 5-23 Electric potential and activating function along a 10 degree angle from the electrode axis

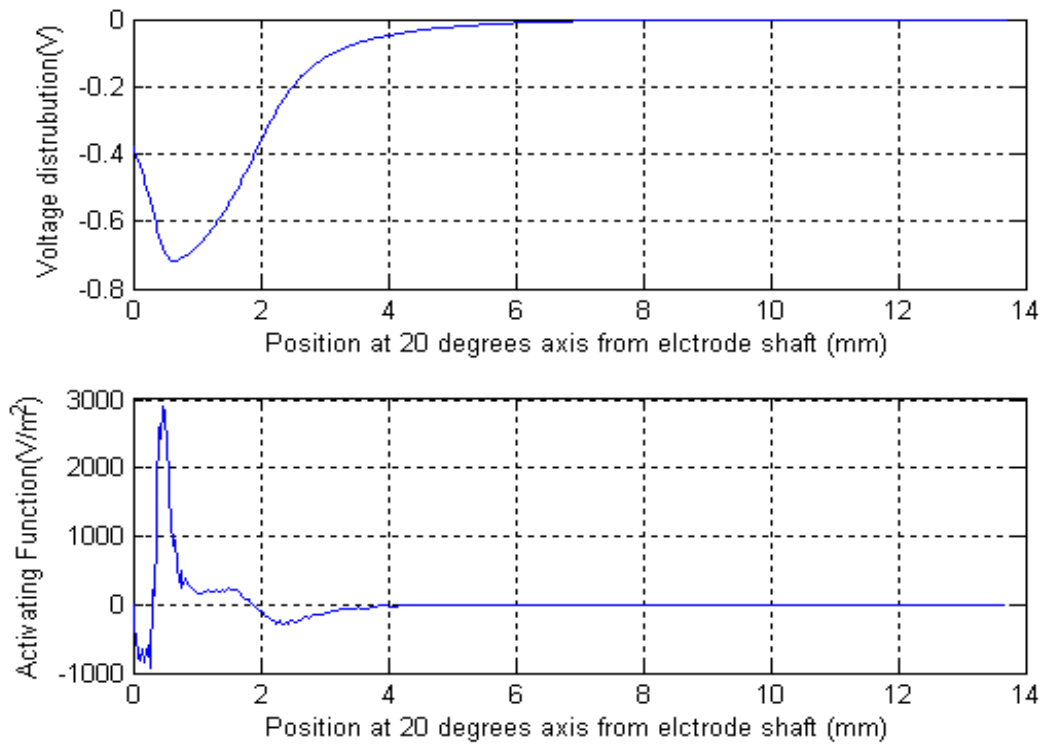


Figure 5-24 Electric potential and activating function along a 20 degree angle from the electrode axis

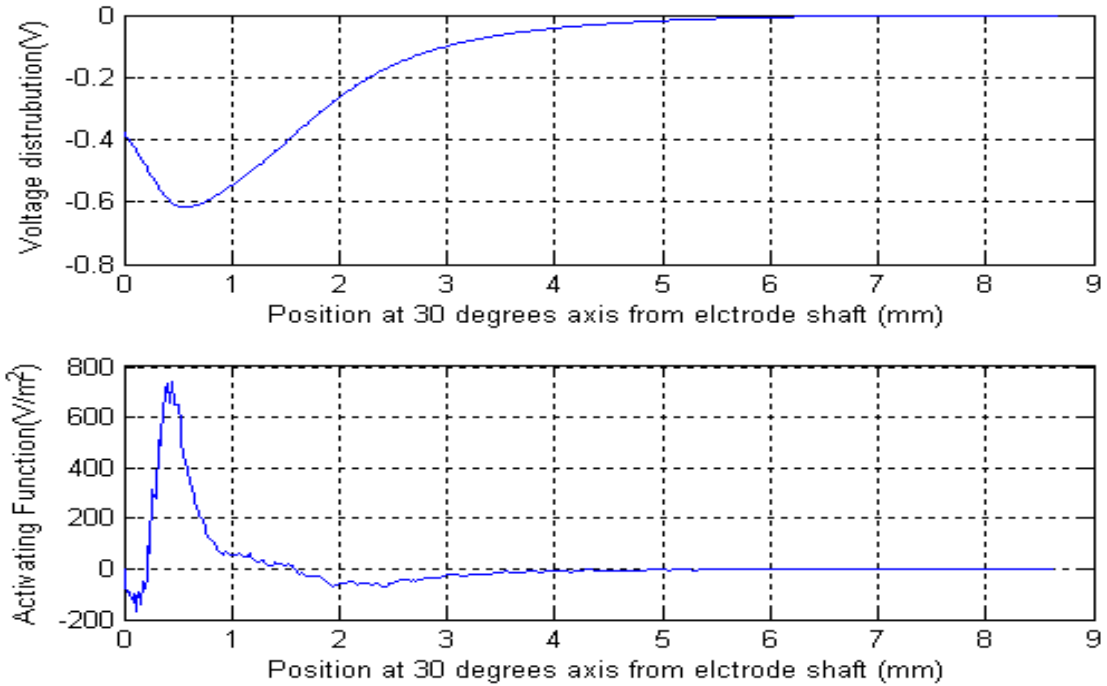


Figure 5-25 Electric potential and activating function along a 30 degree angle from the electrode axis

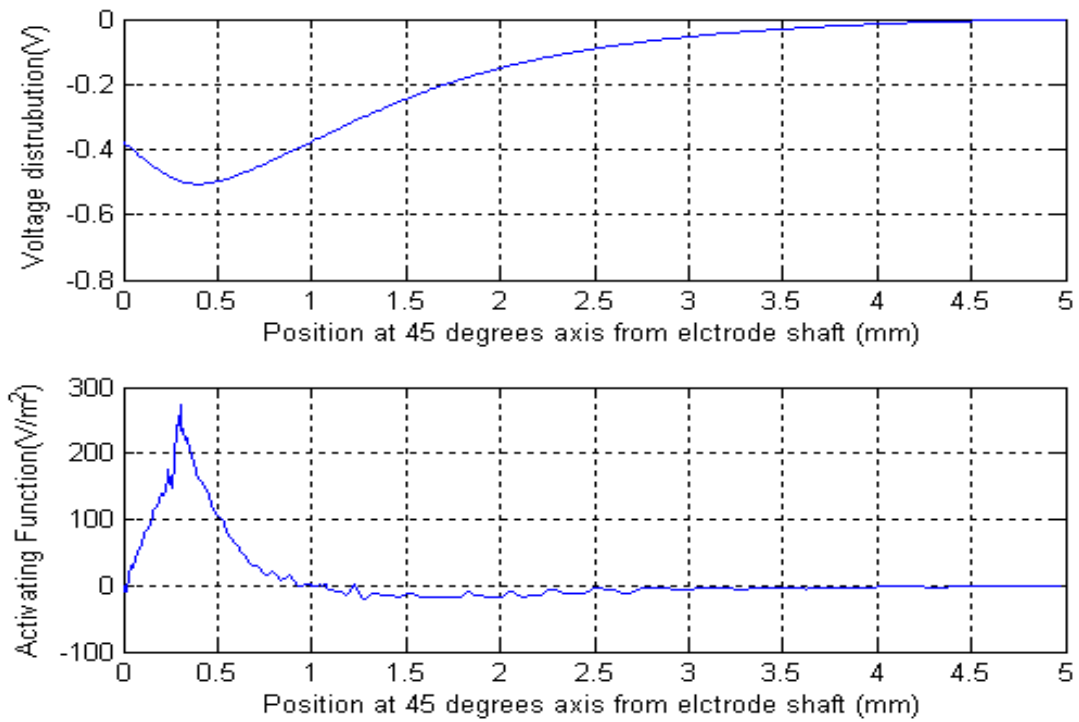


Figure 5-26 Electric potential and activating function along a 45 degree angle from the electrode axis

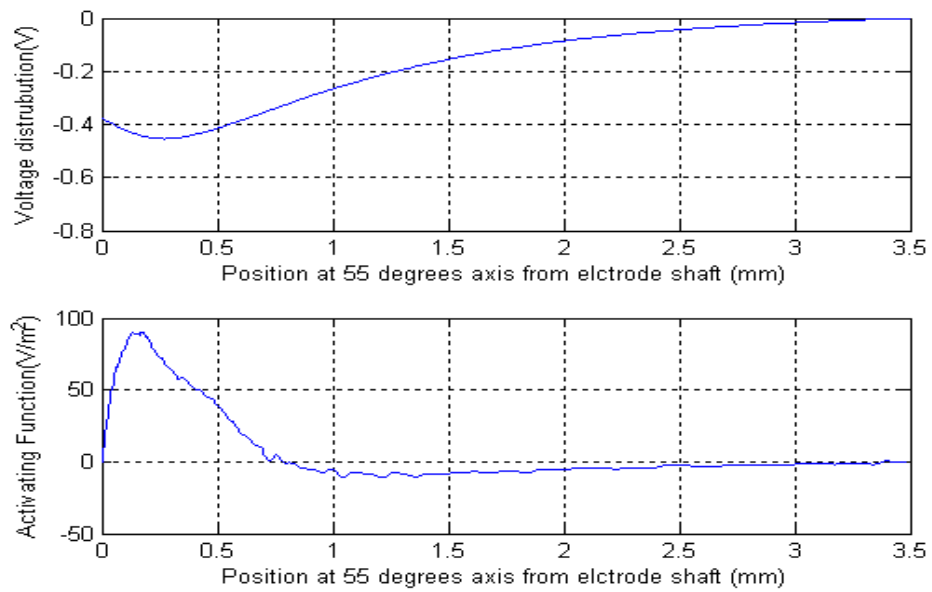


Figure 5-27 Electric potential and activating function along a 55 degree angle from the electrode axis

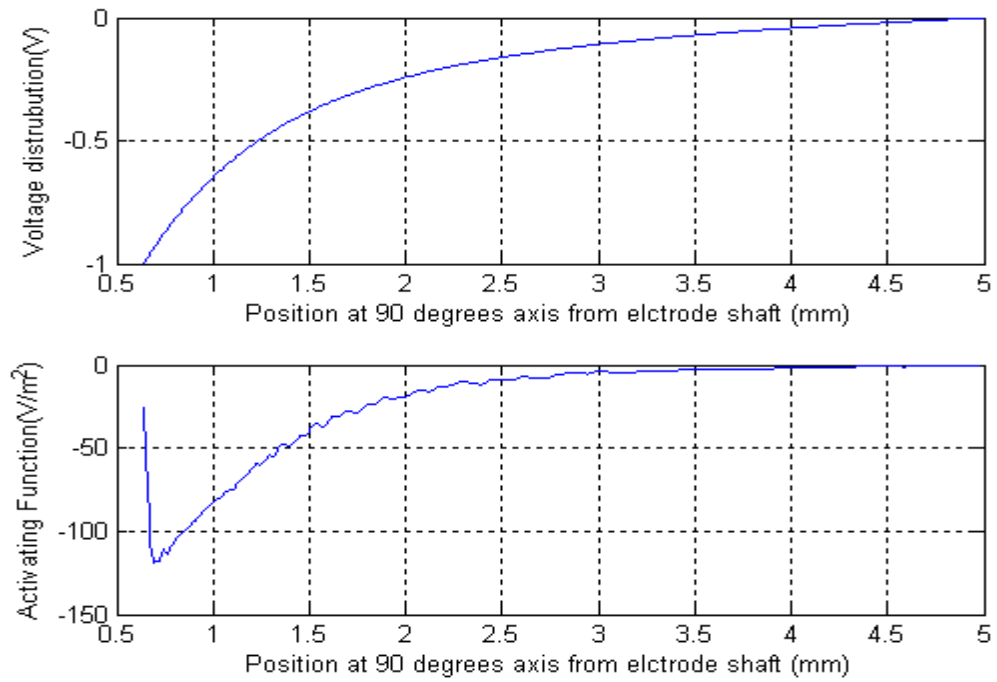


Figure 5-28 Electric potential and activating function along a 90 degree angle from the electrode axis

Table 5-3 Maximum and minimum activating function (AF) [V/m²] for different degree angles from the electrode shaft

Position	AF(Max) V/m ²	AF(Min) V/m ²
10 degree	14.98*10 ³	-7.621*10 ³
20 degree	2.889*10 ³	-0.725*10 ³
30 degree	0.740*10 ³	-149.8*10 ³
45 degree	0.270*10 ³	-0.020*10 ³
55 degree	0.090*10 ³	-0.008*10 ³

The value of the zero degree position was not considered in this analysis because it represents a parallel position to the DBS electrode shaft and it was considered before in section 5.4.1. Also, we noticed that after the 55 degree position, the maximum value of the activating function dropped to zero values, and it even goes to negative values at 90 degree angle from the DBS electrode shaft as shown in Figure 5-28.

We observed that the maximum value of the activating function calculated at the 10 degree angle position was extremely increased to 14.98*10³ V/m², this is due to the rapid change of the voltage distribution along this position from its minimum to maximum values which guaranteed a higher activating function, while in the other cases (different angle positions greater than 10 degree or even parallel manner positions), the voltage distribution changing smoothly from its minimum to maximum values.

The effect of the different degree angle from the DBS electrode shaft (where activating function was calculated) on the maximum activating function is modeled. Matlab Linear regression with exponential equation provided the most accurate model with a minimum root mean square error (RMSE) and maximum coefficient of determination R^2 , with confidence bounds of 95% (Figure 5-29). The extracted equation of AF_{max} is:

$$AF_{max}(\theta) = 7.56 * 10^4 \exp(-0.1619 * \theta) \quad [V/m^2] \dots \quad 10 \leq \theta \leq 55 \quad (5.5)$$

where θ in degree and $R^2 = 99.95\%$, and $RMSE = 166.5$,

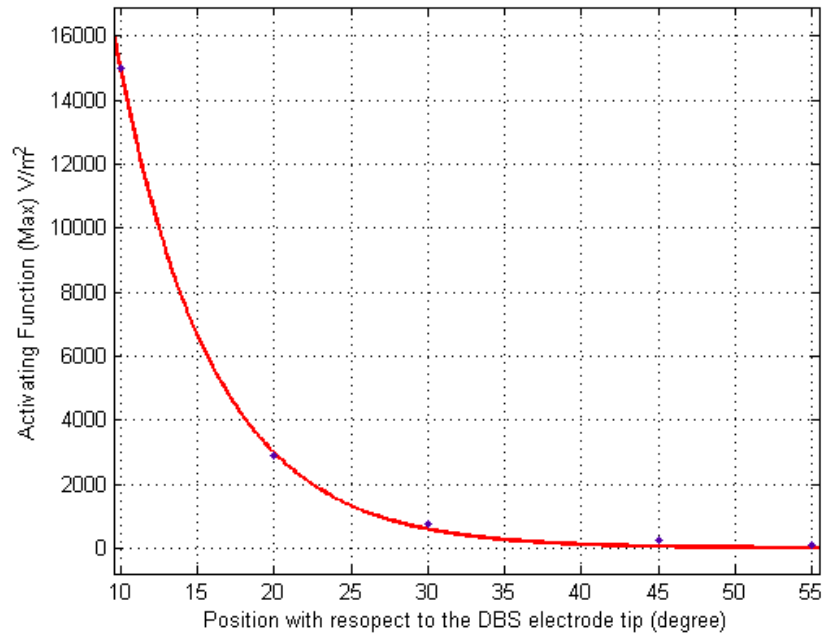


Figure 5-29 Maximum activating function (AF_{max})[V/m^2] for different angles from the electrode shaft

5.5 Effect of Pulse Width

In all previous sections, we have only studied the effect of the DBS pulse amplitude on the maximum activating function. In this section we will vary the width of the DBS pulse from $60\mu s$ - $450\mu s$ in steps of $30\mu s$. For each of these pulse widths, we did vary the DBS pulse amplitude and it was held constant at 1 volt.

The activating function along a vertical line passing 1 mm on the right of the active contact no. 1 was calculated for different DBS pulse widths as shown in Figure 5-30. The maximum values of the activating function are summarized in Table 5-4, and the relation between the maximum values of the activating function at 1mm position from the electrode shaft and different DBS pulse widths are shown in Figure 5-31

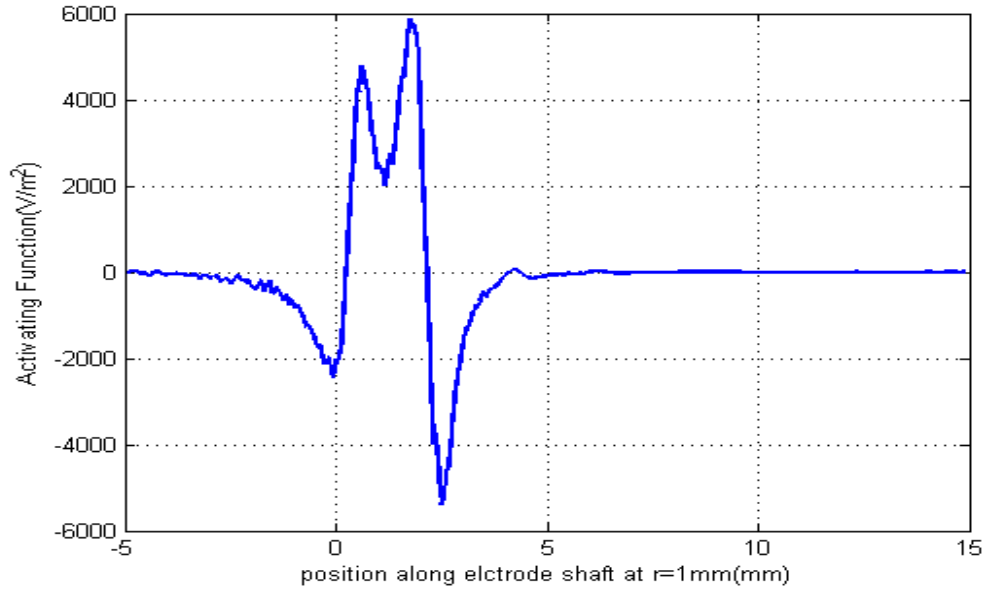


Figure 5-30 Activating function along a vertical line passing 1 mm from DBS active contact No. 1 for DBS pulse width = 90 μ s.

Table 5-4 Maximum activating function (AF) [V/m²] for different DBS pulse widths at 1.0mm from the DBS electrode shaft

DBS Pulse width	AF(Max) V/m ²
60	3.919*10 ³
90	5.870*10 ³
120	7.680*10 ³
150	9.309*10 ³
180	10.580*10 ³
210	11.660*10 ³
240	12.540*10 ³
270	13.220*10 ³
300	13.720*10 ³
330	14.108*10 ³
360	14.497*10 ³
390	15.020*10 ³
420	15.279*10 ³
450	15.542*10 ³

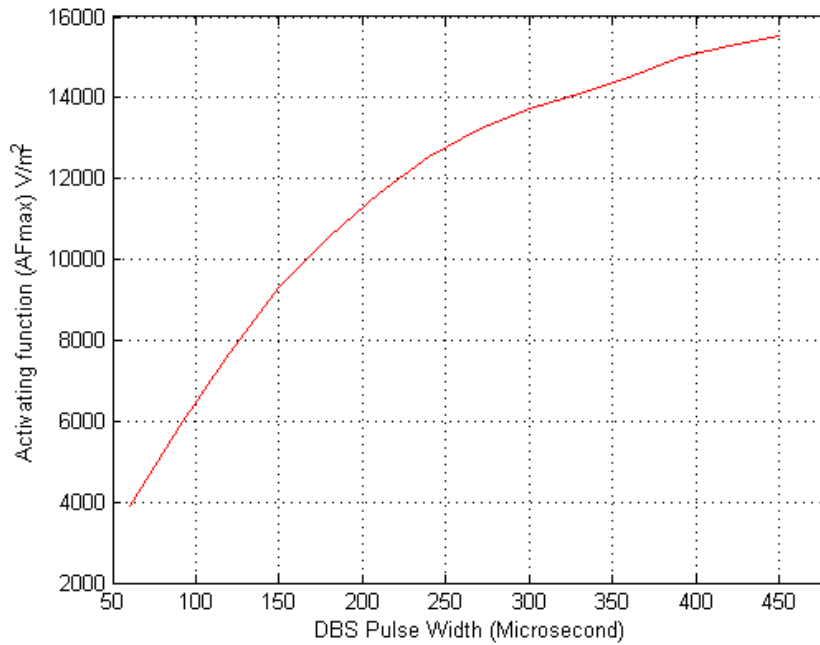


Figure 5-31 Maximum activating function (AF_{max})[V/m²] for different DBS pulse widths (μs)

5.6 Effect of DBS Electrode Encapsulation Thickness

Moreover as we explained earlier, encapsulation layer surrounding the implanted DBS electrode will be added to the basic brain model as discussed in (Model-II, Figure 4-7) which represents the aging process of the implanted electrode inside the brain tissue.

We will study the effect of the DBS electrode encapsulation thickness on the electric field and voltage distribution as well as the behavior of the activating function inside the brain tissue, also, we will calculate the injected current from the electrode contact through the brain tissue in order to determine how the impedance of the DBS electrode contact is changing with the aging process of the DBS electrode. The conductivity of the encapsulation layer was taken at a value of $0.05 \text{ S} \cdot \text{m}^{-1}$ and the brain Grey tissue was kept at $0.1 \text{ S} \cdot \text{m}^{-1}$ while the encapsulation tissue layer permittivity value remains the same as the brain Grey tissue. The thickness varied between 0.1 to 1 mm.

5.6.1 Electric Field Distribution Calculation

The electric field distribution was calculated at two different encapsulation thicknesses of 0.36 mm and 1.0 mm where a negative one volt was applied to the DBS electrode contact. The maximum electric field intensity within the brain tissue was found to be equal to 2.78 KV/m within 3.9 mm penetration depth for 0.36 mm encapsulation thickness as shown in Figure 5-32 which represents a drop of the field intensity and shrinkage of the electric field region from 4.5 mm where there was no encapsulation layer assigned. For the other case of 1.0 mm encapsulation thickness, the field valued dropped to 1.56KV/m within a 3.5mm region inside the brain tissue as shown in Figure 5-33.

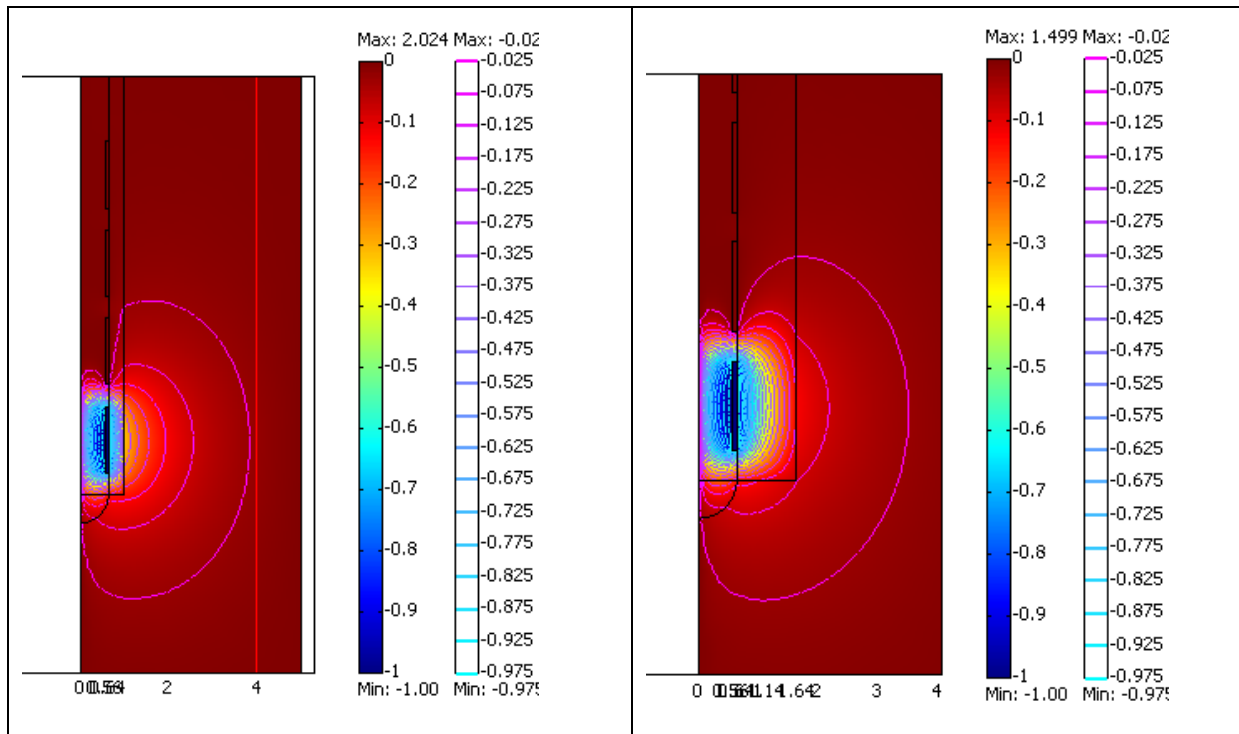


Figure 5-32 Finite element potential contour of DBS electrode surrounded by 0.36 mm encapsulation thickness with conductivity $\sigma=0.05 \text{ S.m}^{-1}$

Figure 5-33 Finite element potential contour of DBS electrode surrounded by 1.0 mm encapsulation thickness with conductivity $\sigma=0.05 \text{ S.m}^{-1}$

5.6.2 Effect of Encapsulation Thickness on Voltage and Activating Function

The electric potential and the activating function was calculated at 2mm distance from the electrode shaft for the case of 1.0 mm encapsulation thickness as shown in Figure 5-34 since this encapsulation layer represents a dead tissue and there is no meaning to calculate the activating function inside it. The maximum value of the electric potential dropped to 0.09 Volt while the activating function dropped to $0.0645 \cdot 10^3 \text{ V/m}^2$ which is approximately 3 times less than the case when no encapsulation thickness inserted.

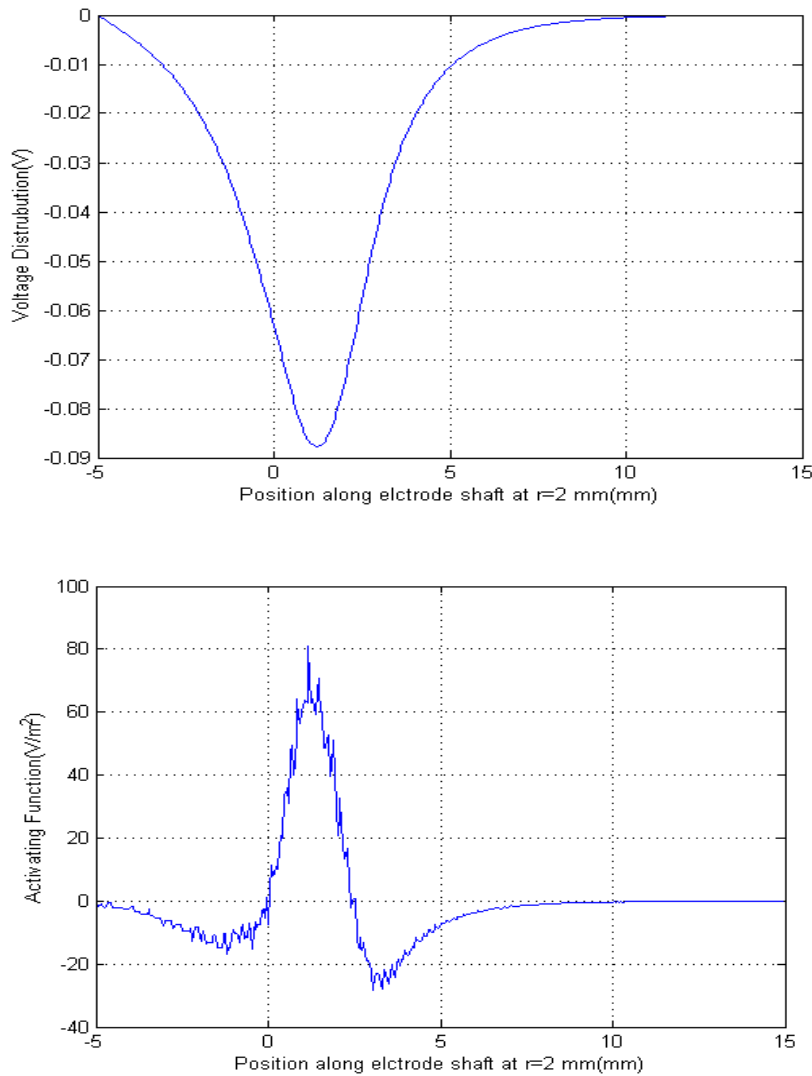


Figure 5-34 Electric potential and activating function at 2 mm from DBS contact for $V = -1$ volt with 1.0 mm encapsulation thickness of conductivity $\sigma = 0.05 \text{ S.m}^{-1}$

5.6.3 Current Density and Impedance Calculation

For the case when a negative 1 volt stimulus applied to the DBS electrode contact, the injected current density through the brain tissue was calculated for different encapsulation thickness ranging from 0-1 mm as shown in Figure 5-35, Figure 5-36 and Figure 5-37. Current density was integrated around the contact surface to determine the current injected into the brain tissue. Ohms law was used to determine the impedance from $Z=V/I$. Encapsulation thickness around the electrode shaft had a strong effect on impedance. Variations in its thickness caused changes of impedance from 220-450 Ω as shown in Figure 5-38. These low values of calculated impedance matched the measured impedance of DBS electrode contacts in *Vitro* done by [76]. Hence, encapsulation around the electrode contact had a strong effect on DBS system impedance.

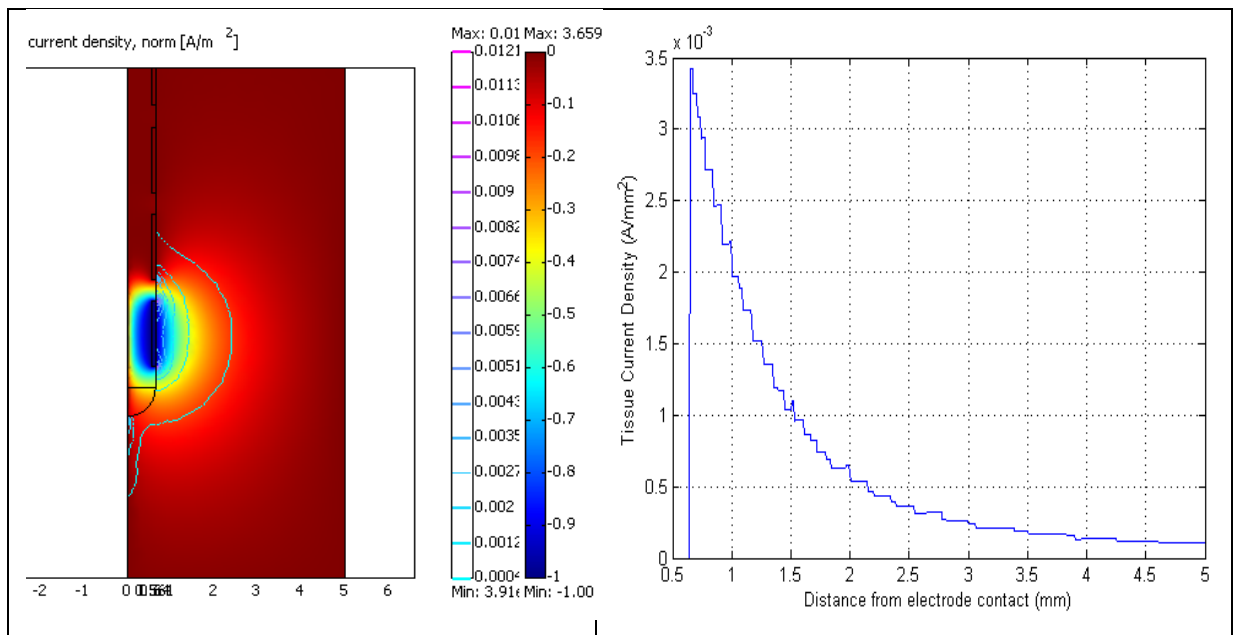


Figure 5-35 Surface current density distribution at DBS contact center with 0 mm encapsulation thickness of conductivity $\sigma=0.05 \text{ S.m}^{-1}$

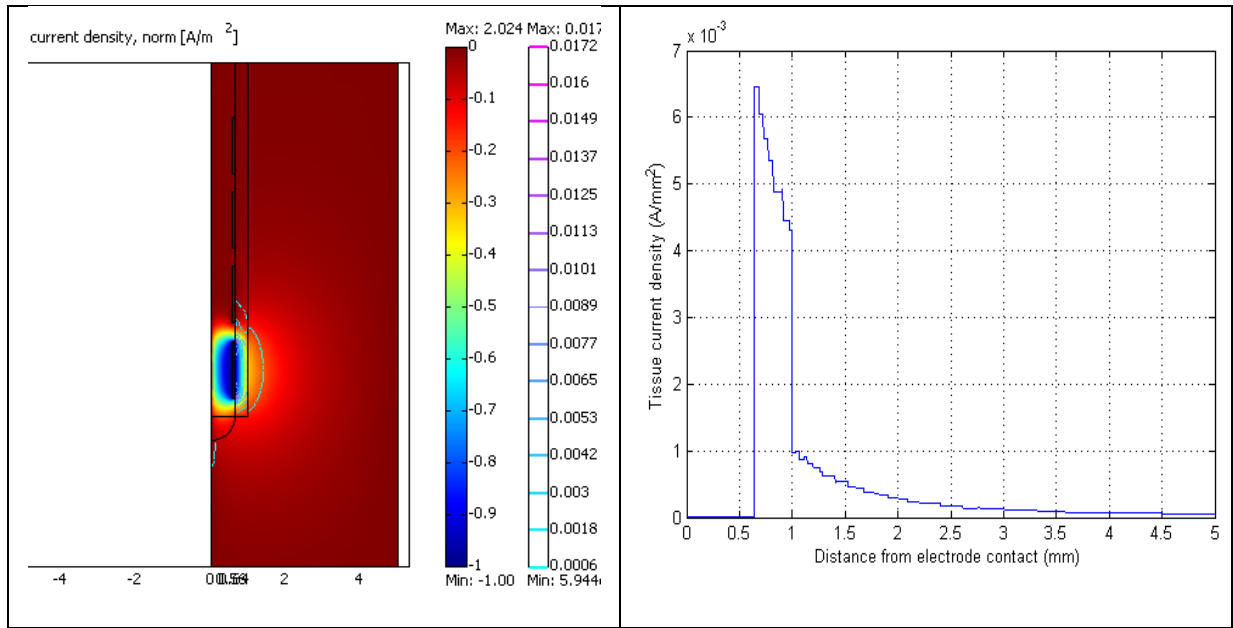


Figure 5-36 Surface current density distribution at DBS contact center with 0.36 mm encapsulation thickness of conductivity $\sigma=0.05 \text{ S.m}^{-1}$

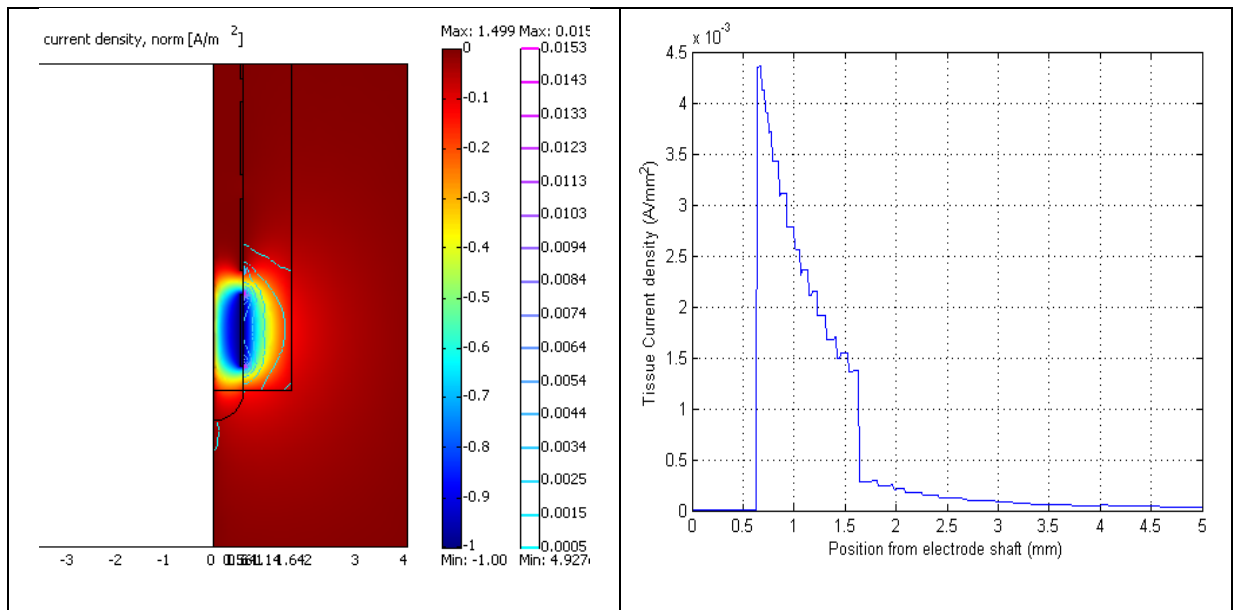


Figure 5-37 Surface current density distribution at DBS contact center with 1.0 mm encapsulation thickness of conductivity $\sigma=0.05 \text{ S.m}^{-1}$

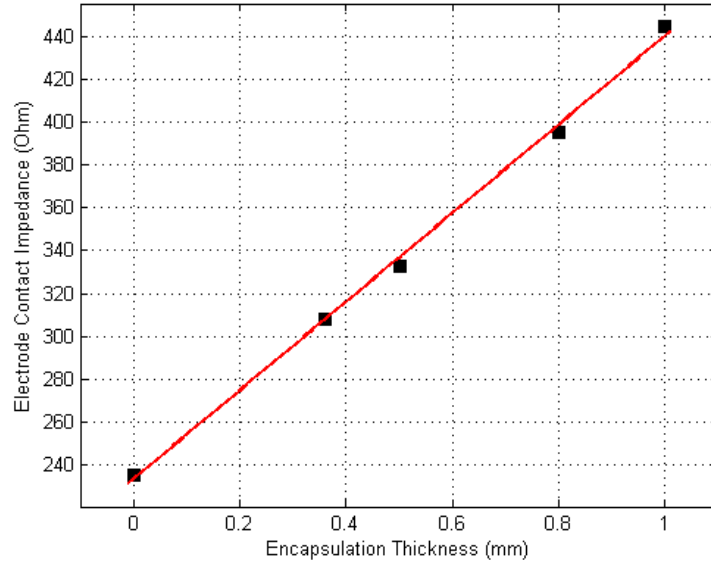


Figure 5-38 DBS electrode contact impedance vs. encapsulation thickness from 0-1 mm

Matlab Linear regression with linear equation provided the most accurate model, with confidence bounds of 95%. The relation between electrode contact impedance and encapsulation thickness is extracted in equation (5.5)

$$Z(T_{\text{encap}}) = 206.8 * T + 233.2 \quad \Omega \quad (5.6)$$

with R – square = 99.8% and RMSE = 4.149

5.7 DBS Electrode in Anisotropic Conductivity Medium

The electric field distribution inside the brain tissue is controlled by the electrical conductivity and permittivity of brain tissue as was discussed before. In all previous models we assumed that the brain tissue is isotropic conductor but in the real case it is anisotropic medium. The effect of this anisotropic conductivity medium on the field distribution and hence the activating function was studied. The values of the conductivities used for the Grey tissue matter was extracted by diffusion tensor MR imaging (DTI) [77].

The DBS electrode was surrounded by anisotropic medium of $\sigma_1 = 0.545 S.m^{-1}$ and $\sigma_2 = 0.435 S.m^{-1}$ in x, y directions respectively. The electric field distributions were calculated as shown in Figure 5-39. It shows a drifting of the major axis of the electric field towards the DBS electrode axis.

The voltage distribution and the activating function were subsequently calculated at 1mm distance from electrode shaft, the results were plotted with respect to the isotropic case as shown in Figure 5-40. It can be shown that there is a slight change in the values of the voltage and the activating function except there is a shifting in the values of both curves due to the new orientation of the electric field around the DBS electrode.

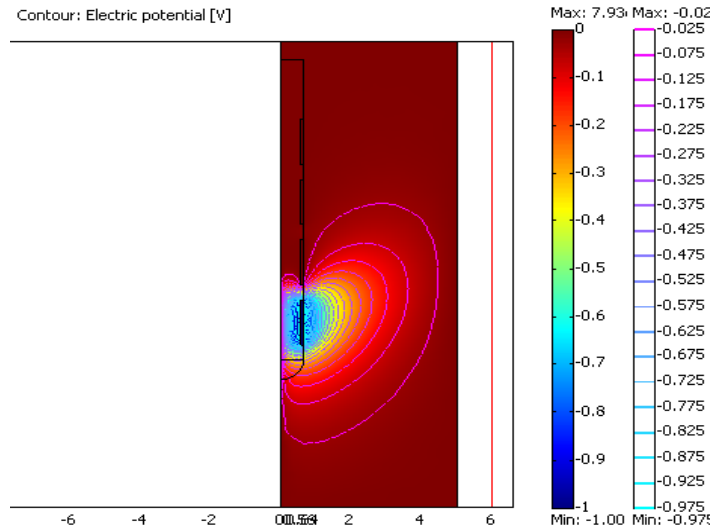


Figure 5-39 Finite element potential contour of DBS electrode surrounded by anisotropic medium of conductivity $\sigma_1 = 0.545 \text{ S.m}^{-1}$ and $\sigma_2 = 0.435 \text{ S.m}^{-1}$ respectively

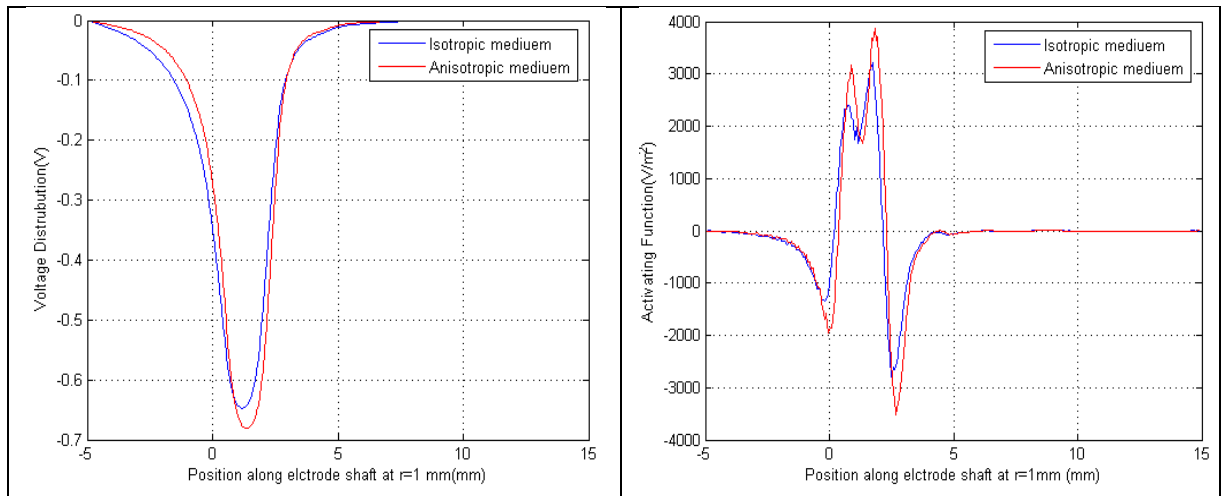


Figure 5-40 Electric potential and activating function at 1 mm from DBS electrode surrounded by anisotropic medium of conductivity $\sigma_1 = 0.545 \text{ S.m}^{-1}$ and $\sigma_2 = 0.435 \text{ S.m}^{-1}$ respectively.

5.8 DBS Electrode Representation versus Point Source Approximation

Calculation of the electrical potentials generated by DBS electrode and subsequently, the activating function calculation will affect the firing neurons and the VTA. All these values depend on the electric field distribution assigned from the geometry of the DBS electrode.

The objective of this section is to quantify the voltage distribution around the DBS electrode contact at different degree angles in order to prove that the DBS electrode contact (which is the source of the electric field) cannot be approximated as a point source as provided by [78]. This approximation will be less accurate in the electric field calculation and this will greatly affect the accuracy of calculating the activating function around the DBS electrode.

The electric potential was calculated along a multiple axis with different degree angles at 10 and 55 degrees respectively. These electric potentials were quantified using Matlab Linear regression technique. The extracted model equations that provided the most accurate model with a minimum root mean square error (RMSE) and maximum coefficient of determination R^2 , with confidence bounds of 95% are shown in Figure 5-41 and Figure 5-42. The behavior of this voltage distribution was observed as a linear combination of Gaussian pulses which is different from the voltage distribution of any point source.

Also, we approximate the voltage distribution located at a 90 degree angle from the real DBS contact as shown in Figure 5-43 and from a point source as shown in Figure 5-44. We determined that maximum coefficient of determination $R^2 = 95.32\%$ in the case of a point source approximation which is 4.52% less accurate than the real DBS contact representation. Hence, approximation of the DBS electrode contact as a point source is not an accurate one.

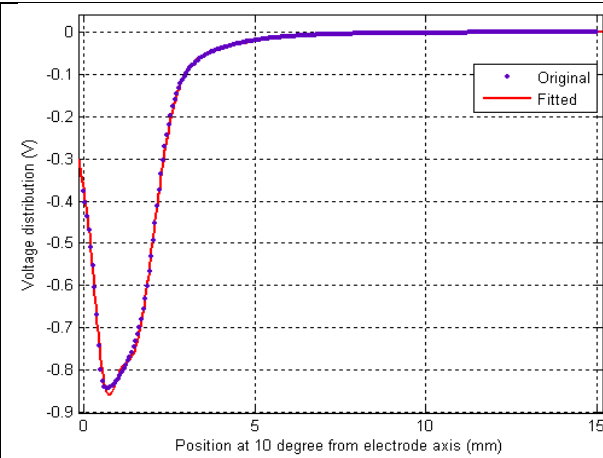


Figure 5-41 DBS voltage distribution at 10 degree

Extract equation is Gauss4:

$$V(x) = -0.1207 \cdot \exp\left(-\frac{(x-0.04483)}{3.801}\right)^2 - 0.3112 \cdot \exp\left(-\frac{(x-0.6302)}{0.4168}\right)^2 + 0.5734 \cdot \exp\left(-\frac{(x-0.8523)}{0.7742}\right)^2 - 1.119 \cdot \exp\left(-\frac{(x-1.061)}{1.025}\right)^2 \quad (5.6)$$

R-square = 99.96% and RMSE = 0.00495

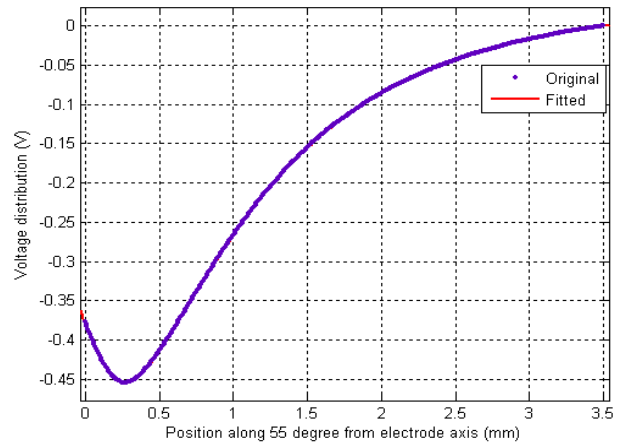


Figure 5-42 DBS voltage distribution at 55 degree

Extract equation is Gauss6:

$$V(x) = 0.01722 \cdot \exp\left(-\frac{(x-4.2)}{0.5929}\right)^2 - 0.3153 \cdot \exp\left(-\frac{(x-0.3074)}{1.37}\right)^2 + -0.01721 \cdot \exp\left(-\frac{(x-0.8574)}{0.3215}\right)^2 - 0.1222 \cdot \exp\left(-\frac{(x-0.3139)}{0.4085}\right)^2 + -0.02021 \cdot \exp\left(-\frac{(x-2.332)}{0.8256}\right)^2 - 0.02236 \cdot \exp\left(-\frac{(x-0.1748)}{0.1893}\right)^2 \quad (5.7)$$

R-square = 99.99% and RMSE = 0.0003547

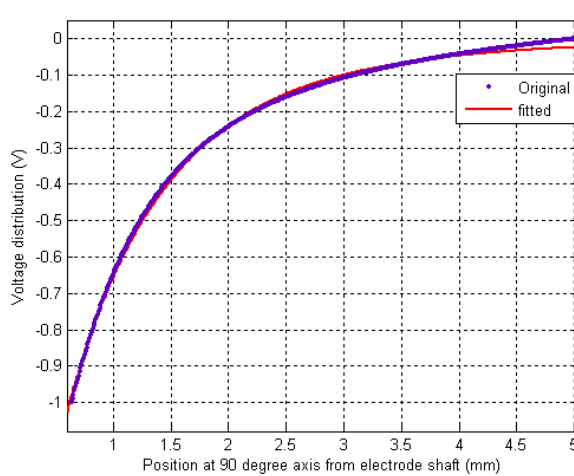


Figure 5-43 DBS voltage distribution at 90 degree

Extract equation is Exp2:

$$V(x) = -1.603 \cdot \exp(-1.384 \cdot x) - 0.4697 \cdot \exp(-0.6153 \cdot x) \quad (5.8)$$

R-square = 99.84% and RMSE = 0.009474

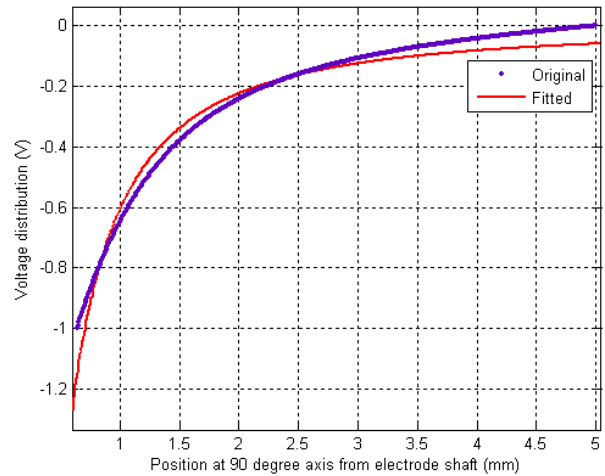


Figure 5-44 Point source approximation

Extract equation is Power1:

$$V(x) = -0.6045 \cdot x^{-1.438} \quad (5.9)$$

R-square = 95.32% and RMSE = 0.03878

5.9 Conclusion

The objective of the analysis in this chapter is to calculate the second order spatial voltage distribution (Activating Function) for an implanted DBS electrode which is needed to be coupled with the neuron cells inside the brain. Finite Element Method (FEM) was used for modeling and simulating the DBS electrode and brain tissue medium. Low frequency models representing the Medtronic 3387 DBS electrode in the STN are developed in this chapter based on Gabriel biological tissue model.

The roles of the DBS stimulation parameters (Pulse width and amplitude) have been studied and their role in affecting activating function is demonstrated. AF_{max} , and AF_{min} have been considered for different voltage values of the input waveform and the maximum electric field intensity within the brain tissue and its penetration depth have been studied. In the case of changing stimulation pulse amplitude, the values confirms with the result obtained before by FDTD analysis in part one; the pulse amplitude had no effect on the depth of field penetration within the tissue while it directly controlled the levels of the field intensity.

Also, the activating function was studied for different distances from the DBS electrode shaft since it will be the input signal to stimulus the neurons placed at these different positions. This activating function will affect the action potential initiation and hence the volume of tissue activated (VTA) with respect to the applied stimulation parameters (The results of this study will be discussed in the next chapter). In order to calculate the value of the activating function at any position, we must integrate the electric field distribution along parallel and perpendicular axis to the DBS electrode. The integration of the electric field along any perpendicular axis to the DBS electrode will only result in small negative values of activating function with respect to the values obtained from the integration along parallel axis to the electrode as shown from Figure 5-13 and Figure 5-28 respectively. From these figures we can observed that the activating function value at 1.0 mm from the center of the first active contact is equal to $+2000 \text{ V/m}^2$ from parallel calculation (Figure 5-13) and -80 V/m^2 from perpendicular calculation which is 25 times less (Figure 5-28). Thus, the total activating function value at this position is equal to 1920 V/m^2 and can be approximated to the value of the activating function (2000 V/m^2) calculated from parallel position manner with a $\sim 4\%$ less accurate. We can conclude that only parallel calculation

of AF with respect to the DBS electrode will be considered in the calculation of the neuron firing activity and the VTA as will be discussed in the next chapter.

The effect of the DBS electrode encapsulation thickness on the electric field and the behavior of the activating function inside the brain tissue have been studied. We showed that the maximum activating function values dropped 3 times less than the case when no encapsulation thickness inserted. Also, we calculated the injected current from the electrode contact and determined the impedance of the DBS electrode contact and how the encapsulation thickness around the electrode contacts increased the DBS system impedance.

Finally, we took into consideration for the region surrounding the DBS electrode the anisotropic brain medium characteristics rather than the simple isotropic medium. The integration of the electric field and the activating function were calculated and the results show a minor change on the values of the activating function except for the shifting due to the new orientation of the electric field around the DBS electrode.

Chapter 6

Deep Brain Stimulation Neuron Simulations and Modeling

6.1 Introduction

In this chapter, we are going to study the last phase for the proposed DBS model as described in section 3.1, Figure 3-2. The interaction between the activating function calculated inside the brain medium tissue due to the implanted DBS electrode and the neuron cells will be analyzed. As mentioned before, The output of this DBS model will represent the region in the brain that is excited through the numbers of neuron that are activated and the firing activity of the neurons which will be used to build the neuron tuning curves and finally the volume of tissue activated (VTA) as shown in Figure 6-1.

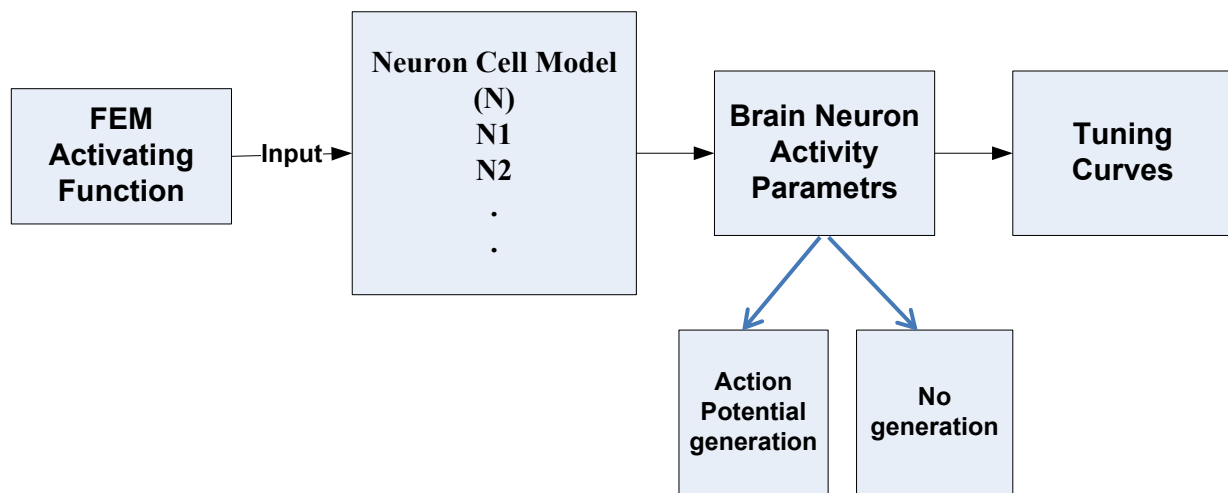


Figure 6-1 A schematic diagram of the inputs and outputs of the neuron environment indicating the coupling between the activating function calculated from FEM model and neuron environment tool to detect neuron firing activity

Finite element electric field and activating functions that have been calculated in the previous chapter will be coupled to the neuron structure in this chapter. The brain medium will be an active source by taking the effect of the neurons inside the STN. In order to build all the details of the neuron structure; dendrite, soma and its axon, we use of the NEURON program in our simulation. NEURON is a simulation environment for modeling individual neurons and networks of neurons [46]. NEURON models individual neurons via the use of sections which are

subdivided into individual compartments by the program; it is used as the basis for instruction in computational neuroscience in many papers.

6.2 STN Neuron Cell Model

Neural excitation by the activating function was calculated for one STN neuron cell as a start to get used to the NEURON program. To build this neuron model, a multi-compartment cable model of a STN neuron was used as discussed in chapter 2. It consisted of soma and multi-compartment myelinated axon with explicit representation of the myelin and underlying axolemma. All the parameters related to this neuron cell model were shown in Figure 2-23, Table 2-7 and Table 2-8.

A short axon cable model of a $5.7 \mu\text{m}$ diameter myelinated axon was implemented in NEURON to quantify the response of this cell to extracellular spatial voltage distribution. The model consisted of 4 nodes of Ranvier separated by 3 internodes. Each internode section of the model consisted of 2 paranodal myelin attachment segments (MYSA), 2 paranodal main segments (FLUT), and 6 internodal segments (STIN) regions of fiber as shown in Figure 2-22. The Model Geometric Parameters with this $5.7 \mu\text{m}$ fiber diameter is listed in Table 2-5.

Each node of Ranvier was modeled as a single electrical compartment connected to other nodes via a series resistance and to the extracellular medium by a parallel circuit consisting of a voltage-gated sodium channel, a linear leakage conductance and a membrane capacitance. Internodal lengths were $500 \mu\text{m}$ which is about 88 times the axon diameter, and the diameter of the node of Ranvier was $1.9 \mu\text{m}$ which is 0.3 times the axon diameter.

The position of the neuron with respect to the electrode shaft was set into two different scenarios; all of the scenarios were set at 1mm apart from the electrode shaft with the first position set into the middle of the DBS electrode first active contact. In the second position the neuron was set into the middle of the DBS second non active contact as shown in Figure 6-2. A stimulus pulse with negative one volt was applied to the first contact, and the others contacts are set to zero voltage. The activating function along a line passing 1 mm apart from the electrode shaft were calculated as shown in the previous chapter and coupled to the neuron program. Simulations were conducted to measure neuron's action potential.

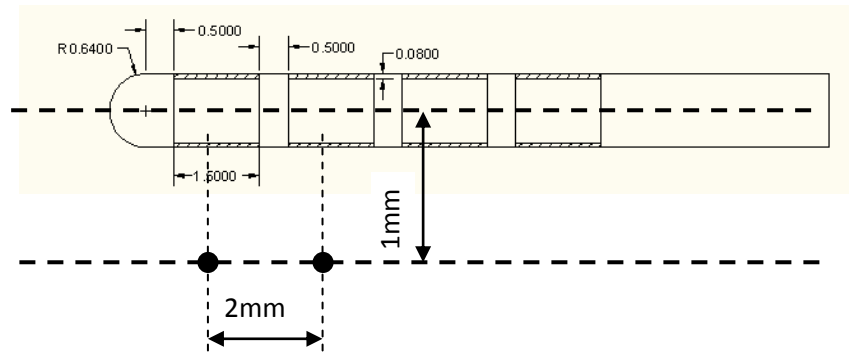


Figure 6-2 Position of the electrode with respect to the neuron for two different scenarios 1 and 2

In the first scenario, the neuron is set into a high positive activating function and hence it will lead to a higher probability of depolarization. It can be shown that the activating function due to stimulation of -1 volt at the first active contact triggers a spike that propagates actively along the axon as shown in Figure 6-3.

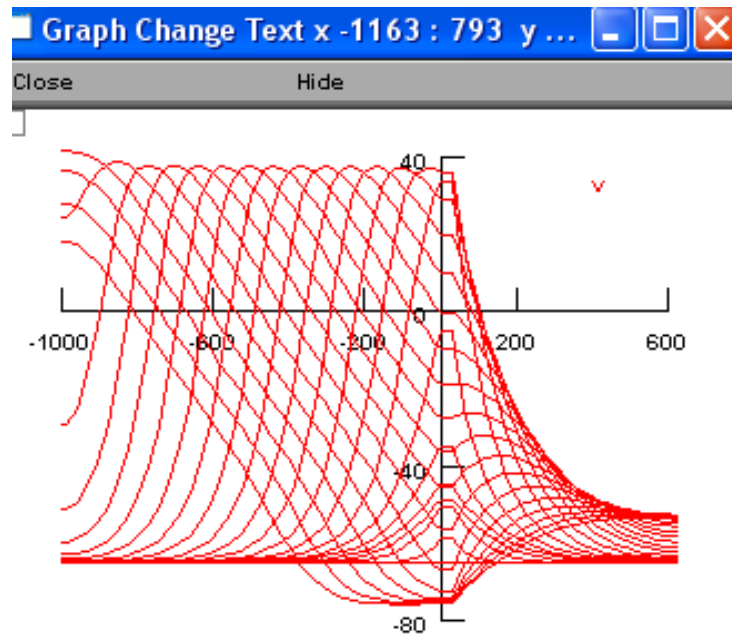


Figure 6-3 Propagation of action potential along the axon

In the second scenario the neuron is placed into the middle of the non-active DBS contact and a negative activating function is calculated. This lead to hyperpolarization and no action potential or spikes were triggered as shown in Figure 6-4. This verified that the coupling between the calculated activating function and the generation or no generation of the action potential was successfully integrated. This allowed us to investigate the effect of the DBS stimulation parameters on neuron firing activity (spikes/second) and the volume of tissue activated can be readily investigated.

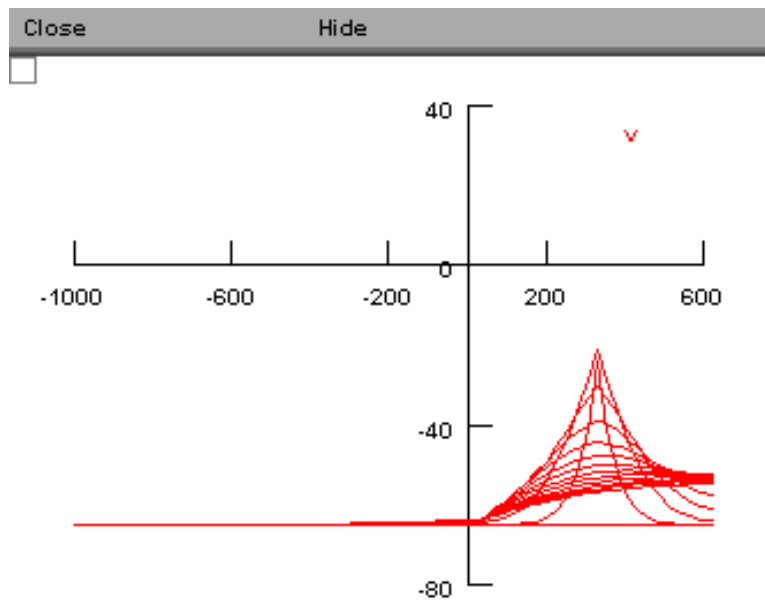


Figure 6-4 Action Potential cannot be triggered due to hyperpolarization effect

To study the effect of the DBS pulse amplitude voltage on the firing activity of the neuron, the STN neuron cell was placed in the middle of the DBS electrode first contact at a distance 1 mm from the electrode shaft as was done before in the first scenario. The pulse amplitude was set for a value of -0.5 volt and the activating function was calculated at this position. The AF was coupled to the NEURON program and the firing activity at this position was recorded as shown in Figure 6-5.

A time window of $T = 500\text{ms}$ is set and the number of spikes $n_{sp}(T)$ that occur in this interval is counted. The mean firing rate which is equal to: $a = n_{sp}(T)/T$ is calculated for this specific voltage and is found to be 60 spikes/second.

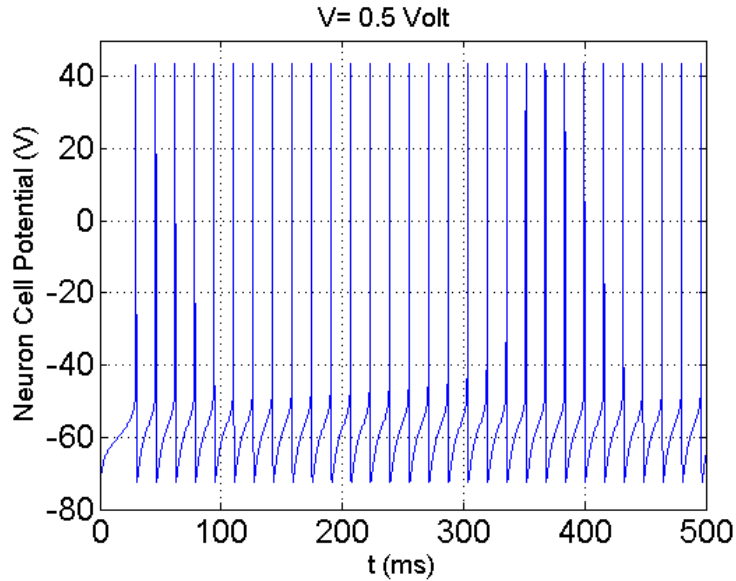


Figure 6-5 Firing activity rate (spikes/second) for DBS electrode stimulation amplitude voltage of -0.5 volt

The scenario was repeated for a negative 2 voltage. The firing rate was recorded from the neuron as shown in Figure 6-6. This represents 146 spikes/second. It can be deduced that higher stimulation voltage (-2) will lead to higher firing activity rate (spikes/second) while negative 0.5 volt will cause smaller amount of activity.

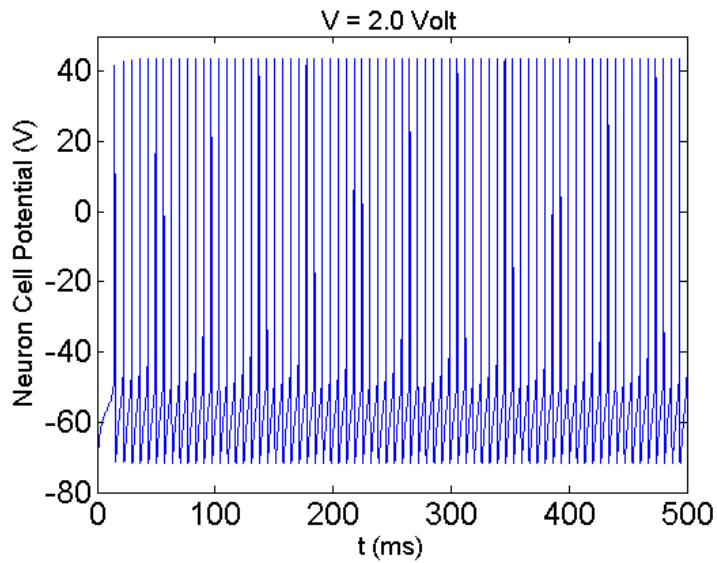


Figure 6-6 Firing activity rate (spikes/second) for DBS electrode stimulation amplitude voltage of -2.0 volt

6.3 DBS STN Tuning Curves

In this section we are going to build the tuning curves for neurons; they are a family of curves that describe the relation between neurons firing activity and the parameters under study for which we want to investigate its effect on the neurons, i.e., we can study the effect of DBS pulse parameters (Amplitude, width and frequency) on the neurons firing rates. We started with a population of two neurons ($N=2$) located at 1.0 mm and 1.50 mm apart from the electrode shaft and centered into the middle of the DBS electrode first active contact as shown in Figure 6-7. The DBS pulse amplitude varied from 0 - 3 volts in steps of 0.25 volt and for each voltage, the system was solved and the activating function was calculated and coupled to the STN cell model using the NEURON program. The firing activity from each neuron was recorded, calculated and tuning curves were constructed for those two neurons as shown in Figure 6-8.

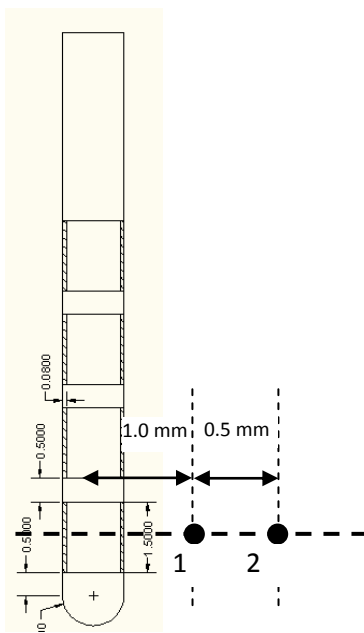


Figure 6-7 Position of the electrode with respect to two neurons ($N=2$)

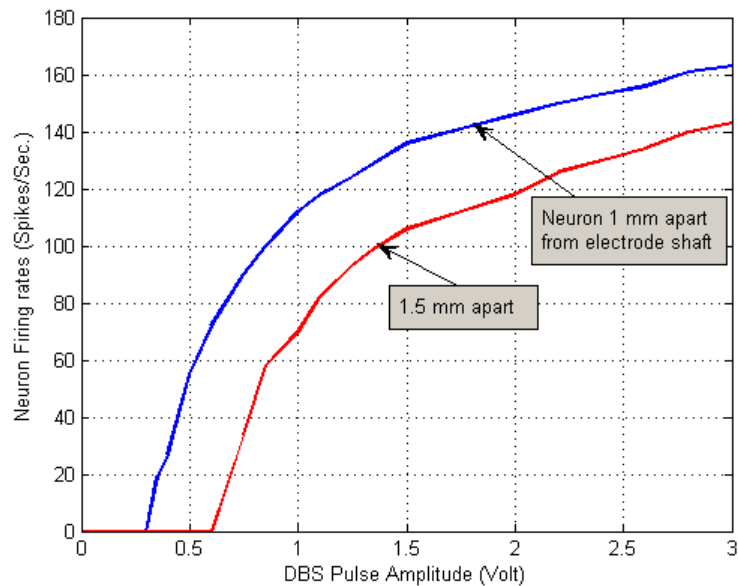


Figure 6-8 Tuning curves for two neurons ($N=2$) located at 1.0 mm and 1.5 mm from electrode shaft at the center of the first DBS electrode contact

6.4 Neurons Firing Decoding

Back to the proposed DBS model in Figure 3-2, since we need to use some sort of superposition to study the DBS interaction with brain neurons as discussed before. We have implemented optimal linear decoder filter to find the accurate decoding of neural firing activity representing the input DBS parameters. This optimal linear decoder represent last block in our DBS model implementation as shown in Figure 6-9 .

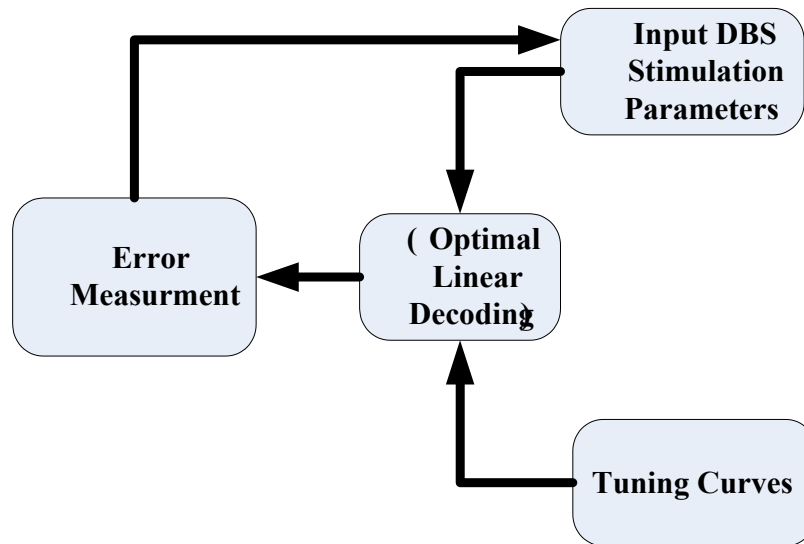


Figure 6-9 A schematic diagram of the inputs and outputs of the optimal linear decoder filter

The input of the optimal linear decoder depends on the neurons tuning curves in a way that we need to build this tuning curves in order to calculate the matrix A which was given by equation (3.9). This matrix dimension depends on the number of neurons used to build the tuning curves. Figure 6-10, Figure 6-11, Figure 6-12, Figure 6-13 and Figure 6-14 Show the tuning curves for different neuron populations (N=10 to N=50).

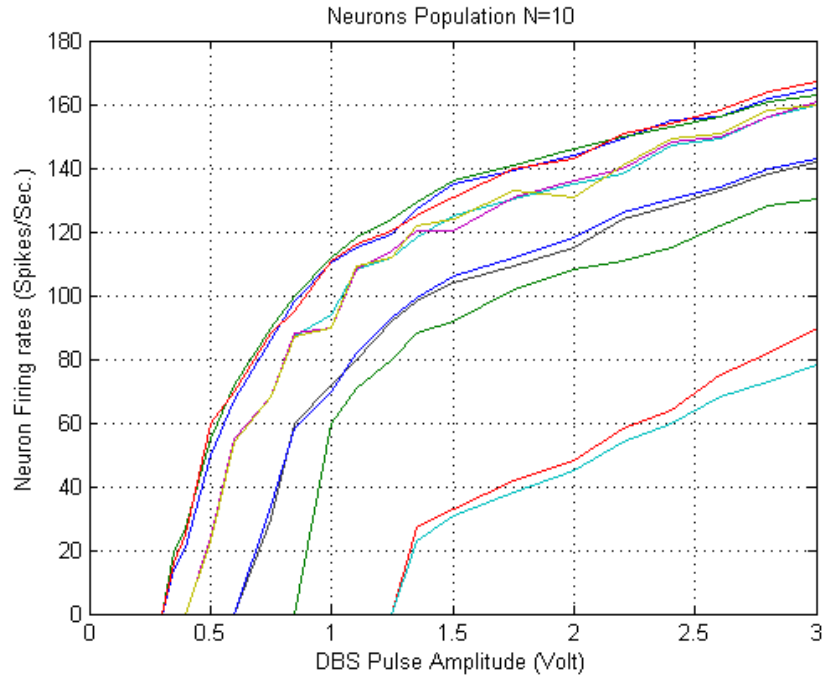


Figure 6-10 Tuning curves for neuron population (N=10) oriented perpendicular to the electrode shaft with 0.25mm inter distance

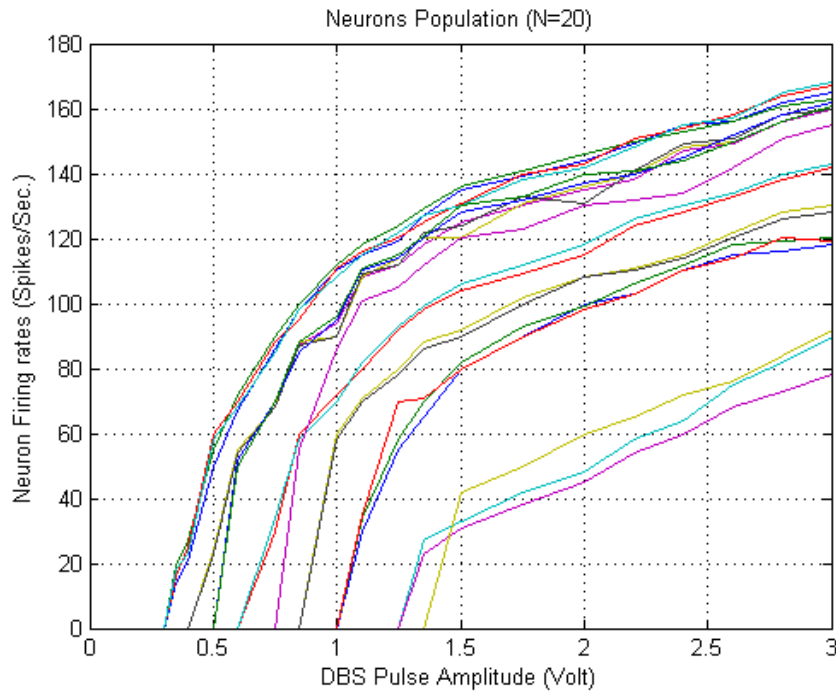


Figure 6-11 Tuning curves for neuron population (N=20) oriented perpendicular to the electrode shaft with 0.25mm inter distance

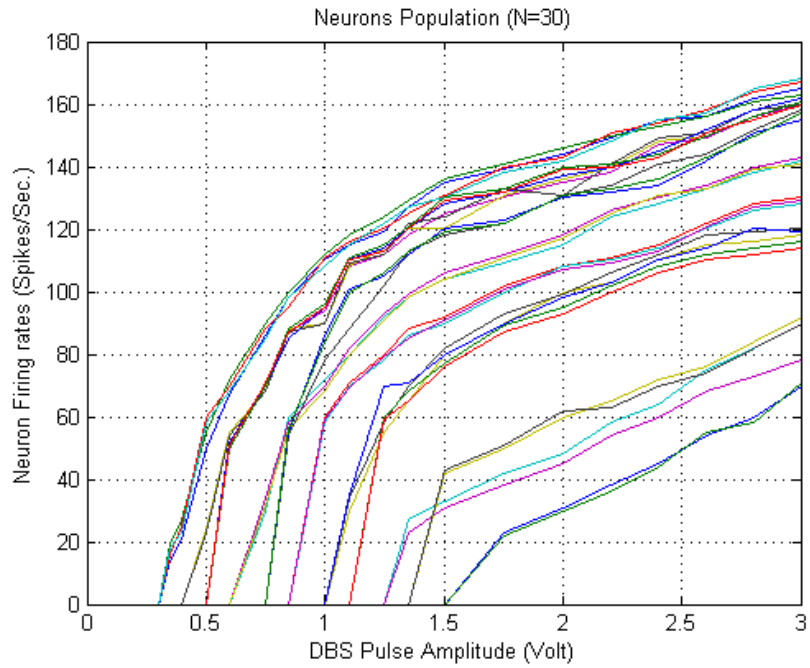


Figure 6-12 Tuning curves for neuron population (N=30) oriented perpendicular to the electrode shaft with 0.25mm inter distance

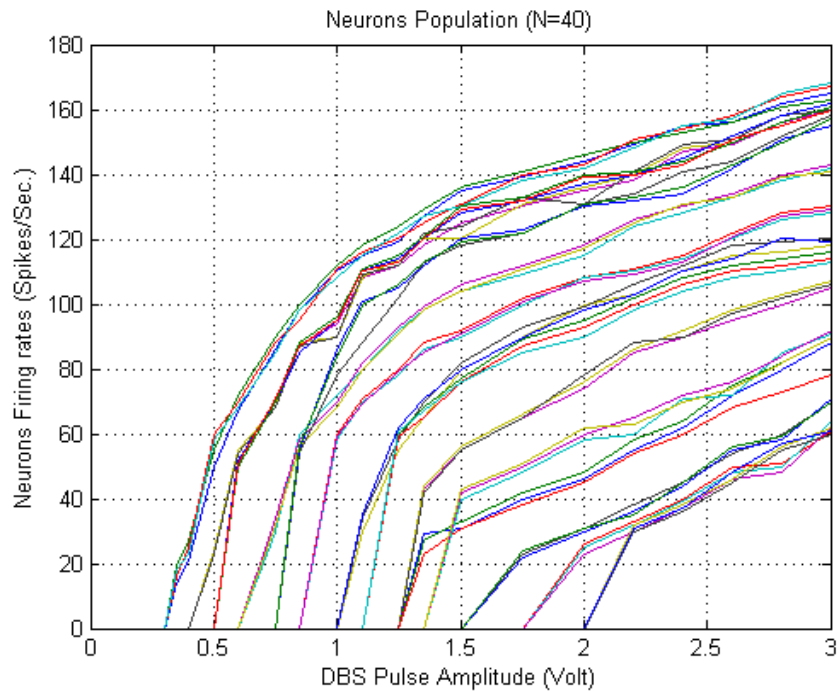


Figure 6-13 Tuning curves for neuron population (N=40) oriented perpendicular to the electrode shaft with 0.25mm inter distance

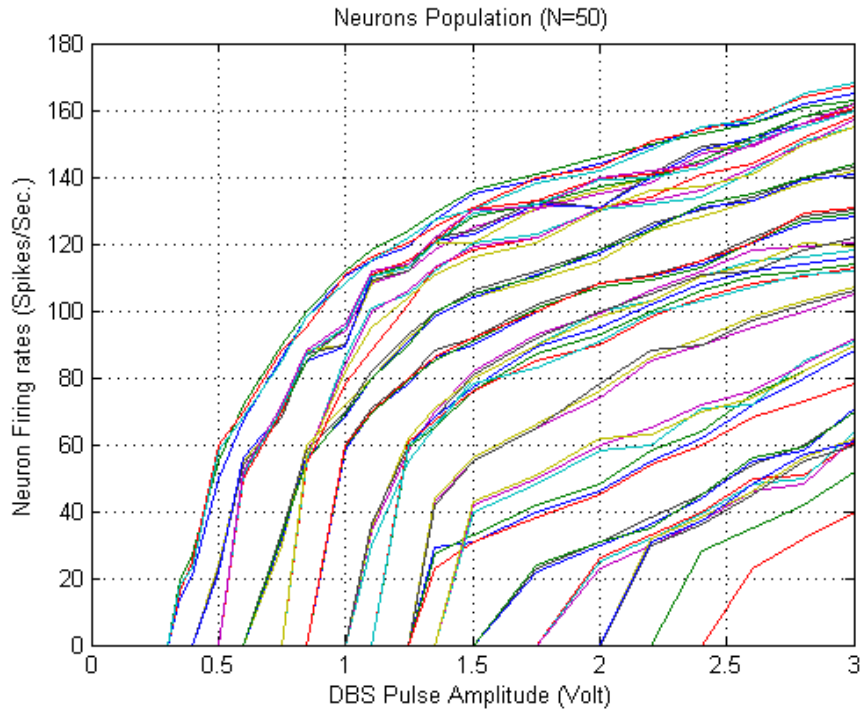


Figure 6-14 Tuning curves for neuron population (N=50) oriented perpendicular to the electrode shaft with 0.25mm inter distance

The tuning curves are discretized by an interval of $\Delta x=0.1$ volt to build this matrix, the linear filter coefficients (φ) were calculated according to equation (3.11) in such a way to minimize the error between the applied DBS pulse amplitude and the reconstructed pulse amplitude. The values of the optimal linear filter coefficients for the case when the number of the neurons $N=10$ are shown in Figure 6-15. The decoded pulse amplitude was applied back to the DBS electrode and hence all of the previous calculations of the electric field distribution, the activating function and then the firing activity were recalculated to build a new tuning curves and the matrix A until the difference between the effect of applied DBS parameters and the reconstructed ones were negligible. This step guaranteed that electric field distribution that comes from the applied pulse on the DBS electrode matches with the electric field distributions (electric charge) from the neurons inside the brain. The reconstructed DBS pulse amplitude versus the applied input DBS pulse amplitude for the case when $N=10$ are shown in Figure 6-16.

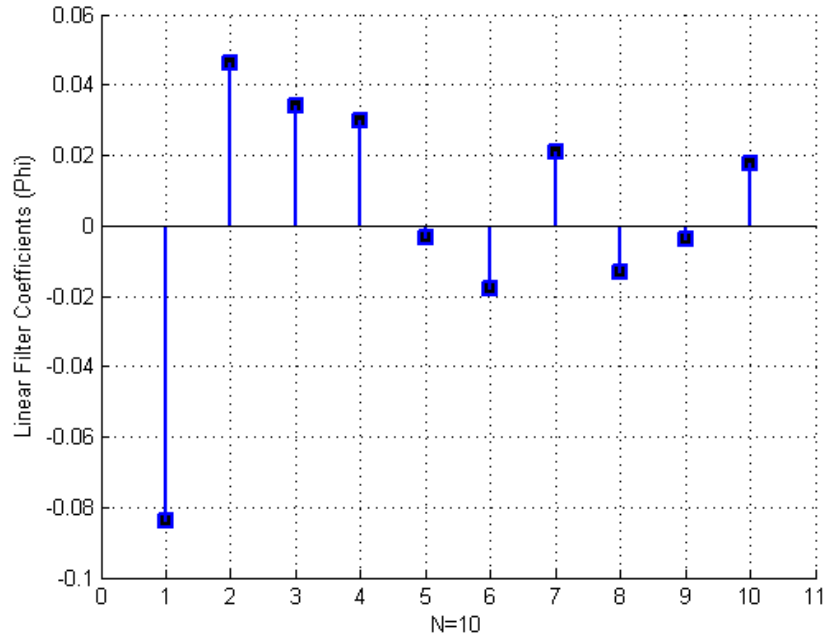


Figure 6-15 Optimal linear filter coefficients for N=10

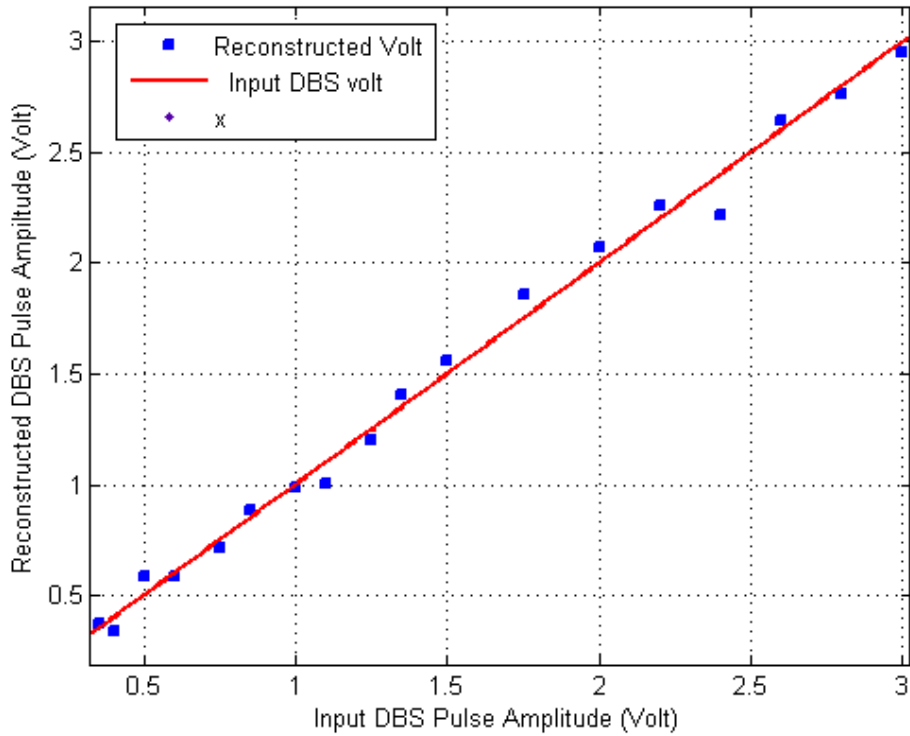


Figure 6-16 Reconstructed DBS pulse amplitude versus applied input DBS pulse amplitude

The Optimal linear filter coefficients were calculated for the other cases when the number of neurons used was equal to $N=20$, 30, 40 and 50 respectively, the values of these decoder coefficients are plotted in Figure 6-17, Figure 6-18, Figure 6-19 and Figure 6-20.

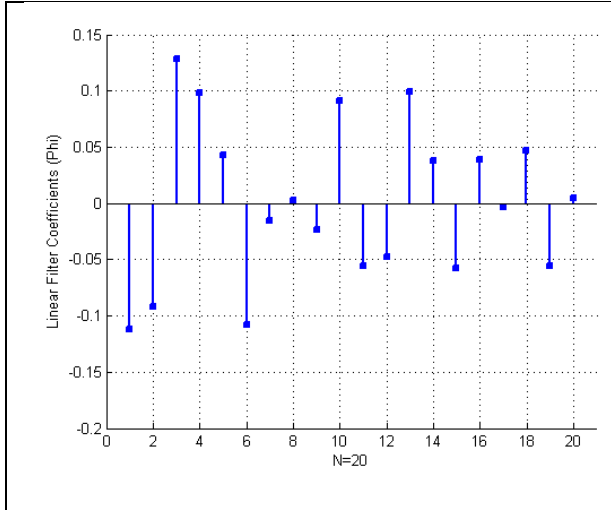


Figure 6-17 Optimal linear filter coefficients for $N=20$

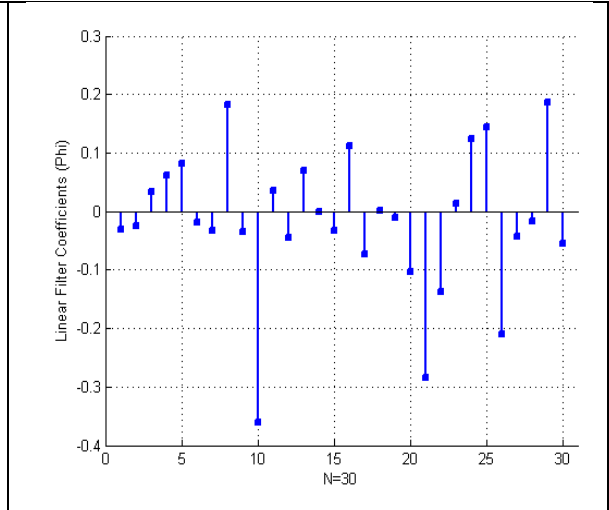


Figure 6-18 Optimal linear filter coefficients for $N=30$

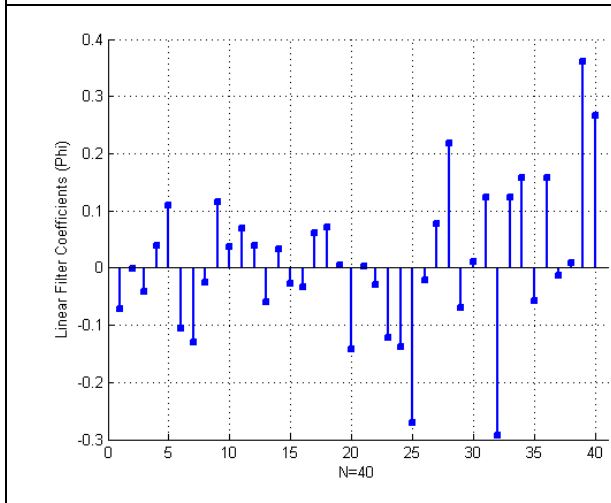


Figure 6-19 Optimal linear filter coefficients for $N=40$

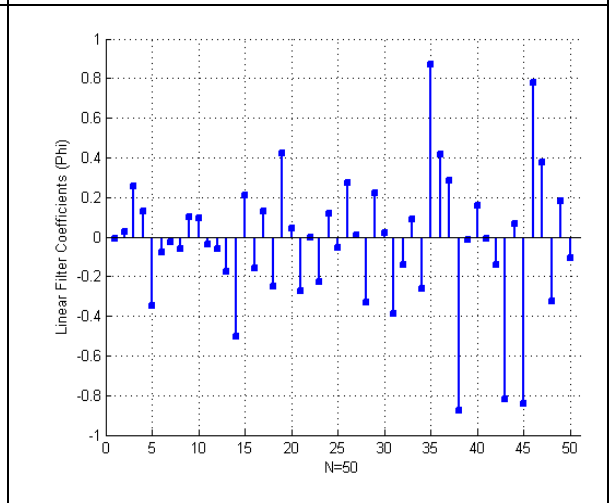


Figure 6-20 Optimal linear filter coefficients for $N=50$

The Optimal linear decoder's minimum errors versus neuron populations are shown in Figure 6-21, and it was found that this error is proportional to the number of neurons used through the extracted equation:

$$\text{Mean Square Error} \cong 1/N^2 \quad (6.1)$$

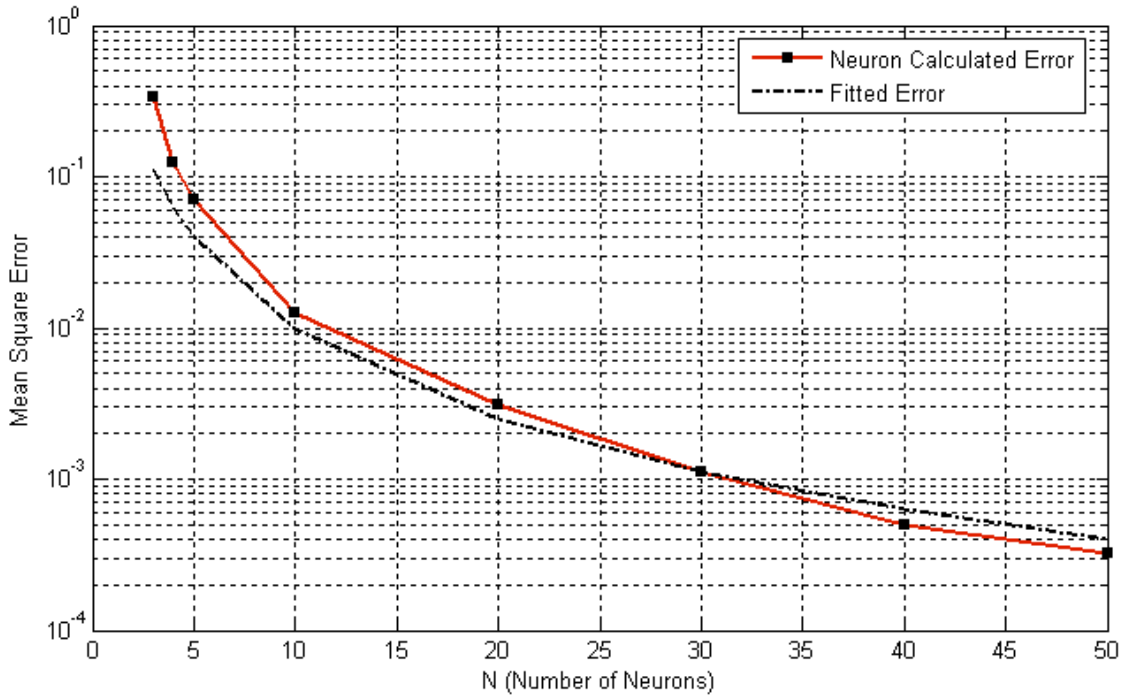


Figure 6-21 Mean square error versus number of neurons (N) used to build tuning curves

This last step guaranteed the complete developing of our DBS model which was proposed in chapter 3, and it the first time, to the best of the author knowledge; we are able to build family of tuning curves for STN regions versus the effect of the stimulation pulse amplitude. This type of information is very important to the physician to determine the activity of the neurons and hence the volume of tissue activated due to different DBS pulse amplitude.

6.5 Volume of Tissue Activated (VTA) of Neurons

In this section we develop a quantitative technique to estimate the VTA (the numbers of neurons that is being active within the brain tissue) as a function of DBS pulse amplitude. DBS electrode was coupled to a collection of 225 STN neurons which were distributed in a 15 ×15 matrix oriented perpendicular to the electrode shaft with 0.25mm inter distance. A 5.7 μm diameter myelinated axon models were used as previously explained in section 2.16. The DBS pulse amplitude was changed at -0.5V, -1V, -2V and -3 respectively with a constant width of 60μs and

a frequency of 130Hz. The electric field distribution generated in the tissue medium from the FEM solution was calculated, the activating function was introduced onto the position of each neuron, and the time dependent transmembrane potential variations induced by the stimulation were calculated in NEURON program. Red spheres indicate positions of neurons that were fired and hence VTA can be estimated for the different DBS pulse amplitude used as shown in Figure 6-22, Figure 6-23, Figure 6-24 and Figure 6-25 respectively. It also shows the positions of the activated neurons with the respect to the electric potential intensities and contours generated inside the brain tissue.

The resulting volumes of the tissue activated (VTA) produced by the Medtronic DBS electrode are listed in Table 6-1. It can be seen that VTA was $\sim 1.25\text{mm}$ radius with a volume of 8.18 mm^3 using stimulation voltage of -0.5 V while it increased to ~ 27 times (220.89 mm^3) when using a -3.0 V stimulating voltage as shown in Figure 6-26. From those values of VTA (activated neurons around the DBS electrode at many distances apart from the electrode shaft), we can conclude that the threshold for activation is $\sim 200.0\text{ V/m}^2$ inside brain tissue.

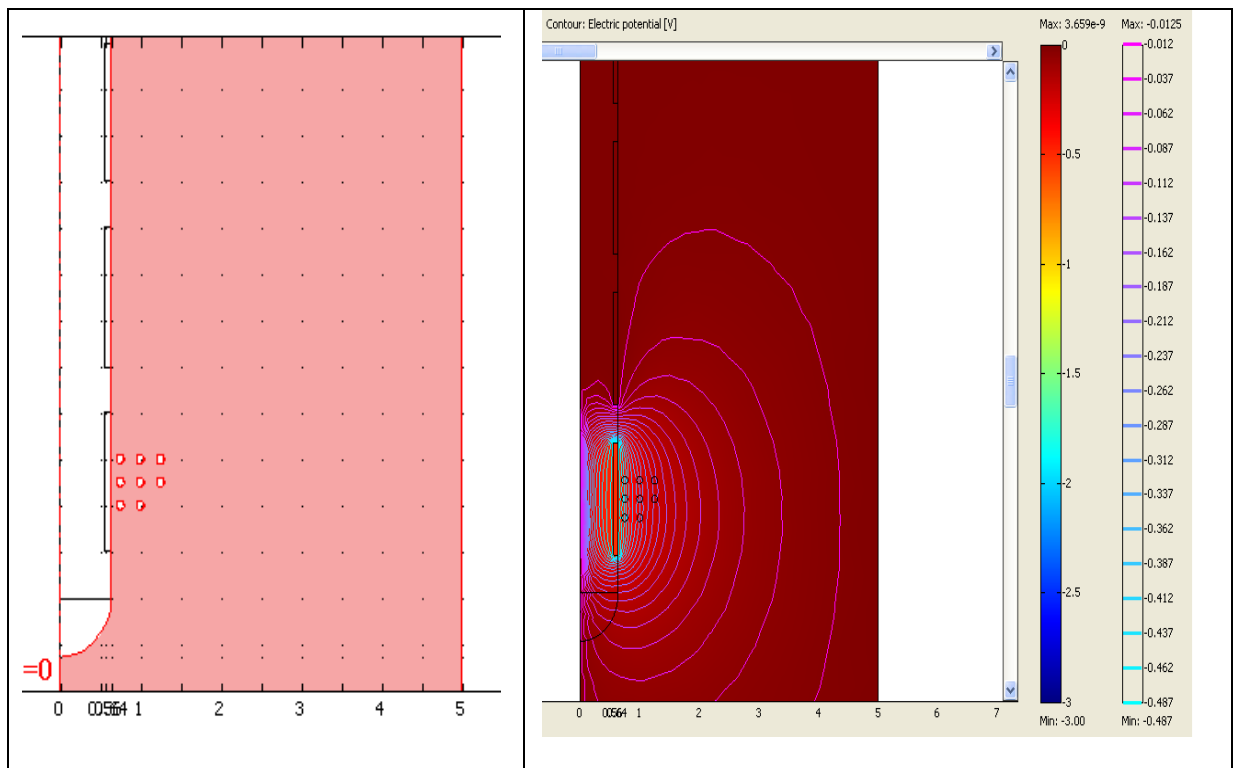


Figure 6-22 Prediction of neuron model activation for pulse amplitude $V = -0.5$ Volt

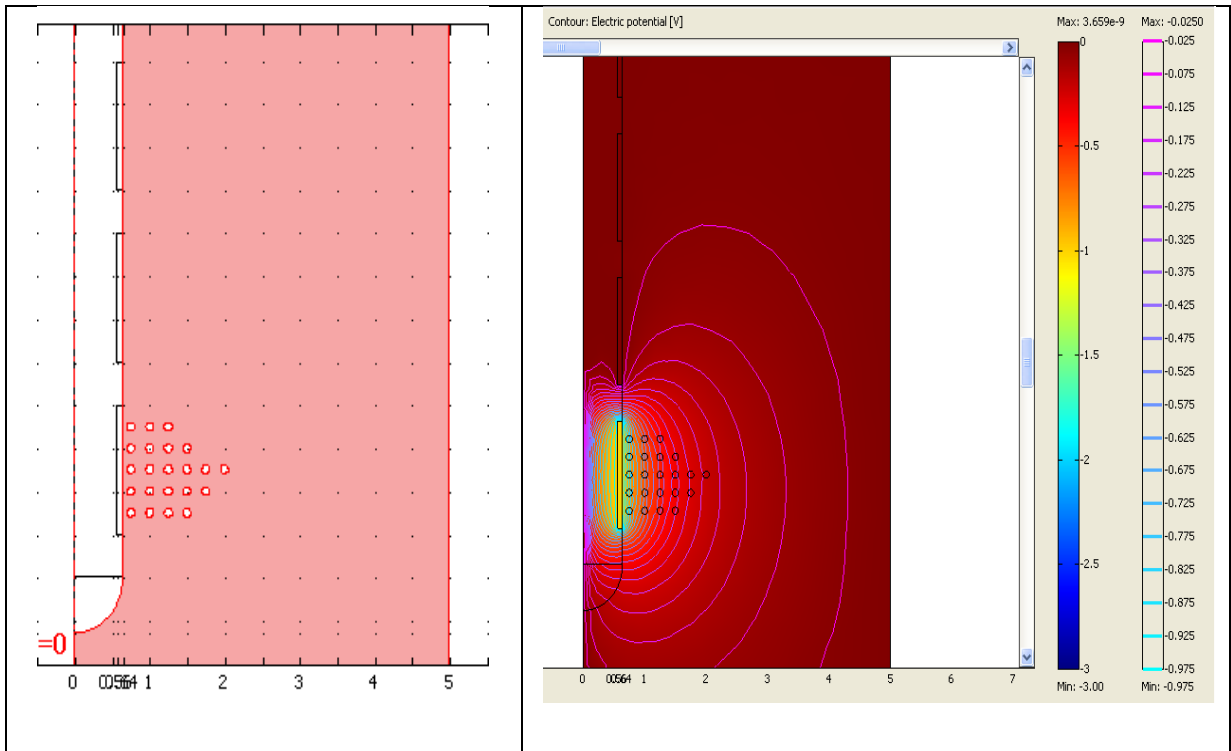


Figure 6-23 Prediction of neuron model activation for pulse amplitude $V = -1$ Volt

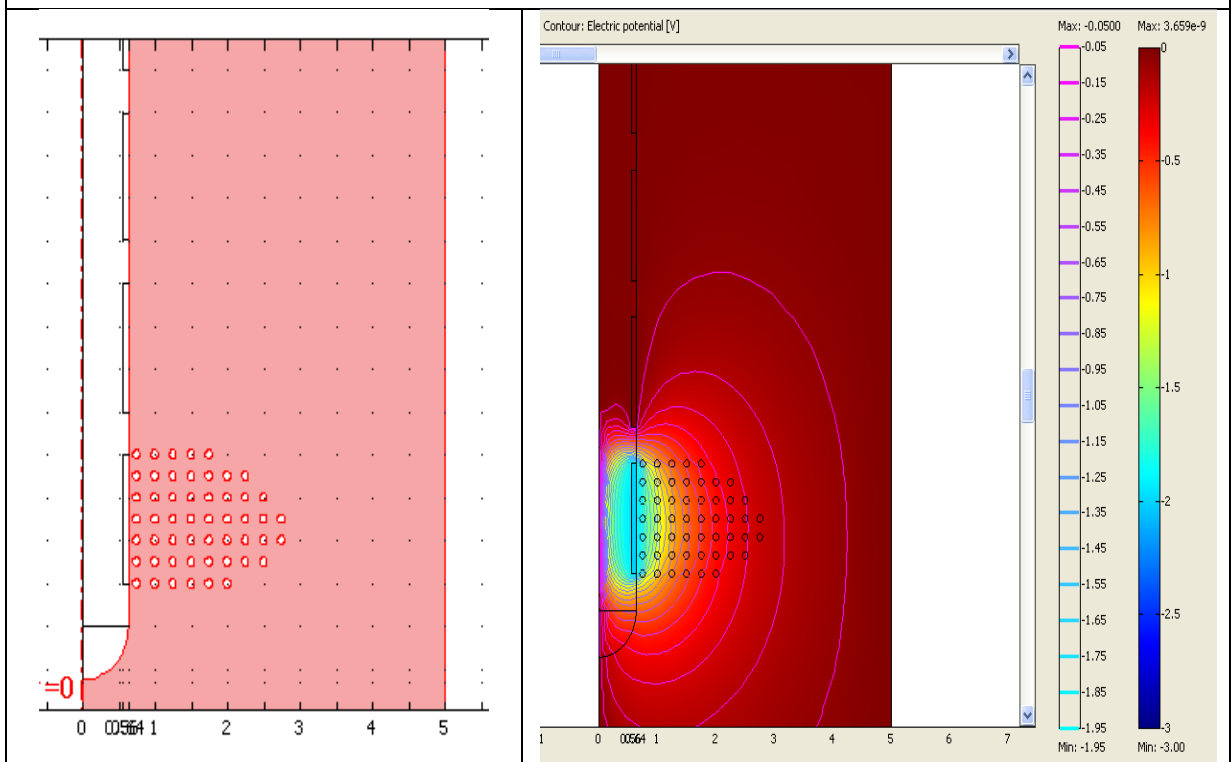


Figure 6-24 Prediction of neuron model activation for pulse amplitude $V = -2$ Volt

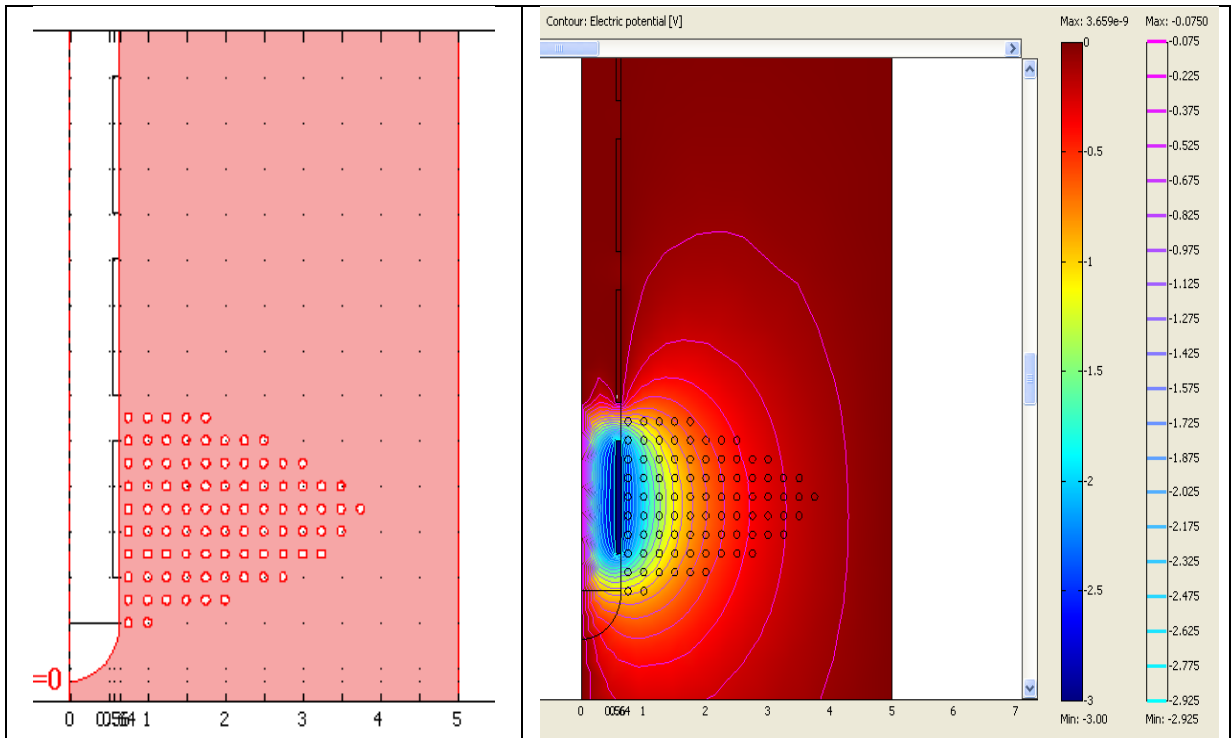


Figure 6-25 Prediction of neuron model activation for pulse amplitude $V = -3$ Volt

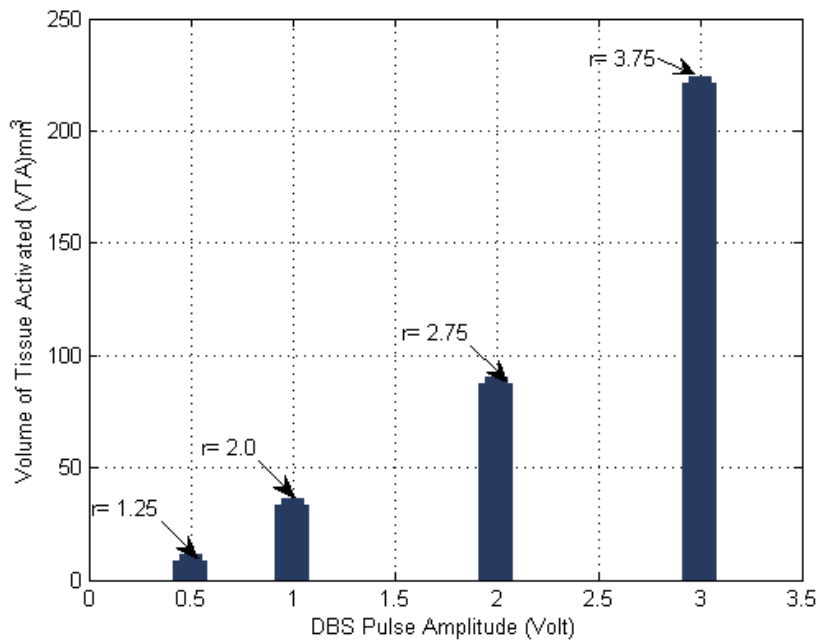


Figure 6-26 Effect of DBS pulse amplitude on VTA for different four voltage values (-0.5 V, -1.0 V, -2.0 V, and -3.0 V)

Table 6-1 Effect of DBS pulse amplitude on VTA and its equivalent radius

V(Pulse) volt	R _{max} (mm)	VTA _{max} [mm ³]
-0.5	1.25	8.18
-1.0	2.00	33.50
-2.0	2.75	87.11
-3.0	3.75	220.89

Once more, this is the first time, to the best of the author knowledge; we are able to determine the threshold for activation, and hence the volume of tissue activated for a given pulse amplitude which is again a very crucial for the physician to determine the stimulation parameters of DBS electrode.

6.6 Stochastic STN Neuron Model

In this section, we will study the effect of the neuron gating variables (n, m and h) on the spiking activity inside the STN region and hence the tuning curves, we want to prove that the proposed DBS model is still capable in analyzing and decoding these changes in a rigid manner. Following the study of Hodgkin and Huxley, most of the neurons models have treated the generation and propagation of action potentials using deterministic differential equations since the gating variables n, m and h describes the mean ratios of the open gates of the working channels. Back to the Hodgkin-Huxley model, the dynamics of the membrane potential V, measured throughout this work in mV is given by:

$$C \frac{d}{dt} V + g_{Na} m^3 h (V - V_{NA}) + g_K n^4 (V - V_K) + g_L (V - V_L) = 0 \quad (6.2)$$

The combined action of m and h controls the Na⁺ channels. The K⁺ gates are controlled by n.

The mean values of these gating variables are determined according to the equations (2.9) to (2.11) which as shown before can be inserted in the form of:

$$\frac{dx}{dt} = -\frac{1}{\tau_x(V)} [x - x_0(V)] \quad (6.3)$$

where x stands for m , n , or h . For fixed voltage V , the variable x approaches the value $x_0(V)$ with a time constant $\tau_x(V)$. The asymptotic value $x_0(V)$ and the time constant $\tau_x(V)$ are plotted in Figure 2-18. We can see from Figure 2-18 that m and n increase with V whereas h decreases. Thus, if some external input causes the membrane voltage to rise, the conductance of sodium channels increases due to increasing m . As a result, positive sodium ions flow into the cell and the action potential can be changed; this is the same scenario with a time constant τ as it is changed too with the voltage and hence the values of m , n , or h will be changed hence the action potential can be changed.

In all our previous simulations we had fixed the time constant τ for a mean value of 5ms [23] and according to Figure 2-18, this value can change from 0 to 1 from its maximum value. The effect of randomized this time constant τ on the neuron firing activities has been studied so that our STN neuron model is no longer deterministic but will be a stochastic STN neuron model.

We started with one STN neuron model ($N=1$) that is positioned at 1mm apart from the electrode shaft and placed into the middle of the DBS electrode first active contact. A negative 0.35 pulse amplitude voltage has been applied and as before, the system was solved and the activating function was calculated and coupled to the STN cell model using NEURON program. The firing activity was recorded for three different time constant τ output (0, 5 and 10ms respectively). The effect of this changing on the spikes rates are shown in Figure 6-27, Figure 6-28 and Figure 6-29 and listed in Table 6-2.

Table 6-2 Neurons spiking rate for different time constant τ at DBS pulse amplitude = - 0.35 V

Time constant τ (ms)	Spikes/Sec.
0	24
5	20
10	17

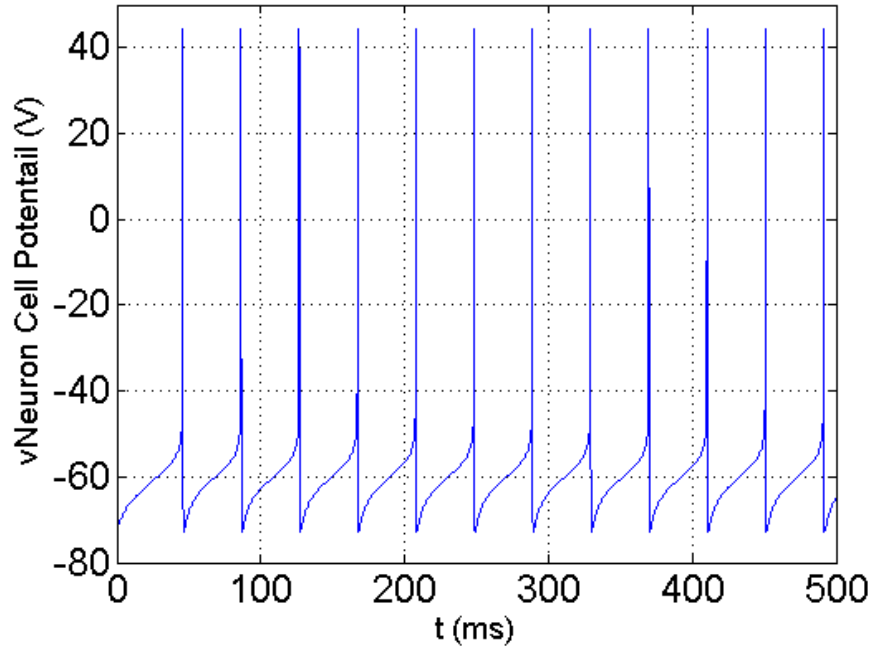


Figure 6-27 Firing activity rate (spikes/second) for DBS amplitude voltage of $v = -0.35$ volt with $\tau = 0$ ms

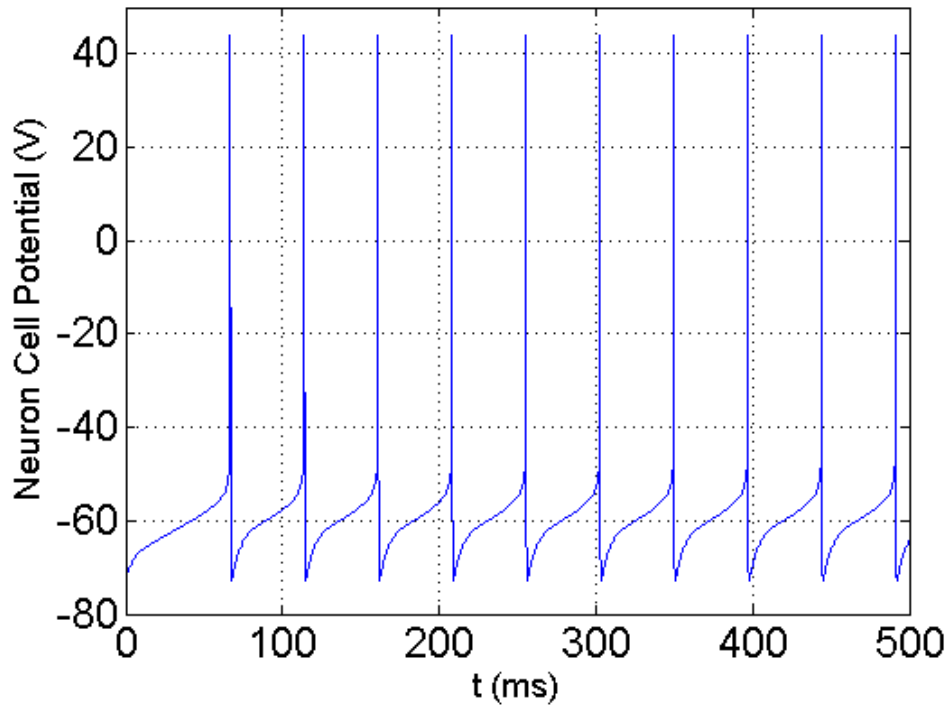


Figure 6-28 Firing activity rate (spikes/second) for DBS amplitude voltage of $v = -0.35$ volt with $\tau = 5$ ms

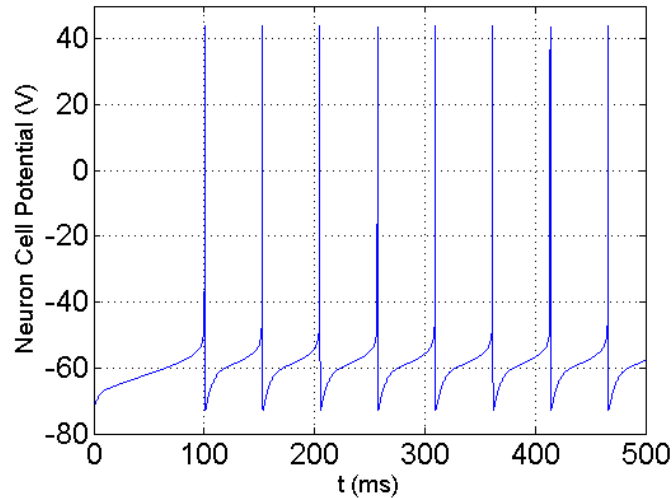


Figure 6-29 Firing activity rate (spikes/s) for DBS amplitude voltage of $v = -0.35$ volt with $\tau = 10$ ms

In order to study the effect of changing the time constant τ on our DBS model, we need to rebuild the tuning curves as was done before. We started with one STN neuron located at 1.5 mm from the DBS electrode shaft and centered at the middle of the first active contact, 10 different voltages were applied and for each voltage the time constant τ was randomly changed between 0 and 10ms in order to find properties of this stochastic process. The system was solved and the activating function was calculated and coupled to the STN cell model using NEURON program and the firing activity was recorded. The variations of this spikes/second around its mean values (time constant = 5ms) were plotted in Figure 6-30.

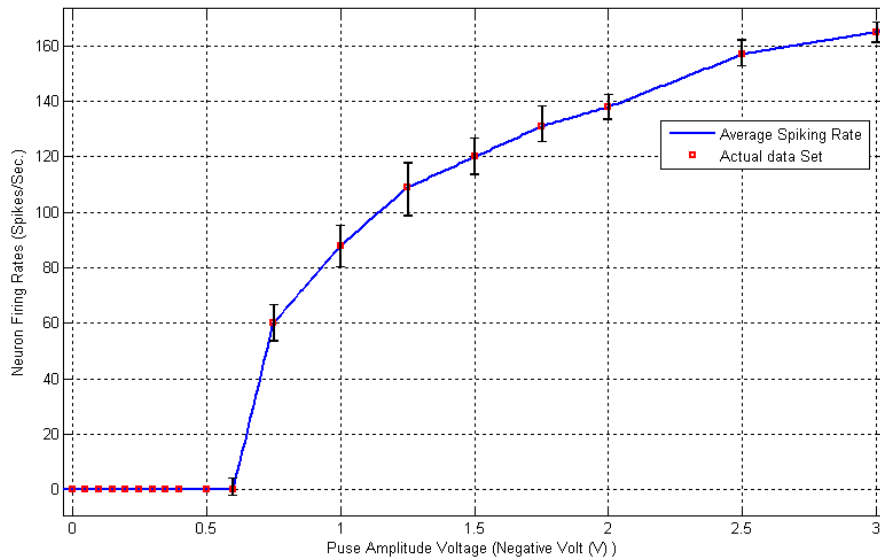


Figure 6-30 Neuron firing rates variation on a tuning curve for a neuron located at 1.5 mm from electrode shaft at the center of the first DBS electrode contact

The effect of spikes variation on our optimal linear decoder filter implementation to find the accurate decoding of neural firing activity representing the input DBS parameters has been studied. From these spike variations, the standard deviation σ was calculated at each DBS pulse amplitude voltage and was set to its maximum value where it is found to be $\sigma \cong 0.1$. This standard deviation σ has added to the tuning curve matrix A and the linear filter coefficients (φ) were again recalculated according to equation (3.11) in such a way to minimize the error between the applied DBS pulse amplitude and the reconstructed pulse amplitude. The optimal linear decoder's minimum errors versus neurons population are calculated in Figure 6-31. It was found that this error is proportional to the extracted equation:

$$\text{Mean Square Error} \cong 1/N \quad (6.4)$$

This stochastic STN model variation has increased the error of the optimal linear filter decoder used with compared to the deterministic STN neuron model as shown in Figure 6-32.

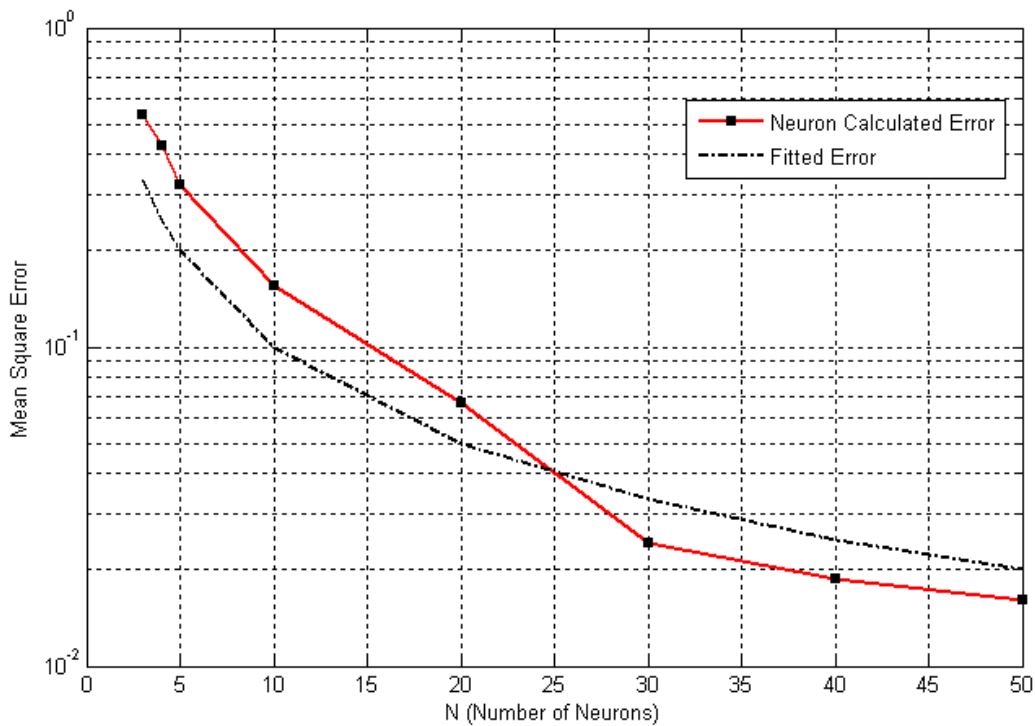


Figure 6-31 Mean square error versus neuron populations N for $\sigma \cong 0.1$

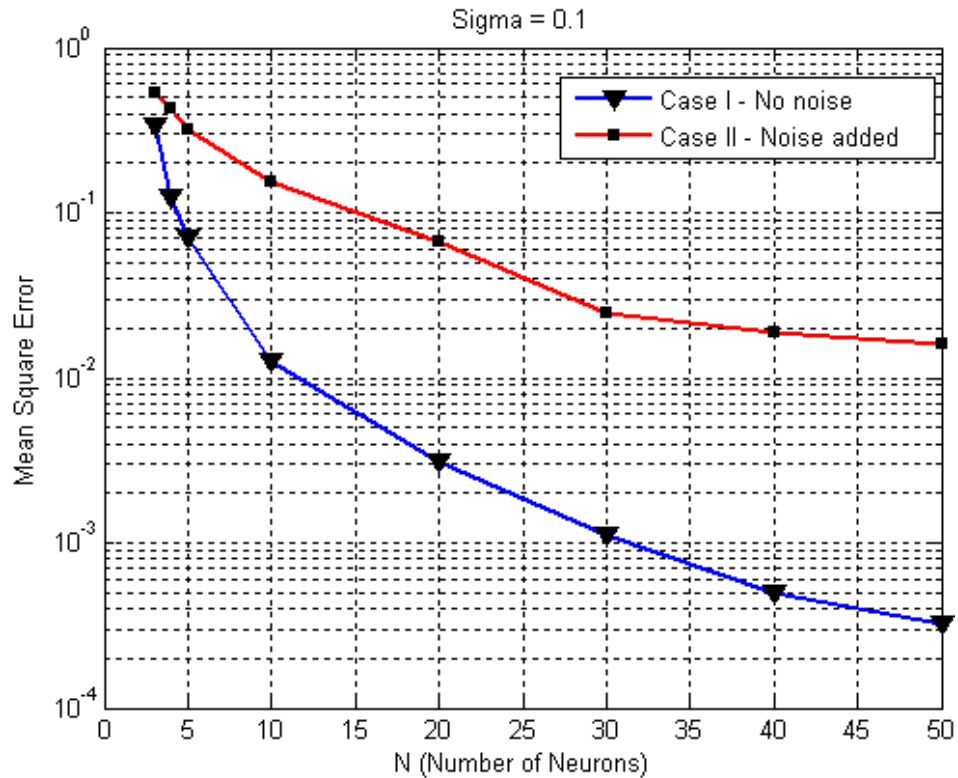


Figure 6-32 Comparison of Mean square error versus neuron populations N for deterministic STN model and stochastic STN model of $\sigma \cong 0.1$

6.7 Conclusion

The objective of this chapter was to introduce the interaction between the calculated activating function in the previous chapter and the STN neurons model inside the brain medium. The results of DBS STN neuron stimulation were used in many scenarios to show the effect of the activating function on the firing activity of the neurons.

Neurons which placed in the regions of depolarization and hyperpolarization have been introduced and the results confirmed the action potential concept. Also the rates at which the neurons are fired have been studied for different stimulation DBS electrode amplitude voltages indicating high rates of activity with the increasing of the stimulation amplitude.

A quantitative evaluation of the volume of tissue activated (VTA) has been performed for a range of different DBS pulse amplitude variations and it was in order of mm^3 which matched

with many clinical studies. Our intentions were to define specific characteristics of the VTA that corresponds to certain DBS stimulating voltage.

STN tuning curves were built for different number of neurons population N . The firing rates from these curves were the key to design our optimal linear decoding filter that can reconstruct the DBS input parameters from these neurons spiking activity. Also, these firing rates values played an important role in explaining the DBS mechanism as discussed in our DBS proposal model. These firing rates have successfully give us the role of the neurons charge distribution and how their electric field is interacted with the external electric field that is produced from the stimulation pulses applied on the DBS electrode.

Finally, a stochastic STN neuron model was introduced to study its effect on the neuron firing rates and hence on the tuning curves. Our proposed DBS model was a rigid system that its optimal linear filter was still capable of minimizing the error between the applied stimulation pulses and the reconstructed ones. Showing how the error is increased with respect to the case of deterministic STN neuron model.

Chapter 7

Conclusions and Future Work

In this Chapter, we present our conclusions and outline our future research directions.

7.1 Conclusions

Deep brain stimulation techniques are spreading to new ailments such as depression, and obsessive compulsive disorder as the numbers of patients who benefit from this surgical intervention are increasing. The ultimate challenge is to develop a computational model for the electrode–brain interaction that can to predict the best stimulation parameters for each individual patient.

In this thesis, we have proposed a comprehensive model that will help to understand the mechanism of deep brain stimulation (DBS) for a commercially approved electrode (Medtronic) that is implanted inside the STN brain region. Our results have shown that the proposed DBS model can achieve the targeted neurons' electric field distribution and hence the required electric input parameters for the DBS electrode. In addition, detailed analysis of the problem has indicated that the proposed DBS model can work for either a deterministic STN neurons model or stochastic ones. The achievements accomplished in this thesis can be summarized as follows.

In Chapter 2, we surveyed the state of the art in deep brain stimulation mechanisms and the various biological neuron models that represent an action potential. We have identified the challenges for better understanding of the DBS mechanism by compartment details for the STN regions for which the DBS electrode is implanted.

In Chapter 3, we have proposed a novel DBS model for implanted electrodes surrounded by different neurons populations, which offers a new approach to study the interaction between the DBS electrodes and the neuron world. In addition, our DBS model is capable of quantify neurons' firing activity and hence their volume of tissue activated assigned.

In Chapter 4, Finite Difference Time Domain (FDTD) has been proposed for modeling and simulating the DBS electrode and brain tissue medium. The effect of many DBS electrode

parameters and brain tissue in controlling the electric field distribution have been analyzed and quantitatively evaluated. FDTD had the advantage compared to FEM in this computational study since it can analyze the importance of the DBS parameters in one simulation execution.

Three models (Model-I to Model-III) were developed representing DBS electrode inside brain tissue and their effect on the electric field distribution around the DBS electrode have been studied and quantified.

In Chapter 5, the integration of the electric field and the second order spatial voltage distribution (Activating Function) were successfully calculated using Finite Element Method (FEM) which was used in modeling and simulating the DBS electrode and brain tissue medium. All the parameters of brain conductivity and permittivity were chosen according to the results of chapter 4.

The FEM results confirm the results we have obtained in Chapter 3 where the DBS pulse amplitude has no effect on the electric field penetration inside the brain tissue but only changes its strength. The maximum value of the activating function was studied for different parallel and tilting positions from the DBS electrode shaft, also, different brain mediums (isotropic or anisotropic) and even the DBS electrode encapsulation thickness were implemented and analyzed their effect on the activating function.

In Chapter 6, we represented the significance of the proposed DBS model for implanted DBS electrode inside STN brain region as we were successfully capable of finding the interaction between the electric field produced from DBS electrode (source) and the internal electric field generated from the STN neurons charge.

It is the first time, to the best of the author knowledge; we built STN tuning curves and we determined the threshold for activation ($\sim 200.0 \text{ V/m}^2$ inside the brain tissue). Also, the volume of tissue activated were calculated for a given pulse amplitude. All of this information is very vital for the DBS physicians.

Neurons depolarization and hyperpolarization regions have been confirmed in this study through the generation or non-generation of the neuron membrane potential (action potential).

Also, neurons spiking activity have been studied under altering the DBS electrode pulse amplitude voltages demonstrating high activity (spikes/second) with the increasing of the stimulation amplitude.

We have proposed an optimal linear decoder that was successfully used with the neurons tuning curves to quantify the interaction between neurons' electric field and DBS input parameters which was our finest goal in the design of our proposed DBS model. In addition we proved that as the numbers of neurons population (N) increased; the better is the system performance and hence a more realistic neurons' charge distribution is achieved.

The rigidity of our proposed DBS model appears in providing the VTA and the neurons spiking activity at different applied DBS pulse amplitude to the physician without letting him goes through an iteration loops of trial and error. These kinds of iterations inside the operation room is very time consuming for either the patience or the physician and it can last for many hours until the disease symptoms relieved or a certain motion occurred when the physician targeted the right position and the volume of the brain needed.

7.2 Future Work

The research done in the thesis provides the basics steps for understanding the DBS mechanism and there are still many open research areas that should be tackled to completely understand the DBS mechanism. In the following paragraph, we outline future work.

Establishing DBS models that are assigned to a specific patient history which is an emerging technology named as patient-specific modeling (PSM).

Taking into account the changes occurred at the interface between the brain and the electrode on both short and long timescales on the DBS model.

Furthermore, the current study did not focus on the stimulation efficiency of electrode geometry, electrode dimensions, pad size and layout. To go further, the DBS model should also foresee the influence of different electrodes dimensions in the brain.

References

- [1] W. T. Liberson, H. J. Holmquest, D. Scot, M. Dow, “Functional electrotherapy: stimulation of the peroneal nerve synchronized with the swing phase of the gait of hemiplegic patients”, *Archives of Physical Medicine and Rehabilitation*, vol. 42, pp: 101–105, 1961.
- [2] A.M. Lozano, N. Mahant, “Deep brain stimulation surgery for Parkinson’s disease: mechanisms and consequences”, *Parkinsonism and Related Disorders*”, vol. 10, pp. S49-S57, 2004.
- [3] D. J. DiLorenzo and J. D. Bronzino, “Neuroengineering”, CRC Press, 2007.
- [4] “The history of DBS”, <http://www.parkinsonsappeal.com>
- [5] Michael S Okun et al. “Avoiding deep brain stimulation failures in Tourette syndrome” *Journal of Neurol Neurosurg Psychiatry*, Vol. 79 pp. 111-112, 2008.
- [6] Krack P, et al. “Five-year follow-up of bilateral stimulation of the subthalamic nucleus in advanced Parkinson's disease. *N Engl J Med*; Vol. 349; pp. 1925-34, 2003.
- [7] C. C. McIntyre and W. M. Grill, “Extracellular stimulation of central neurons: influence of stimulus waveform and frequency on neuronal output”, the *Journal of Neurophysiology*, vol. 88, no. 4, pp: 1592 – 1604, 2002.
- [8] McIntyre C C, Savasta M, Goff L K and Vitek J L “Uncovering the mechanisms of action of deep brain stimulation: activation, inhibition or both” *Clin. Neurophysiol*, Vol. 115, pp. 1239–1248, 2004.
- [9] P. Limousin, P. Krack, P. Pollak, A. Benazzouz, C. Ardouin, D. Hoffmann, A. Benabid, “Electrical stimulation of the subthalamic nucleus in advanced Parkinson's disease”, *The New England Journal of Medicine*, vol. 339, pp: 1105 – 1111, 1998.
- [10] E. Moro, R. J. A. Esselink, J. Xie, M. Hommel, A. L. Benabid, P. Pollak, “The impact on Parkinson’s disease of electrical parameter settings in STN stimulation”, *Neurology*, vol. 59, pp: 706 – 13, 2002.
- [11] F. S. Barnes and B. Greenbaum, “Bioengineering and biophysical aspect of electromagnetic fields”, CRC Press Taylor and Francis Group, 2007.
- [12] F. L. H. Gielen, “Deep brain stimulation - current practice and challenges for the future”, *First International IEEE EMBS Conference on Neural Engineering*, pp: 489 – 491, 2003.
- [13] “Neurological disorders: public health challenges” By World Health Organization, 2006.
- [14] “Medtronic electrode”, wwwp.medtronic.com
- [15] Joel S. Perlmutte and Jonathan W. Mink “Deep brain stimulation” *Annual Review Neurosci.* Vol. 29, pp. 229–57, 2006.
- [16] Duvoisin R & Sage J “Parkinson’s disease: a guide for patient and family, 5th edition”, 2001.

- [17] Roy A. E. Bakay, “Movement disorder surgery: the essentials”, 2008.
- [18] Christopher R. Butson and Cameron C. McIntyre “Deep brain stimulation of the STN” Proceedings of the 2 International IEEE EMBS Conference on Neural Engineering Arlington, Virginia · March 16 - 19, 2005.
- [19] Stephen K. Fisher and Bernard W. Agranoff “Receptor activation and inositol lipid hydrolysis in neural tissues”, *J. Neurochem.*, Vol. 48, No. 4, pp. 999-1017, 1987.
- [20] Pedro J. Andres-Barquin “Ramón y Cajal: a century after the publication of his masterpiece” *Endeavour* Vol. 25(1), pp. 13-16, 2001.
- [21] G. Paxinos and J. K. Mai, “The human nervous system”, Elsevier Academic Press, 2004.
- [22] J. J. Warner, “Atlas of neuroanatomy”, Butterworth Heinemann, 2001.
- [23] Wulfram Gerstner and Werner M. Kistler “Spiking neuron models single neurons, populations, plasticity” Cambridge University Press, 2002.
- [24] Chris Elia Smith, “Lecture notes SYDE 750”, 2010.
- [25] Hille, B. “Ionic channels of excitable membranes”, Sinauer Associates, Sunderland, Mass., 2nd edition, 1992.
- [26] Eugene M. Izhikevich, “Which model to use for cortical spiking neurons” *IEEE Transactions on Neural Networks*, Vol. 15, No. 5, pp. 1063-1070, 2004.
- [27] Stein, R. B. “Some models of neuronal variability” *Biophys. J.*, 7:37-68. 1967.
- [28] A. L. Hodgkin and A. F. Huxley, “A quantitative description of membrane current and its application to conduction and excitation in nerve” *J Physiol*, Vol. 117(4), pp. 500–544, 1952.
- [29] Llinás, R. “The intrinsic electrophysiological properties of mammalian neurons: Insights into central nervous system function”. *Science*, Vol. 242, No. 4886, pp. 1654-1664, 1988.
- [30] Koch, C. “Biophysics of computation” Oxford University Press, New York. 1999.
- [31] Huguenard, J. R. and McCormick, D. A. “Simulation of the currents involved in rhythmic oscillations in thalamic relay neurons” *J. Neurophysiol.*, Vol. 68, pp. 1373-1383, 1992.
- [32] Jahnsen, H. “Electrophysiological characteristics of neurons in the guinea-pig deep cerebella nuclei in vitro. *J. Physiol.*, Vol. 372, pp. 129-147, 1986.
- [33] Abbott, L. F., Fahri, E., and Gutmann, S. “The path integral for dendritic trees” *Biol. Cybern.*, Vol. 66, pp. 49-60, 1991.
- [34] Bower, J. M. and Beeman, D. “The book of GENESIS: exploring realistic neural models with the general neural simulation system” Springer, New York. 1995.
- [35] Gabbiani, F., Midtgaard, J., and Knoepfl, T. “Synaptic integration in a model of cerebellar granule cells” *J. Neurophysiol.*, Vol. 72, pp. 999-1009, 1994.

- [36] McIntyre C. C., Richardson A. G. and Grill W. M. “Modeling the excitability of mammalian nerve fibers: influence of after potentials on the recovery cycle” *J. Neurophysiol.* Vol. 87, pp. 995–1006, 2002.
- [37] S. N. Sotiropoulos and P. N. Steinmetz, “Assessing the direct effects of deep brain stimulation using embedded axon models”, *Journal of Neural Engineering*, pp: 107–119, 2007.
- [38] C.C. McIntyre, W.M. Grill, D.L. Sherman, N.V. Thakor, “Cellular effects of deep brain stimulation: model-based analysis of activation and inhibition”, *J. Neurophysiol.*, vol. 91, no. 4, pp. 1457-1469, 2004.
- [39] Destexhe A, Neubig M, Ulrich D, and Huguenard J. “Dendritic low-threshold calcium currents in thalamic relay cells” *J. Neurosci.* Vol. 18, pp. 3574–3588, 1998.
- [40] Hubel, D. H. and Wiesel, T. N. “Receptive fields of single neurons in the cat's striate cortex” *J. Physiol.*, Vol. 148, pp. 574-591, 1959.
- [41] Frank Rattay “Analysis of models for external stimulation of axons” *IEEE Transactions on Biomedical Engineering*, Vol. BME-33, No. 10, pp. 974-977, 1986.
- [42] C. Gabriel, S. Gabriel, E. Corthout, “The dielectric properties of biological tissues: I. Literature survey”, *Physics in medicine and biology*, vol. 41, pp: 2231 – 2249, November 1996.
- [43] S. Gabriel, R. W. Lau, C. Gabriel, “The dielectric properties of biological tissues: II. Measurements in the frequency range 10 Hz to 20 GHz”, *Physics in Medicine and Biology*, vol. 41, No. 11, pp: 2251 – 2269, 1996.
- [44] S. Gabriel, R. W. Lau, C. Gabriel, “The dielectric properties of biological tissues: III. Parametric models for the dielectric spectrum of tissues”, vol. 41, No. 11, pp: 2271 – d2293, November 1996.
- [45] A. M. Kuncel and W. M. Grill, “Selection of stimulus parameters for deep brain stimulation”, *Clinical Neurophysiology*, vol. 115, pp: 2431 – 2441, 2004.
- [46] NEURON program “<http://www.neuron.yale.edu/neuron/>”
- [47] Monson H. Hayes “Statistical digital signal processing and modeling” JOHN WILEY INC., 1996.
- [48] COMSOL Multiphysics Tool “www.comsol.com”.
- [49] H. P. Schwan, "Dielectric properties of biological tissue and physical mechanisms of electromagnetic field interaction", *Biological Effects of Nonionizing Radiation*, ACS Symposium Series 157, Karl H. Illinger, the American Chemical Society, 1981.

- [50] L. A. Geddes and L. E. Baker, “The specific resistance of biological material - A compendium of data for the biomedical engineer and physiologist”, *Journal of Medical and Biological Engineering and Computing*, vol. 5, No. 3, pp: 271–293, May 1967.
- [51] Christopher R. Butson, Cameron C. McIntyre, “Current steering to control the volume of tissue activated during deep brain stimulation”, *Journal of Brain Stimulation* vol. 1, Issue 1, pp: 7 – 15, January 2008.
- [52] Christopher R. Butson, Christopher B. Maks, Cameron C. McIntyre, “Sources and effects of electrode impedance during deep brain stimulation”, *Journal of Clinical Neurophysiology*, vol. 117, Issue 2, pp: 447 – 454, February 2006.
- [53] R. Salvador, P. C. Miranda, Y. Roth, A. Zangen, “High-permeability core coils for transcranial magnetic stimulation of deep brain regions”, *IEEE EMBS 2007 Conference Proceedings*, pp: 6653 – 6656, 2007.
- [54] Heethaar, F. H. Lopes da Silva, “In vivo measurement of the brain and skull resistivities using an EIT-based method and realistic models for the head,” *IEEE Transactions in Biomedical Engineering*, vol. 50, pp: 754 – 767, June 2003.
- [55] P. W. Nicholson, “Specific impedance of cerebral white matter”, *Experimental Neurology*, vol. 13, pp: 386 – 401, 1965.
- [56] F. Apollonio, A. Paffi, M. Parazzini, F. Maggio, T., Novellino, P. Ravazzani, G. D’Inzeo, “Fundamental electrical quantities in deep brain stimulation: influence of domain dimensions and boundary conditions”, *IEEE EMBS 2007 Conference Proceedings*, pp: 6669 – 72, 2007
- [57] Frank S. Barnes and Ben Greenbaum, “Bioengineering and biophysical aspects of electromagnetic fields”, CRC Press, 2007.
- [58] Italian national research council, Institute for Applied Physics: <http://niremf.ifac.cnr.it/tissprop>
- [59] “EMPIRE XCcel manual”, IMST GmbH, Germany, November 12, 2008: <http://www.empire.de/>
- [60] A. Bondeson, T. Rylander, P. Ingelström, “Computational electromagnetics”, Springer, New York, 2005, ch. 5, pp: 57 – 81.
- [61] S. Miocinovic, S. F. Lempka, G. S. Russo, C. B. Maks, C. R. Butson, K. E. Sakaie, J. L. Vitek, C. C. McIntyre, “Experimental and theoretical characterization of the voltage distribution generated by deep brain stimulation”, *Journal of Experimental Neurology*, vol. 216, pp: 166–176, 2009.

- [62] C. C. McIntyre and W. M. Grill, “Extracellular stimulation of central neurons: influence of stimulus waveform and frequency on neuronal output”, *The Journal of Neurophysiology*, vol. 88, no. 4, pp: 1592 – 1604, 2002.
- [63] Vadim S. Polikov, Patrick A. Tresco, William M. Reichert, “Response of brain tissue to chronically implanted neural electrodes”, *Journal of Neuroscience Methods*, vol. 148, Issue 1, pp: 1 – 18, 2005.
- [64] K. Kagoo, “Microelectrode arrays for neural recording”, School of Engineering, UCSC, January 2005.
- [65] L. A. Geddes, R. Roeder, “Criteria for the selection of materials for implanted electrodes”, *Annals of Biomedical Engineering*, pp: 879 – 890, 2003.
- [66] E. Fournier, C. Passirani, C. N. Montero-Menei, J. P. Benoit, “Biocompatibility of implantable synthetic polymeric drug carriers: focus on brain compatibility”, *Biomaterials*, vol. 24, pp: 3311 – 3331, 2004.
- [67] . C. Collias and E. E. Manuelidis, “Histopathological changes produced by implanted electrodes in cat brains”. *Journal of Neurosurgery*, vol. 14, pp: 302 – 328, 1957.
- [68] F. R. Robinson and M. T. Johnson, “Histopathological studies of tissue reactions to various metals implanted in cat brains”, ASD Technical Report, Aeronautical Systems Div Wright-Patterson Afb Ohio Aerospace Medical Div, October 1961.
- [69] P. K. Campbell, K. F. Jones, R. J. Huber, K. W. Horch, R. A. Normann, “A silicon-based, three-dimensional neural interface”, *IEEE Transactions on Biomedical Engineering*, vol. 38, pp: 758 – 768, 1991.
- [70] J. N. Turner, W. Shain, D. H. Szarowski, M. Anderson, S. Martins, M. Isaacson, H. Craighead, “Cerebral astrocyte response to micro machined silicone implants”, *Experimental Neurology*, pp: 33 – 49, 1999.
- [71] E. Moro, R. J. A. Esselink, J. Xie, M. Hommel, A. L. Benabid, P. Pollak, “The impact on Parkinson’s disease of electrical parameter settings in STN stimulation”, *Neurology*, vol. 59, pp: 706 – 13, 2002.
- [72] C. R. Butson and C. C. McIntyre, “Role of electrode design on the volume of tissue activated during deep brain stimulation”, *Journal of Neural Engineering*, vol. 3, pp: 1–8, 2006.
- [73] J P B’erenger. “A perfectly matched layer for the absorption of electromagnetic waves”, *J. Comput. Phys.*, 114(2):185–200, October 1994.

- [74] S. R. I. Gabran, J. H. Saad, M. M. A. Salama, R. R. Mansour, "Finite difference time domain (FDTD) modeling of implanted deep brain stimulation electrodes and brain tissue", 31st IEEE Engineering in Medicine and Biology Society, Minnesota, USA, pp: 6485 – 6488, September 2009.
- [75] J. Saad, S. Gabran, M. Salama, R. Mansour, "Quantitative modeling of electric field in deep brain stimulation: study of medium brain tissue and stimulation pulse parameters", 5th International IEEE EMBS Conference on Neural Engineering, Cancun, Mexico. April 27- May 1, 2011.
- [76] Xuefeng F. Wei and Warren M. Grill, "Impedance characteristics of deep brain stimulation electrodes in vitro and in vivo" Journal of Neural Engineering, 6 (2009), pp: 1641-1649.
- [77] S. N. Sotiropoulos, B. Mueller, K. O. Lim and P. N. Steinmetz, "Calculation of stereotaxically registered brain conductivities and anisotropies using Diffusion Tensor MR Imaging" International Journal of Bioelectromagnetism, Vol. 7, No. 1, 2005, pp: 146-149.
- [78] Zhang TC, Grill WM, "Modeling deep brain stimulation: point source approximation versus realistic representation of the electrode", Journal of Neural Engineering, 7 (2010), p. 066009.